

NIST GCR 03-849

Application of CFD Modeling to Room Fire Growth on Walls

K.M. Liang, T. Ma, J.G. Quintiere
University of Maryland
College Park, MD 20742

and

D. Rouson
The City College of CUNY
New York, NY 10031

NIST

National Institute of Standards and Technology
Technology Administration, U.S. Department of Commerce

Report Documentation Page			Form Approved OMB No. 0704-0188		
Public reporting burden for the collection of information is estimated to average 1 hour per response, including the time for reviewing instructions, searching existing data sources, gathering and maintaining the data needed, and completing and reviewing the collection of information. Send comments regarding this burden estimate or any other aspect of this collection of information, including suggestions for reducing this burden, to Washington Headquarters Services, Directorate for Information Operations and Reports, 1215 Jefferson Davis Highway, Suite 1204, Arlington VA 22202-4302. Respondents should be aware that notwithstanding any other provision of law, no person shall be subject to a penalty for failing to comply with a collection of information if it does not display a currently valid OMB control number.					
1. REPORT DATE 01 JAN 2003		2. REPORT TYPE		3. DATES COVERED 00-00-2003 to 00-00-2003	
4. TITLE AND SUBTITLE Application of CFD Modeling to Room Fire Growth on Walls			5a. CONTRACT NUMBER		
			5b. GRANT NUMBER		
			5c. PROGRAM ELEMENT NUMBER		
6. AUTHOR(S)			5d. PROJECT NUMBER		
			5e. TASK NUMBER		
			5f. WORK UNIT NUMBER		
7. PERFORMING ORGANIZATION NAME(S) AND ADDRESS(ES) University of Maryland, College Park, MD, 20742			8. PERFORMING ORGANIZATION REPORT NUMBER		
9. SPONSORING/MONITORING AGENCY NAME(S) AND ADDRESS(ES)			10. SPONSOR/MONITOR'S ACRONYM(S)		
			11. SPONSOR/MONITOR'S REPORT NUMBER(S)		
12. DISTRIBUTION/AVAILABILITY STATEMENT Approved for public release; distribution unlimited					
13. SUPPLEMENTARY NOTES					
14. ABSTRACT					
15. SUBJECT TERMS					
16. SECURITY CLASSIFICATION OF:			17. LIMITATION OF ABSTRACT Same as Report (SAR)	18. NUMBER OF PAGES 136	19a. NAME OF RESPONSIBLE PERSON
a. REPORT unclassified	b. ABSTRACT unclassified	c. THIS PAGE unclassified			

NIST GCR 03-849

Application of CFD Modeling to Room Fire Growth on Walls

Prepared for
*U.S. Department of Commerce
Building and Fire Research Laboratory
National Institute of Standards and Technology
Gaithersburg, MD 20899*

By
K.M. Liang, T. Ma, J.G. Quintiere
University of Maryland
College Park, MD 20742

and

D. Rouson
The City College of CUNY
New York, NY 10031

April 2003



U.S. Department of Commerce
Donald L. Evans, Secretary

Technology Administration
Phillip J. Bond, Under Secretary for Technology

National Institute of Standards and Technology
Arden L. Bement, Jr., Director

Notice

This report was prepared for the Building and Fire Laboratory of the National Institute of Standards and Technology under grant number 60NANB9D0071. The statements and conclusions contained in this report are those of the authors and do not necessarily reflect the views of the National Institute of Standards and Technology or the Building and Fire Research Laboratory

Application of CFD Modeling to Room Fire Growth on Walls

K. M. Liang, T. Ma, J. G. Quintiere
Department of Fire Protection Engineering
University of Maryland
College Park, MD 20742

and

D. Rouson
Department of Mechanical Engineering
The City College of CUNY
New York, NY 10031

FINAL REPORT

January 2003

Prepared for:

U.S. Department of Commerce
National Institute of Standards and Technology
Laboratory of Building and Fire Research
Washington, D.C. 20234

ABSTRACT

An evaluation of the NIST FDS model was conducted with particular attention for its use in predicting flame spread on surfaces. Over the course of this investigation the computational model changed from combustion depicted by particles to a mixture fraction based combustion model. The study pertains to version 2.0 released on December 4, 2001.

Three aspects were considered in the study. First, we studied the evaluation of the code to predict a combusting plume. Second, the code was applied to a fire plume adjacent to a vertical wall, and then flame spread on the wall. Third, a complementary investigation of an improved algorithm for convective heat transfer at a surface was developed. The first two studies resulted in M.S. theses. Damian Rouson of CCNY performed the third study. The thesis by Ma on the axi-symmetric plume was previously transmitted and will not be included here. However, a recently accepted paper, based on the thesis with updated results is included.

The general conclusions are that the FDS code is very good for computing the fluid dynamics, entrainment and flame height. The temperature in the combustion region appears to be over-estimated at the base of the geometry considered, and any related heat flux is consequently over-predicted. The temperature results are grid dependent. A computation of flame spread on vertical PMMA gave mixed results.

The code was benchmarked against fire plume correlations after a review of the literature to obtain the most general results. Most of the experimental correlations have some deficiencies, and should be improved. Particular attention needs to be given to temperature measurements in the flame since these are generally under-estimated due to radiation error. The wall heat flux and flame spread comparisons were made against data we viewed as quality data.

The algorithm developed by Rouson is based on the theoretical formulation by Howard Baum, and has not been tested in the FDS code.

Acknowledgements

In addition to the funding of NIST/BFRL, the authors would like to acknowledge the support of Kevin McGrattan, who patiently responded to many questions on the workings of the **FDS** code; Howard Baum, for his exceptional formulation of the convective model; and to Thomas Ohlemiller, for his faithful monitoring of this grant. These efforts are greatly appreciated.

TABLE OF CONTENTS

EXECUTIVE SUMMARY	1
NUMERICAL SIMULATION OF AXI-SYMMETRIC FIRE PLUMES: ACCURACY AND LIMITATIONS, T. G. Ma and J. G. Quintiere..	I
EVALUATION STUDIES OF THE FLAME SPREAD AND BURNING RATE PREDICTIONS BY THE FIRE DYNAMICS SIMULATOR, M. Liang	II
SOFTWARE DEVELOPMENT FOR MODELING SCALAR TRANSPORT NEAR SURFACES IN COMPARTMENT FIRES, D. W. I Rouson	III

Executive Summary

The objective of this study was to investigate the ability to compute flame spread on walls using a field model. The model selected was the Large Eddy Simulation (LES) developed by NIST/BFRL that is entitled the Fire Dynamics simulator (FDS). Version 2.0 was used in the final analysis presented in this report; however, this work was originally begun with version 1.0. In version 2.0, the combustion is computed using a mixture fraction formulation, while in version 1.0 the combustion was specified by particles that released energy until their burnout. The time release depended on the nature of the fire being simulated. Thus, version 1.0 was not suited for predicting fires of an arbitrary nature as those resulting from a particular geometry or spread.

Particle Energy Release Rate. Version 1.0, with the prescribed particle energy release, is still a useful approach when information about the fire is available. The algorithm for describing the time-release of the particle energy is based on the McCaffrey fire plume correlation for axi-symmetric fires, and a constant energy release rate applied to each particle. For fires of other geometries, expressions must be available for representing the characteristic velocity and flame length, in the least. In a combustion system, the energy release rate is not uniform, but controlled by the rate of oxygen entrainment. A more general approach to selecting the energy release rate of the particles, and to illustrate its dependence on the fire geometry is presented below since it was not included in past progress reports.

Represent the energy release rate of the fire in terms of the selected particle release rate and its distributed energy release rate over the time for combustion.

$$\dot{Q} = \dot{n}_p \int_0^{t_b} \dot{q}_p(\tau) d\tau = \dot{n}_p \int_0^{z_f} \dot{q}_p(\eta) d\eta$$

where \dot{q}_p is the particle energy release rate,

t_b is the burning time,

z_f is the flame length,

\dot{n}_p is the selected particle rate.

The velocity of the particles generally depends on their launch site. But if they are based on a characteristic plume velocity, usually taken as the centerline velocity, then the trajectory can be based on

$$w = \frac{dz}{dt} \text{ or } t = \int_0^z \frac{dz}{w} \text{ where } w \text{ would be known as a function of } z.$$

The rate of entrainment into a fire plume can be approximately represented in terms of an entrainment velocity proportional by a constant (a) to the characteristic velocity

and the perimeter of the fire plume, $P(z)$. It follows that the rate of mass entrainment is

$$\dot{m}_e = \int_0^z \alpha \rho_\infty w P dz.$$

The rate of combustion energy in the plume depends on the oxygen that burns, and this has been empirically found to require n times the needed stoichiometric requirement with n generally found as about 10. The combustion rate is related to the entrainment as

$$Q = Y_{ox,\infty} \dot{m}_e \Delta h_c / n.$$

The particle energy release rate must follow accordingly as

$$q_p = \frac{dQ_p}{dz} = \alpha \rho_\infty Y_{ox,\infty} \Delta h_c w^2 P / (n \dot{m}_p).$$

The velocity in the combustion region of a fire plume is found to be proportional to $z^{1/2}$. The distribution of P with z depends on the dimension of the firebase relative to the flame height. For short flames, P is nearly constant and related to the base dimension; and for tall flames, P is proportional to z . Therefore, the particle energy release rate should vary as z or z^2 . For flames that have the flow constrained, as for example corner fires, P would decrease accordingly.

While this result for the particle energy rate is more complex than in version 1.0 of the **FDS**, it is more general and may find utility; or in the least, shows the dependence of the particle energy rate on the plume geometry.

Fire plume modeling. The objective of this study was to assess the application of a **CFD** model for the prediction of fire spread. The model selected for investigation was the NIST **FDS** code, and the objective became to establish its accuracy. Before the general problem of fire spread could be examined, it was felt that the accuracy of the **FDS** code should be assessed with simpler, but related problems. Since a fire plume is usually the ignition source and driving heat transfer for fire spread on adjacent objects, the fire plume became the first issue for examination. Moreover, much data exist for axi-symmetric fire plumes. These data became our focus in order to **assess** the **FDS** accuracy. Our approach was to examine the array of data and correlations for fire plumes and establish the “best” bases for comparison. “Best” was decided on the most comprehensive fit to data, and on the completeness of the correlation variables. Often both criteria could not be satisfied since most correlations do not include all of the relevant variables. The details are found in the Section 1.

For example, centerline plume temperature above the flame, in general, depends on

$$\frac{T - T_{\infty}}{T_{\infty}} = f(X_r, z/z^*, D/z^*)$$

where

$$z^* = \left(\frac{\dot{Q}}{\rho_{\infty} c_p T_{\infty} \sqrt{g}} \right)^{2/5} = (\dot{Q}_D^*)^{2/5} \cdot D$$

The best correlation above the flame was found based on the work of Heskestad:

$$\frac{T - T_{\infty}}{T_{\infty}} = C_T (1 - X_r)^{2/3} \left(\frac{z - z_0}{z^*} \right)^{-5/3}$$

where

$$\frac{z_0}{z^*} = -1.02 \frac{D}{z^*} + 1.37$$

gives the virtual origin, and Heskestad gives $C_T = 9.1$

In the flame region, the centerline temperature is approximately constant and depends on radiation fraction and somewhat on the fuel. It is shown that

$$\frac{T - T_{\infty}}{T_{\infty}} = 4.89(1 - X_r) \text{ or } T - T_{\infty} = 1455^{\circ}\text{C}(1 - X_r).$$

This suggests that the maximum temperature in turbulent flames with no radiation loss could be as much as 1500°C.

The experimental results for flame height are shown below for the common correlation of Heskestad, correlations from Zukoski over various Q^* values including values below 0.1, and that of Quintiere and Grove which included the effect of flame radiation fraction.

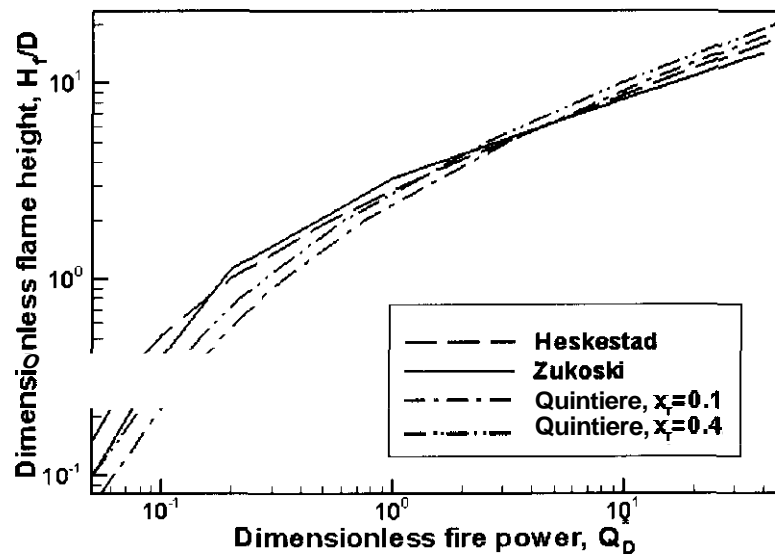


Figure 1. Flame height correlations

The FDS computations show good results for flame height as depicted below. The computed results use a criterion of the percent of combustion completeness to define the flame height in the computation. The computation results for low $Q^* < 0.5$ deviate markedly from the correlation. However, the data in this region are scant, and a more thorough experimental study is needed to properly examine the computations here

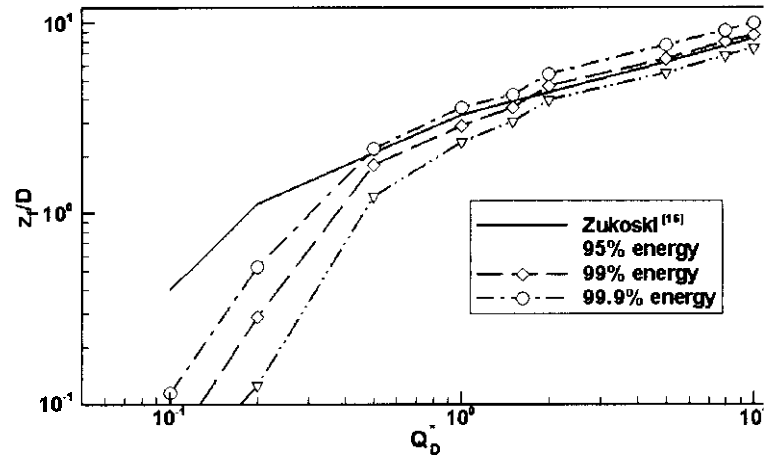


Figure 2. Computational results for flame height.

The computed results for the centerline Froude number, $Fr = w^2 \left(\frac{T - T_\infty}{T_\infty} \right) g z$, are shown in Figure 3. Inviscid theory gives a value of 2, and experimental values of about 1.3-1.9 are generally found in the literature. The FDS computation does a good job a reproducing these values and shows a distinct effect of Q^* that should be examined experimentally

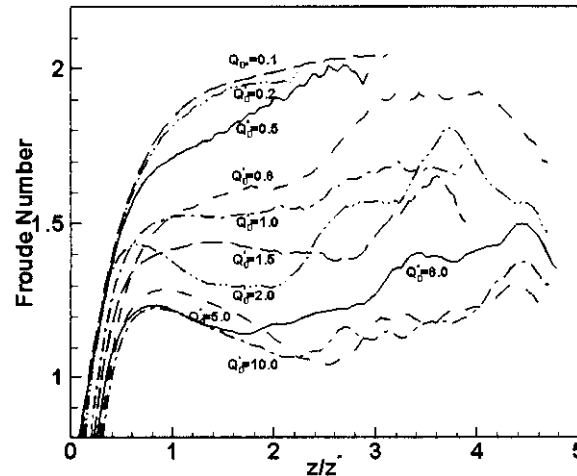


Figure 3. Fr computed on the centerline.

The rate of entrainment over the flame height was also computed, and the entrainment rate, normalized with the stoichiometric required airflow rate, was plotted against the normalized height. Figure 4 shows that for $Q^* > 0.5$, the amount of excess air entrained roughly 10 ± 2 as is generally found from experiments. This is a measure of the “unmixedness” of the fuel and the air in the fire plume. Lower values of Q^* exhibit much lower excess air ratios. Again, insufficient experimental data do not allow a definitive statement on the FDS accuracy in this Q^* range. However, FDS appears to do a good job at predicting the entrainment rates, suggesting that the **large** eddy structure captured in the model may be most significant for entrainment.

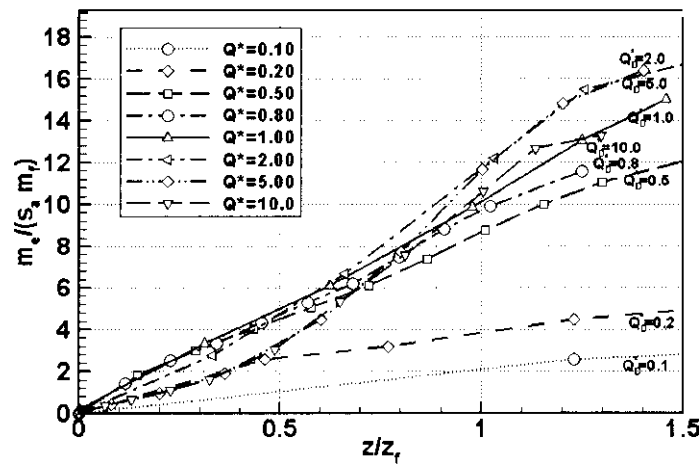
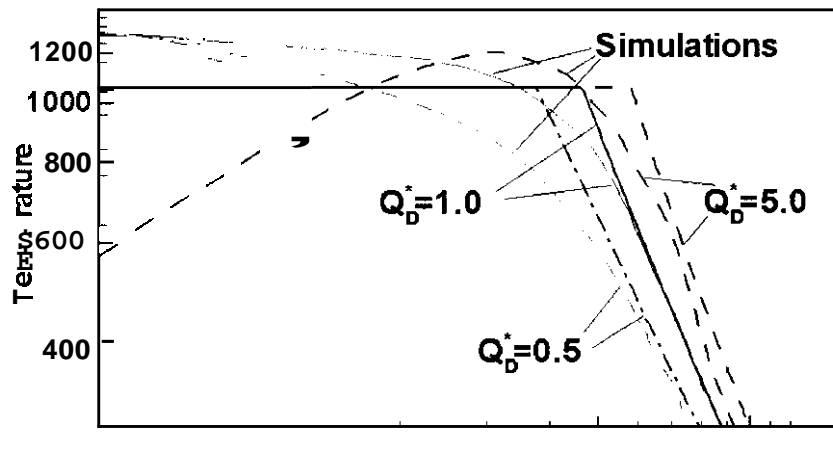


Figure 4. Normalized entrainment rate in the flame

Perhaps the weakest ability of the FDS code lies in the ability to predict the temperature in the flame region. This is likely due to the inability of the code to resolve the sub-grid combustion phenomena. The computed results compared to the



The computed temperatures tend to overestimate the correlation values in the flame zone for $Q^* < 1$, and show the effect of introducing “cool” fuel for large Q^* values. The comparison in the far field plume region is very good. The combustion temperatures can be overestimated by about 200 degrees. Again, good measurements in this region are lacking since radiation effects influence the measurement, and data are lacking for low Q^* fires in general.

In all of our computations, we used

$$R^* = \frac{\max(\delta x, \delta y, \delta z)}{z^*}$$

as a criterion for selecting the grid size to insure sufficient cells over the characteristic flame length,

$$z^* = (\dot{Q} / \rho_\infty c_p T_\infty \sqrt{g})^{2/5}.$$

We used $R^* = 0.05$ or 20 cells over the characteristic flame length. In FDS 2.0 the stoichiometric mixture fracture is adjusted to compensate for the code to resolve combustion is large grid cells. This adjustment is given as

$$\frac{Z_{f,eff}}{Z_f} = \min\left(1, C \cdot \frac{D^*}{\delta x}\right),$$

where C is an empirical constant to be used for all fire scenarios (here it is 0.025 in FDS2.0), δx is the grid size and D^* ($=z^*$ herein). Thus, for all $R^* > 0.025$ there is an adjustment; and our criterion just fell into this category. An experimental set of computations for a fire of 72.5 kW with varying grid cell selections was done to investigate the effect of grid on the flame temperature. These results are shown below. The temperature in the flame appears to increase, roughly, as the grid size is decreased. Except for the coarsest grid, the far field plume temperatures appear to be grid independent. The grid dependence is not understood, and suggests a weakness in the current combustion model.

Table 3. Simulation result of grid-dependent cases.

No.	Grid number	Domain size (m)	Grid size (cm)	Computed combustion rate (kW)	Total Radiative fraction	Maximum Temp.(°C)	Estimated $Z_{f,eff}/Z_f$
1	32x32x72	1.5x1.5x3.5	4.69	65.0	0.38	1205	0.18
2	48x48x96	1.5x1.5x3.5	3.13	64.5	0.40	1288	0.28
3	64x64x144	1.5x1.5x3.5	2.34	66.6	0.38	1000	0.37
4	32x32x72	1.5x1.5x3.5	Non-uniform	74.9	0.46	1374	0.37
5	32x32x80	.54x.54x1.35	1.69	72.8	0.41	1219	0.51
6	64x64x160	.54x.54x1.35	0.84	86.4	0.43	1347	1.00

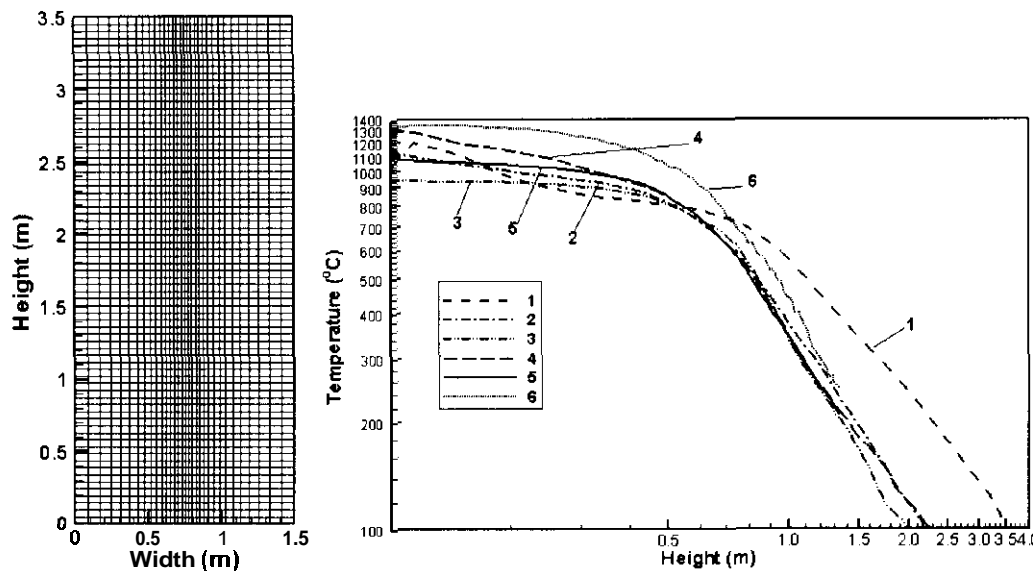
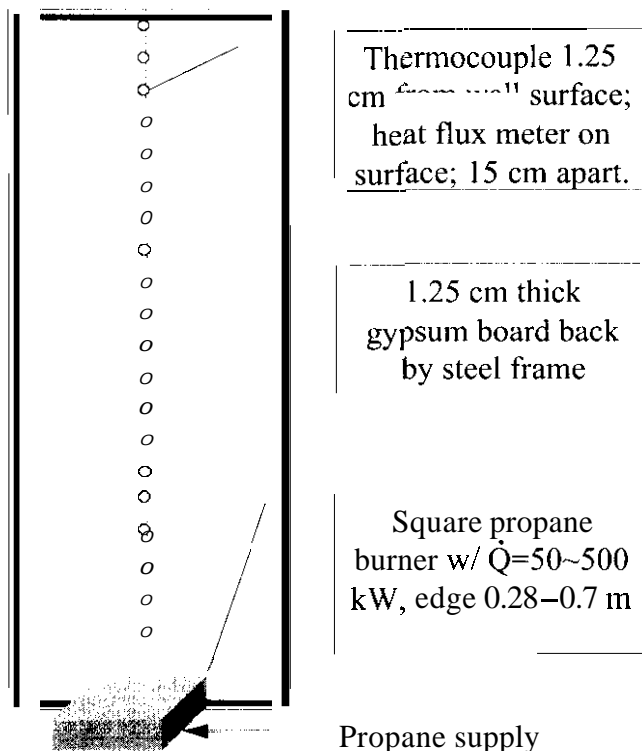


Figure 6. Temperature dependence on grid size.

Wall fires. The next task was to investigate the accuracy of the FDS code in predicting the heat transfer to wall subject to an adjacent pool fire. The experiments of Back et al. served as an experimental basis. The experimental arrangement is shown in Figure 7. The predicted heat flux was in fair agreement with the magnitude



of the measured values, but was distributed too tightly as shown in Figure 8. However, the flame height was reasonably predicted according to Figure 9. This is attributed to the over prediction of the temperature in the region closest to the burner. The same results characterize the free plume predictions. It appears where more fuel exists the burn rate is too high, but the distribution of burning occurs over the proper region. This might be interpreted that burning rate in the cell is too high in fuel rich regions, but the coarse scale mixing of the fuel and air is consistent and a good prediction of flame height results.

Figure 7. Wall heat flux measurements.

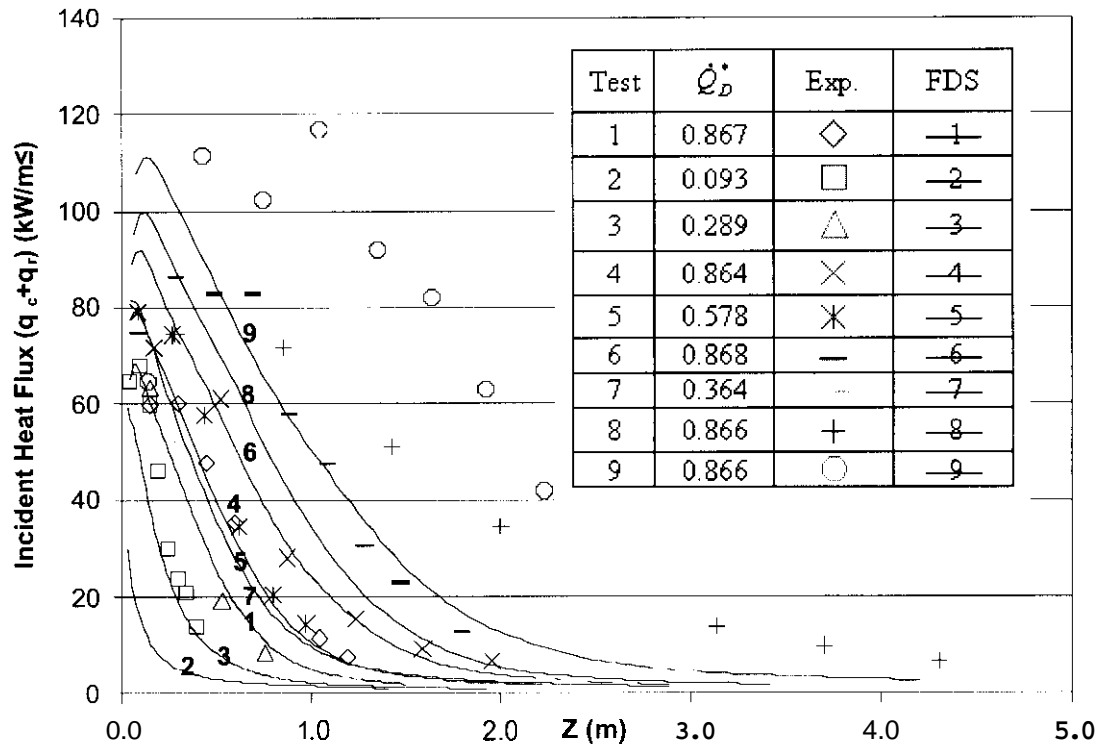


Figure 8. Wall heat flux comparisons for FDS and measurements.

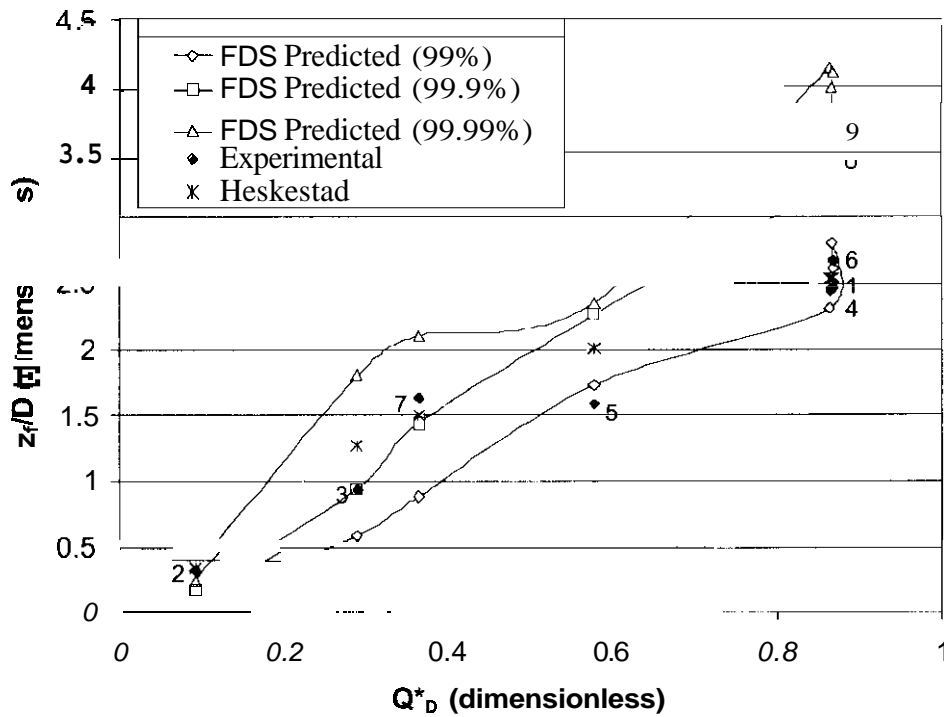


Figure 9. Flame height for burning fire against a wall.

Flame Spread. The flame spread computations were compared to vertical spread over a 5 m slab of PMMA. These experiments were conducted by FMRC. There was some difficulty in simulating the ignition process, and the modeling of this was obverted. Instead, synchronizing at a low energy rate indicative of the incipient fire began the comparison. The experimental arrangement is shown in Figure 10. The comparisons for the spread rate and energy release rate during spread are shown in

Figures 11 and 12, respectively.

The predictions are very good. However, a comparison at the quasi-steady burning rate once all of the 5 m was burning shows higher burning rates than measurements in Figure 13. The measurements were not taken from the flame-spread experiments since none were measured there. The measurements were taken from a 1.2 m tall PMMA study by Orloff. Estimates were also made from a correlation developed by Ahmad and Faeth. When a smaller vertical slab of PMMA was modeled, we believe this higher heat flux contributed to a “runaway” causing an accelerating spread rate, and termination of the run. That result is shown in Figure 14 along with a prediction from the SOFIE code.

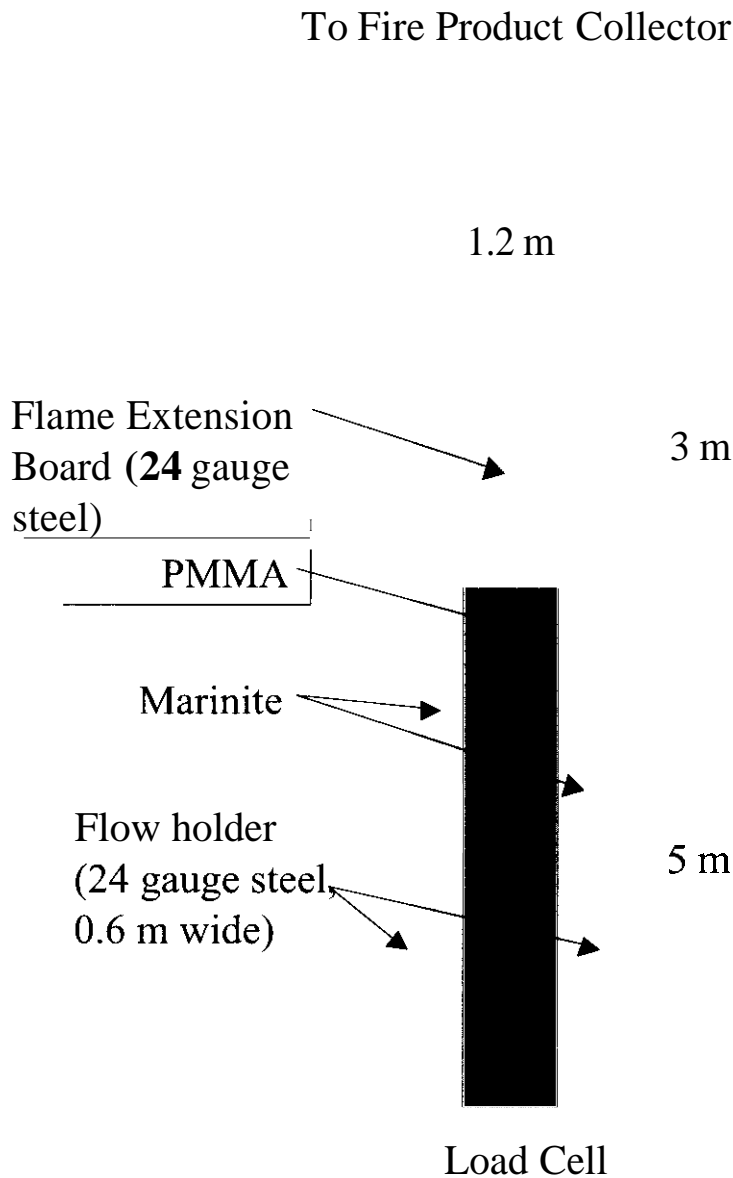


Figure 10. Flame spread experiment

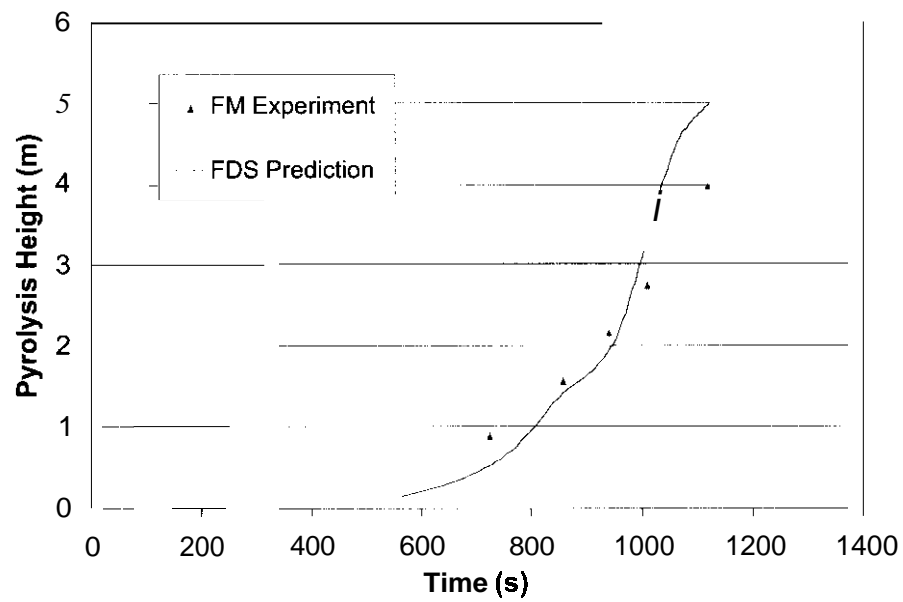


Figure 11. Flame spread rate comparisons.

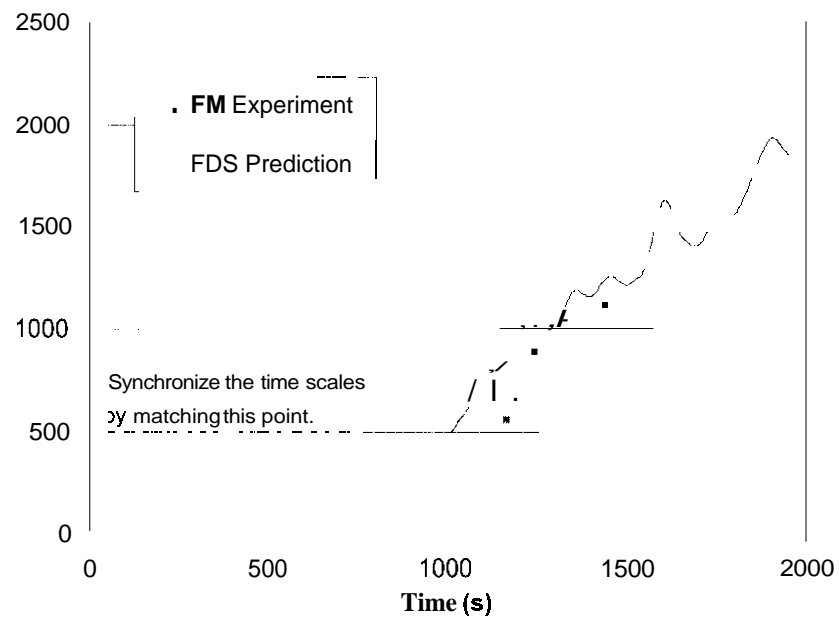


Figure 12. Energy release rate comparison.

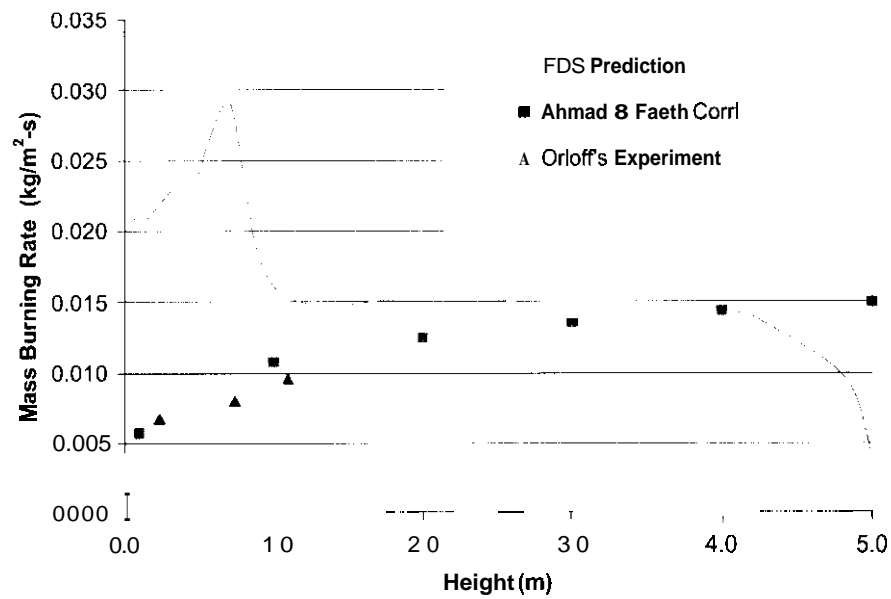


Figure 13. Burning rate comparison.

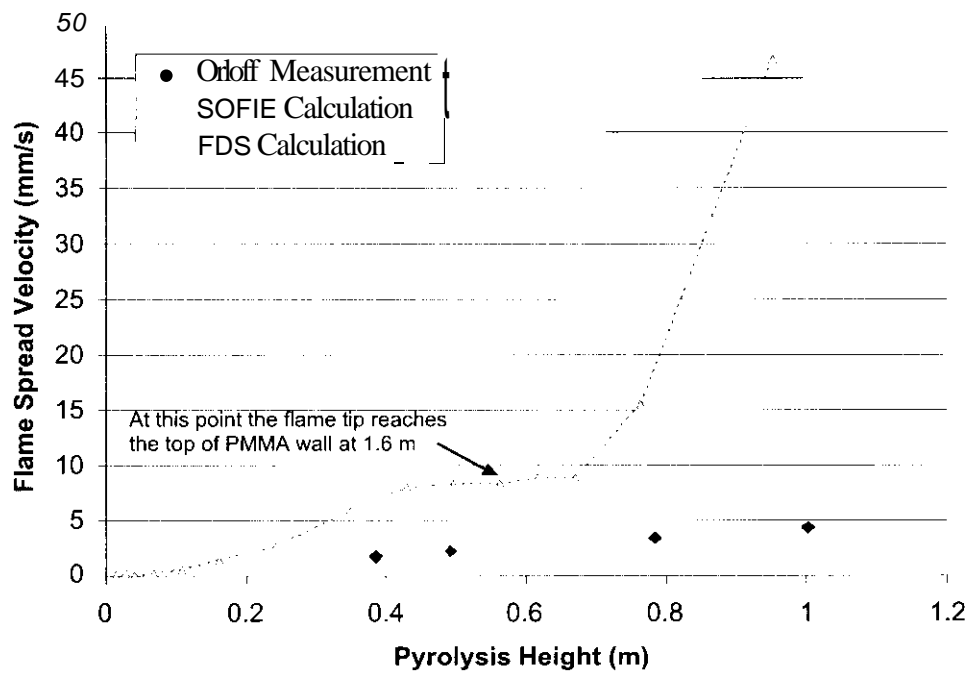


Figure 14. Prediction for spread on 1 m vertical PMMA

Convection heat transfer at the wall. A sub-task of this work was to examine a method to improve the convective heat transfer at the wall. Currently the code uses a standard heat transfer correlation. The improved algorithm was based on a model of Howard Baum that solved the exact unsteady energy equation with a uniform velocity parallel to the wall based on the closest grid cell. This is depicted in Figure 15. Damian Rouson examined the model, and an algorithm was developed. Comparisons were also made with exact solutions.

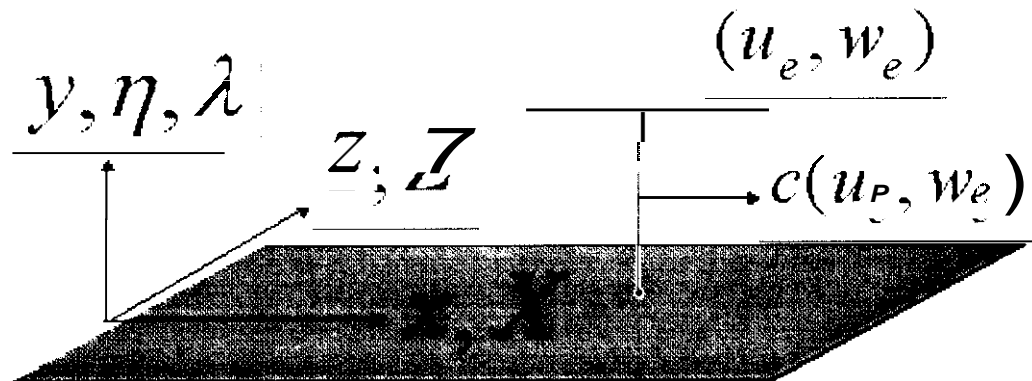


Figure 15. Convection at the wall.

Concluding Remarks. Details of the findings are found in the following Sections. They should be examined for a complete understanding of the analyses. In general, our experience with the current FDS code was good in terms of its ability to make predictions. The weak point appears to be the combustion model that causes higher temperatures and heat fluxes due to the fire, especially in the fuel rich region. The predictions for flame height were good suggesting an accurate representation of the “unmixedness” character of turbulent fires. The thermal and fluid dynamics outside the combustion zone appeared to yield good results for a free fire plume. While one application of flame spread gave good results, another produced an incorrect “runaway” condition. However, the runaway is not inconsistent with the physics of upward flame spread

NUMERICAL SIMULATION OF AXI-SYMMETRIC FIRE PLUMES: ACCURACY AND LIMITATIONS

T. G. Ma and J. G. Quintiere

Numerical Simulation of Axi-symmetric Fire Plumes: Accuracy and Limitations

T.G. Ma & J.G. Quintiere

Dept. of Fire Protection Engineering
University of Maryland, MD20742, USA

Abstract:

The objective of this work has been to determine the accuracy and limitations of a new version of Fire Dynamics Simulator (FDS), developed by McGrattan et al., on axi-symmetric fire plumes. The current version uses LES for turbulence, a mixture-fraction-based infinitely fast chemistry model for combustion, and a constant radiative loss fraction. These sub-models have been tested for unconfined fires of different sizes, based on a dimensionless heat release rate Q_D^* in the range of 0.1 to 10.0, which covers most natural fire scenarios. No adjustment of constants or algorithms in the model FDS2.0 have been made. An examination of plume theory is made first to find the benchmark correlations. This shows a generalization for a collection of correlations based on theory, and which might be “the best”. Using the characteristic length as the scaling factor, it is found that the optimum resolution of a pool fire simulation is around 0.05. With this resolution, the flame height prediction is found to fit well with flame height correlations. Some other parameters such as temperature and mixture fraction are found to be close to the empirical estimations at flame tips. The Froude number, which describes the relative strength of momentum and buoyancy, falls within the measurement range of many researchers. The simulation also reveals that the temperature near the burner is over-predicted, while the centerline temperature and velocity in the non-combusting region is predicted well.

Keywords:

Fire plume dynamics, flame height, entrainment, large eddy simulation

LIST OF ABBREVIATIONS

Nomenclature

c_p	specific heat of air (J/gK)
C	constant in FDs to adjust the stoichiometric mixture for grid size, equation 4b.
C_T	constant for temperature distribution in plume region
C_V	constant for velocity distribution in plume region
$C_{T,f}$	constant for maximum temperature in flame region
D	effective diameter of burner/ species diffusivity
D^*	the local characteristic length with reference to gridsize
z_f	flame height (m)
I	radiation intensity
I_b	radiation blackbody intensity
\dot{m}''	fuel mass loss rate per unit area (kg/s/m ²)
n	entrainment number, the ratio of flame entrained air to stoichiometric air needed.
N	dimensionless group for fire power, equation (3)
\dot{Q}	fire power (kW)
Q_b^*	non-dimensional heat release rate based on burner diameter
\dot{q}'''	heat release rate per unit volume, HRRPUV (kW/m ³)
R^*	resolution of simulation, gridsize/ z^*
T	temperature (°C)
t	time (s)
U	integrated radiant intensity (kW/m ²)
u,v,w	directional velocities (m/s)
x,y,z	spatial coordinates
s	stoichiometric oxygen/fuel mass ratio
s_a	stoichiometric air/fuel mass ratio
X_r	Radiative Loss Fraction
Y_F	mass fraction of fuel
Y_O	mass fraction of oxygen
z	vertical coordinates
z_f	flame height
Z	mixture fraction
Z_f	averaged mixture fraction at flame tip
Z_{st}	stoichiometric mixture fraction at flame sheet
Z_{eff}	effective mixture fraction at flame tip
z	the characteristic length of the fire with reference to the source diameter
Ah	fuel heat of combustion (kJ/kg)
$Ah_{,,}$	energy released per unit mass oxygen consumed

κ absorption coefficient (m^{-1})
 ρ density (kg/m^3)

1. Introduction

As a basic phenomenon, the buoyant plume has always attracted attention throughout fire research history. A lot of investigators have contributed to the fire plume research with well-designed experiments. Among them, Morton et al.^[11], Yokoi^[12], Thomas et al.^[13], McCaffrey^[14], Zukoski et al.^[15], Hasemi et al.^[16], Cox et al.^[17], Heskestad^[18], Delichatsios^[19], Kung et al.^[10], Hamins et al.^[11], etc., made significant contributions to the plume theory and its understanding. These studies represent simple physical Froude modeling and dimensional analysis to model buoyant turbulent fires. Most of these contributions were summarized by Beyler^[12], McCaffrey^[13], Heskestad^[14], Delichatsios^[15], Zukoski^[16], and most recently Quintiere et al.^[17].

With the advancement of computer technology and computational methods, more and more research work shifted to the numerical simulation of fire plumes. Most numerical simulations are based on the $k - \epsilon$ turbulence model (Reynolds average simulations, RAS). Tamanini^[18] used an improved version of the $k - \epsilon - g$ model of turbulence to simulate buoyancy controlled turbulent diffusion flames. His combustion model is infinitely fast chemical kinetics and local radiant emission is simplified to be a constant fraction of total energy. You and Faeth^[19] used a model similar to Tamanini's $k - \epsilon - g$ model, only lessening the effect of buoyancy, applied to flow which buoyancy and low Reynolds number effects were small. They provided the most complete comparison between prediction and experiment in buoyant flames. Crauford et al.^[20] used $k - \epsilon$ model and flamelet combustion to simulate a 25 cm turbulent natural gas flame. Adiga^[21] used the $k - \epsilon$ model and eddy-dissipation concept for combustion. His radiation model is based on the flux model and temperature-weighted gray gas model. Both used a parabolic flow field assumption.

Beginning in the late 1980's, some general-purpose commercial CFD codes were available in the market. Some of them were modified and applied in fire research, such as JASMINE, KAMELEON, FLUENT, and SOFIE, etc. It is pointed out^[22], the $k - \epsilon$ models tend to over-predict velocities and temperatures along the centerline axis of buoyant plumes and consequently under-predicts the plume width. Some suggestions were made, such as using the Algebraic Stress Model (ASM), to account for the influence of buoyancy. Nam and Bill^[23] modified the standard $k - \epsilon$ model in PHOENICS by adjusting its constants to study the pure thermal plume above the flame region. No combustion model was used. The velocity half-width based on velocity and temperature was then compared with those of standard $k - \epsilon$ model and experimental data of large fires by Kung et al.^[10]. This study^[23] is part of a research program devoted to numerical simulation of the interaction of fire and sprinkler spray. Sinai et al.^[24] used FLOW3D to model the unconfined pool fires with emphasis on the flame geometry above a round 20 m kerosene pool fire subjected to a crosswind. The role of the pool shape and ambient turbulence has been investigated. His model is based on the buoyancy-modified $k - \epsilon$ turbulence formulation, the Eddy Break-up combustion model and a gray-medium representation of thermal radiation. Miles et al.^[25] used JASMINE to estimate air entrainment into buoyant balcony spill plumes. It concerns the numerical simulation of a reduced scale physical model. Excellent agreement between

measured and predicted mass fluxes is demonstrated in the regions of low heights of plume rise, but the two apparently diverge at greater heights of plume rise.

Currently, the development of a computational fire dynamics code is underway at NIST. The code, Fire Dynamics Simulator (FDS), including its visualization tool, SMOKEVIEW, is looked to as the future research tool for fire investigation^[26]. It is based on a Large Eddy Simulation (LES) with a Smagorinsky turbulence sub-model. The hydraulics equations were initially developed by Baum and Rehm^[27]. The general usage and application of the code has been reported by McGrattan et al.^[28]. This code has been used to study the isolated plume dynamics^[29]. The combustion model used there is based on simulating the combustion by releasing energy from Lagrangian thermal element. The radiation is simulated through ray-tracing from each thermal element. A 45 kW pool fire plume is simulated. The agreement is remarkably good in the intermittent flame and plume region, but not in the continuous flame region. Since the energy release from the fuel particles was uniform in time, dense particles near the burner surface caused the temperature to be over-predicted. This discrepancy limits the application of the code in predicting flame heat flux, and also in its general use for fire spread prediction.

Based the need for improvement in predicting flame heat flux, an alternative combustion model has been realized in the code by McGrattan et al.^[30]. The new combustion model is based on infinitely fast chemistry and mixture fraction. A new radiative model using Finite Volume Method (FVM) for radiation transfer was also incorporated. In order to evaluate this new model for general applications in fire growth, it was decided to investigate the axi-symmetric fire plume since it was extensively studied. However, since the experimental data are too abundant and not easily accessible, a review of existing correlations is made to determine the most representative and accurate approach to use for these properties. A series of simulations were carried out in order to determine these gross fire plume properties, e.g. the centerline time-averaged Froude number, temperature, and flame height, etc.

2. Methodology

Here we briefly summarize the new models adopted in the code, which is supplied by McGrattan et al.^[30].

2.1. Hydrodynamic and Turbulence Model

Details of the hydrodynamics and turbulence model are supplied in^{[28][29]}. For the current study, the fundamentals of Large Eddy Simulation are unchanged.

2.2. Combustion Model

The new combustion model used here is based on mixture-fraction based infinitely fast chemistry kinetics. The general form of the combustion reaction is,



The mixture fraction Z is defined^{[77][80]} as,

$$Z = \frac{sY_F - (Y_O - Y_O^\infty)}{sY_F^\infty + Y_O^\infty} ; s = \frac{v_O M_O}{v_F M_F} \quad (2)$$

The mixture fraction satisfies the conservation law

$$\rho \frac{DZ}{Dt} = \nabla \cdot \rho D \nabla Z \quad (3)$$

The assumption that the chemistry is "fast" means that the reactions that consume fuel and oxidizer occur so rapidly that the fuel and oxidizer cannot co-exist. The flame sheet is the location where fuel and oxidizer vanish simultaneously.

$$Z_f = Z_{st} = \frac{Y_O^\infty}{sY_F^\infty + Y_O^\infty} \quad (4a)$$

When dealing with a wide range of fire, this definition is not enough to produce the correct flame height. Sometimes the code may not have enough resolution to capture the combustion and relating dynamics. An effective Z , is proposed to help the code capture the combusting region.

$$\frac{Z_{f,eff}}{Z_f} = \min\left(1, C \cdot \frac{D^*}{\delta x}\right), \quad (4b)$$

Here C is an empirical constant to be used for all fire scenarios (here it is 0.025 in FDS2.0), δx is the grid size and D^* ($=z^*$ herein) is the local characteristic length of the fire, used as a reference length. As the resolution of the calculation increases, the effective $Z_{f,eff}$ will approach the ideal value, Z_f of equation (4a). The benefit of the expression is that it provides a quantifiable measure of the grid resolution that takes into account not only the size of the grid cells, but also the size of the fire.

The mixture fraction is a dimensionless value so it cannot decide the species distribution alone. A state relation for oxygen is needed. The ideal state relation for oxygen is introduced based on the assumption that fuel and oxidizer cannot co-exist.

$$\text{For } Z < Z_f, Y_O(Z) = Y_O^\infty \left(1 - \frac{Z}{Z_{eff}}\right) \quad (5a)$$

$$\text{For } Z > Z_f, Y_O(Z) = 0 \quad (5b)$$

The heat release rate per unit volume is based on Huggett's relationship^[43] of oxygen consumption, where Δh_o is assumed constant for most fuels.

$$\dot{q}''' = \Delta h_o \dot{m}_o''' \quad (6)$$

where the mass burning rate is based on the oxygen consumption rate given as,

$$-\dot{m}_o''' = \nabla \cdot \left(\rho D \frac{dY_o}{dZ} \nabla Z \right) - \frac{dY_o}{dZ} \nabla \cdot \rho D \nabla Z \quad (7)$$

The ability to predict the ∇Z over the cell is a reason for equation (4b).

Specifically for our fire simulation, by default in the code, we can have the following diagram showing the relationship between species for fires of a typical fuel, propane. Here $\Delta h_o = 13.1$ MW/kg is used for propane.

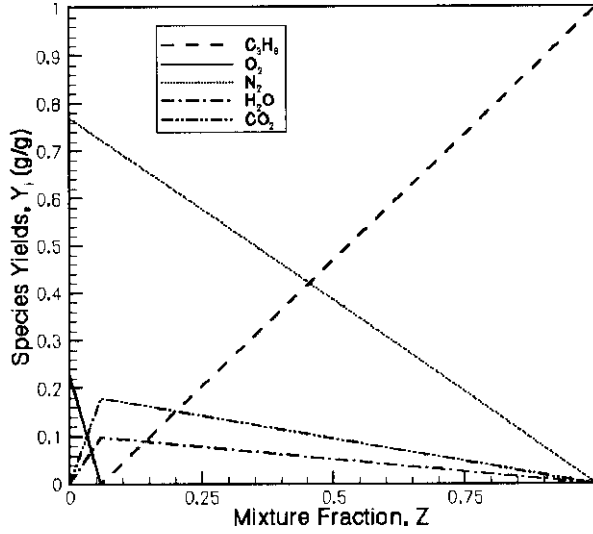


Figure I. Relationship of mixture fraction and species concentration for propane

2.3. Radiation Model

The Radiative Transport Equation (RTE) for a non-scattering gray gas is

$$\mathbf{r} \cdot \nabla I(\mathbf{x}, \mathbf{r}) = \kappa(\mathbf{x}) [I_b(\mathbf{x}, \mathbf{r}) - I(\mathbf{x}, \mathbf{r})] \quad (8)$$

Where $I(\mathbf{x}, \mathbf{r})$ is the radiant heat flux, $I_b(\mathbf{x}, \mathbf{r})$ is the blackbody radiation intensity, \mathbf{s} is the unit normal direction vector and $\kappa(\mathbf{r})$ is the gray-gas absorption coefficient. The radiative loss term in the energy equation is

$$-\nabla \cdot \mathbf{q}_r(\mathbf{x}) = \kappa(\mathbf{x}) \cdot [U(\mathbf{x}) - 4\pi I_b(\mathbf{x})], \quad U(\mathbf{x}) = \int I(\mathbf{x}, \mathbf{r}) d\Omega \quad (9)$$

The net radiant energy gained by a grid cell is the difference between that which is absorbed and that which is emitted. The source term is defined as

$$\kappa I_b = \begin{cases} \kappa \sigma T^4 / \pi, & \text{Outside} \\ \chi_r \dot{q}''' / 4\pi, & \text{Inside} \end{cases} \quad (10)$$

Here \dot{q}''' is the chemical heat release rate per unit volume and χ_r is the local fraction of the energy emitted as thermal radiation. The radiant heat flux vector \mathbf{q}_r is defined

$$\mathbf{q}_r(\mathbf{x}) = \int \mathbf{s} I(\mathbf{x}, \mathbf{s}) d\Omega \quad (11)$$

Through the simulations, we use the default parameters for radiation calculation, since we have no better experimental result on radiation prediction in flames.

3. Plume Theory and Benchmark Correlations

There has been some work done with FDS on isolated fire plumes^[28]. Our purpose is to examine the code for a wide range of fire plumes. The former needs a specific fire experiment while the latter needs general experimental correlations for comparison. In the following, plume theory will be used to extend existing correlations to a more complete and accurate representation of data. While some specific

correlations are considered, it should not be inferred that others not considered are inferior.

3.1. Scaling of Fire Phenomena

The appropriate scaling parameters for most of the features of fire plumes have not been universally established by all investigators. However, the scaling laws for the size of the diffusion flames have been developed by a number of authors, and some consensus has been reached that a dimensionless fire power^[31],

$$Q_D^* = \frac{\dot{Q}}{\rho_\infty c_p T_\infty \sqrt{g D D^2}} \quad (12)$$

or a dimensional parameter that is proportional to Q_D^* , such as $\dot{Q}/D^{5/2}$ can be used as the scaling parameter. Flame-length data discussed by Zukoski^[18] and Hasemi^[6] indicate that scaling laws for the visible flame length, and possibly for other parameters of interest including the entrainment rate, have a different functional form for several ranges of Q_D^* , and must be considered separately for each regime.

It is also pointed out by Heskestad^[32] that Q_D^* does not appear to be a sufficient scaling parameter for the flaming region. Flame height measurements data support a new scaling parameter N.

$$N = \frac{c_p T_\infty}{g \rho_\infty \left(\frac{\Delta h_c}{s_a}\right)^3} \cdot \frac{\dot{Q}^2}{D^5} = \left(\frac{c_p T_\infty}{\Delta h_c / s_a} \right)^3 (Q_D^*)^2 \quad (13)$$

In practice, the distinction from Q_D^* is important mainly when atmospheric conditions differ significantly from standard. So here we still rely on Q_D^* as the scaling parameter.

According to Hasemi et al.^[33], natural fires always fall into the range of $Q_D^* = 0.1$ to $Q_D^* = 10.0$. Figure 2 summarizes the correlation between fuel size and Q_D^* for typical natural fires in unconfined environments. This demonstrates that the range of Q_D^* for most building combustible objects with the size of 0.1-2 m is approximately 0.3-3.0, whereas measurements of the plume properties have been made mostly for a wider range of Q_D^* . In order to investigate the significance of the flame geometry on the plume properties, Hasemi et al.^[6] measured the centerline and the radial distribution of temperature and upward velocity on porous round burners with propane as the fuel for $0.4 < Q_D^* < 4.0$. Here our computed simulation range is $0.1 < Q_D^* < 10.0$, which covers the range of Q_D^* for most common fires. In order to develop the appropriate theoretical basis for the general dimensionless correlations, we will examine specific fire plume features.

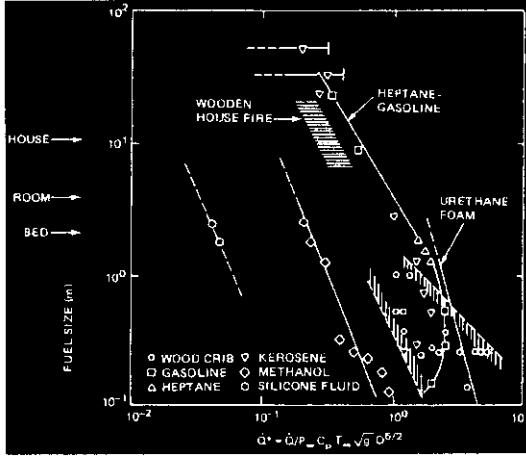


Figure 2. Dimensionless \dot{Q}_D^* for most natural fires'''

3.2. Plume Froude Number

An inviscid Bernoulli equation analysis for the center streamline of a buoyant plume with a uniform surrounding atmosphere at T_∞ gives,

$$\frac{\rho w^2}{2} + p + \rho g z = p(0) \quad (14)$$

The atmosphere imposes the pressure as,

$$p(0) - p = \rho_\infty g z \quad (15)$$

And since the pressure is nearly constant, the perfect gas law gives

$$\rho T = \rho_\infty T_\infty \quad (16)$$

so we have

$$w^2 = 2 \left(\frac{\rho_\infty - \rho}{\rho} \right) g z = 2 \left(\frac{T - T_\infty}{T_\infty} \right) g z \quad (17a)$$

Or,

$$Fr = \frac{w^2}{\left(\frac{T - T_\infty}{T_\infty} \right) g z} = 2 \quad (17b)$$

This gives the inviscid steady value along the centerline a buoyant plume. In a review of real fire plume data, Beyler^[12] summarized many experimental results and found the plume centerline Froude number ranged from about 1.16 to 2.0 for a wide range of data with an average of about 1.5 in the non-combusting and flame intermittent region. Quintiere and Grove^[17] have shown that $Fr = 1.5 \pm 0.1$ for both line and axisymmetric fire plumes along the centerline in their entire domain, combusting and non-combusting regions. Heskestad^[32] uses an alternative parameter defined as $\xi = (9.1)^{0.3} \cdot Fr^{1/2}$ in the non-combusting plume region. This value is found to be 2.2

(Heskestad ^[32]), 2.7 (McCaffrey ^[4]), **2.4** (Kung et al. ^[10]) corresponding to a range of Fr from 1.29 to 1.94.

It appears that a multitude of data from fire plumes suggest a fairly constant time-averaged Fr along the centerline. Since it ties the velocity directly to the temperature change, it is a valuable feature and useful tool in fire induced flow research. The approximate constancy of Fr also suggests a small and uniform departure of real fires from inviscid flow.

3.3. Centerline Temperature and Velocity

Dimensional analysis of the governing equations can show that the centerline plume temperature satisfies

$$\frac{T - T_\infty}{T_\infty} = f(X_r, z/z^*, D/z^*) \quad (18)$$

where

$$z^* = \left(\frac{\dot{Q}}{\rho_\infty c_p T_\infty \sqrt{g}} \right)^{2/5} = (\dot{Q}_D^*)^{1/5} \cdot D \quad (19)$$

is a characteristic plume length scale, and D is the effective diameter of the fuel source (the diameter of the circle with an equivalent area). Theoretical analysis ^[16] can show the general power-law form of this relationship in the combusting and the non-combusting regions of the plume. The coefficients in these relationships must be set from experimental data.

In the non-combusting plume region, Heskestad ^[4] developed a relationship in terms of a virtual origin z_0 , offset below the base of the fire, to account for the dependence on D:

i.e. for $z > z_f$,

$$\frac{T - T_\infty}{T_\infty} = C_T (1 - X_r)^{1/3} \left(\frac{z - z_0}{z^*} \right)^{-5/3} \quad (20)$$

where

$$\frac{z_0}{z^*} = -1.02 \frac{D}{z^*} + 1.37 \quad (21)$$

gives the virtual origin. Heskestad ^[14] obtained $C_T = 9.1$ for the domain of pool fires, $0.04 \leq \dot{Q}_D^* \leq 2.0$, $\dot{Q}_D^* = (z^*/D)^{5/2}$. Quintiere and Grove ^[17] found $C_T = 10.6$ based on far field data of Yokoi ^[2], and this variation suggests the current level of uncertainty in C_T .

From the constancy of Fr, the centerline dimensionless velocity can be consistently written as

$$W = \frac{w}{T_\infty} = C_v (1 - X_r)^{1/3} \left(\frac{z - z_0}{z^*} \right) \quad (22)$$

where C_v is 3.4 according to Heskestad^[14], or 4.17 from Quintiere and Grove^[17]

For the combusting region, it is assumed that the entrainment rate of air into the plume controls the burning rate. With the similar turbulent mixing effects, the fire consumes the same fraction of stoichiometric air. The entrained air is about 10 times of the stoichiometric air^[17]. A theoretical analysis based on these assumptions leads to a constant centerline temperature in the fire region. Accordingly,

$$\frac{T - T_\infty}{T_\infty} = C_{T,f}(1 - X_r) \left(\frac{\Delta h_c / s_a}{c_p T_\infty} \right) \quad (23)$$

where $C_{T,f}$ is a constant dependent on a fit to data. After checking Table 1 for selected centerline flame temperatures, chosen for accuracy and fuel range, an estimate of $C_{T,f} = 0.50$ is a good choice. For the propane fuel in our simulation, the temperature is estimated as 1041°C in the flaming region.

Table 1. Maximum accurately measured centerline flame temperatures.

Max. Aver. Central Temp. °C	Fuel	$\Delta h_c / s_a$ kJ/g air	D (m)	\dot{Q} (kW)	X_r	Source	$C_{T,f}$
1260	Nat. Gas	2.91	0.3	17.9	0.15	Smith et. al. ^[33]	0.50
1100	Nat. Gas	2.91	0.3	70.1	0.25	Smith et. al. ^[33]	0.48
930	Heptane	2.96	1.74	7713	0.43	Kung et. al. ^[10]	0.52
990	Methanol	3.07	1.74	973	0.18	Kung et. al. ^[10]	0.59

This result should serve as an approximate benchmark in the combusting region to assess the accuracy of both predictive and experimental results. The radiation fraction is a significant factor, and it probably represents the most complex phenomena. The value of X_r is difficult to measure and will vary, depending on fuel type and fire diameter. A fundamental predictive model for X_r would require more detailed data and be capable of resolving distributions for flame properties.

3.4. Flame Height

Numerous correlations exist for flame height, and some are summarized in the **SFPE Handbook**^[13]. Usually, flame height correlations are produced under a specific situation and offer independent results from each other. Among them, Heskestad's^[18] expression is easy to use and Zukoski's^[26] expression is based on consistent data. Heskestad gives:

$$\frac{z_f}{D} = 15.6 \cdot \frac{Q_D^{*2/5}}{\left(\frac{\Delta h_c / s_a}{c_p T_\infty} \right)} - 1.02 \quad (24)$$

which is commonly presented as

$$\frac{z_f}{D} = 3.88 \cdot Q_D^{*2/5} - 1.02, \quad \text{for } \Delta h_c / s_a = 2.975 \text{ kJ/g} . \quad (25)$$

Based on the three data regimes characterized by Q_D^* , Zukoski developed

$$\frac{z_f}{D} = 40 \cdot Q_D^{*2}, \text{ for } 0.03 \leq Q_D^* < 0.15 \quad (26a)$$

$$\frac{z_f}{D} = 3.3 \cdot Q_D^{*2/3}, \text{ for } 0.15 \leq Q_D^* \leq 1.0 \quad (26b)$$

$$\frac{z_f}{D} = 3.3 \cdot Q_D^{*2/5}, \text{ for } 1.0 < Q_D^* < 40.0 \quad (26c)$$

Both correlations (equation (24)(26)) ignore the effect of flame radiation. Hamins et al.^[11] attempted to include this effect with an empirical inclusion of X_r . They obtained

$$\frac{z_f}{D} = 18.5 \cdot \frac{Q_D^{*2/5} (1 - X_r)^{2/5}}{\left(\frac{\Delta h_c / s_a}{c_p T_\infty} \right)^{3/5}} - 1.06 \quad (27)$$

This expression does not contain the correct dependence for X_r according to the theory of Quintiere and Grove^[17]. They theoretically derived the effect of radiation and found an implicit expression for flame height.

$$\left(\frac{z_f}{D} \right)^{1/2} \left(1 + 0.357 \frac{z_f}{D} \right)^2 = 169.5 \cdot \frac{Q_D^*}{\left(\frac{\Delta h_c / s_a}{c_p T_\infty} \right)^{3/2} (1 - X_r)^{1/2}} \quad (28)$$

For $z_f / D > 0.1$, the LHS can be approximated as $\left(0.775 + 0.463 \frac{z_f}{D} \right)^{5/2}$, giving

$$\frac{z_f}{D} \approx 16.8 \cdot \frac{Q_D^{*2/5}}{\left(\frac{\Delta h_c / s_a}{c_p T_\infty} \right)^{3/5} (1 - X_r)^{1/5}} - 1.67 \quad (29)$$

This has the form of Equations (24) and (26). It would appear that radiation does not have a strong effect on flame height. However, it has the opposite trend in Hamins' result. Qualitatively, as X_r increases, the flame temperature, velocity and entrainment rate should decrease, and therefore the flame height should increase as more air is available for combustion.

For $z_f / D < 0.1$, the LHS of Equation (29) can be approximated as $(z_f / D)^{1/2}$, therefore

$$\frac{z_f}{D} \approx 2.873 \times 10^4 \frac{Q_D^{*2}}{\left(\frac{\Delta h_c / s_a}{c_p T_\infty} \right)^3 (1 - X_r)} \quad (30)$$

or using $\Delta h_c / s_a = 2.975 \text{ kJ/g}$

$$\frac{\dot{m}_f}{D} = \frac{2.75}{1 - X_r} Q_D^{*2}, \quad (31)$$

with the same form as Zukoski (equation 26c), but now including X_r .

The range of flame height data is about $0.05 \leq Q_D^* \leq 100$. All of these formulas give good accuracy above $Q_D^* = 1.0$. There is a larger disagreement among the formulas and a larger scatter of the data below $Q_D^* = 1.0$. We shall use Equations. (24), (26), and (29) as good representations of flame height (shown in Figure 3). In practice, we usually take the following parameters: $\Delta h_c / s_a = 2.975 \text{ kJ/g}$, $c_p = 1.0 \text{ kJ/kg} \cdot \text{K}$, $T_\infty = 298 \text{ K}$.

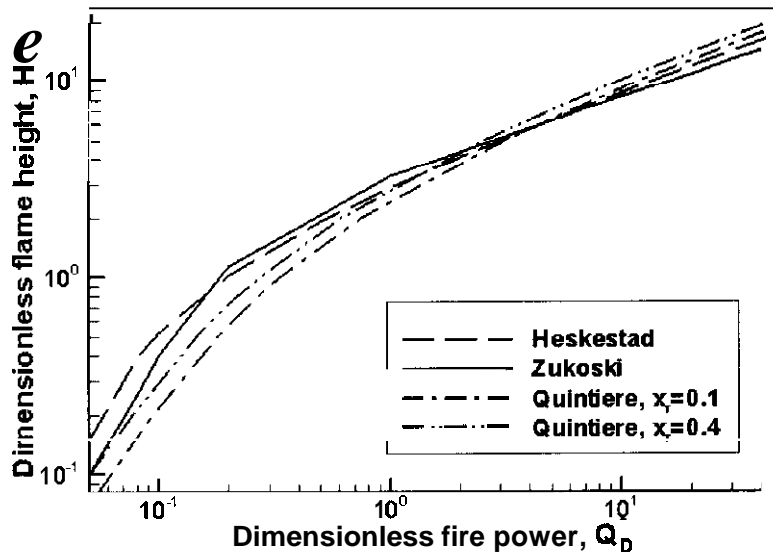


Figure 3. Comparison of Flame Height Correlations.

3.5. Entrainment number at flame tip

There is an important constant in relating the entrainment rate and flame height prediction. It is an empirical number, which has different values among different researchers due to different test methods or analyzing theories applied. This number, n , is the ratio of entrained air up to the flame tip with the stoichiometric air needed.

Some early research work on fire plume was performed by Yokoi^[2]. Roughly 12 times stoichiometric air at flame tip was deduced by McCaffrey and Cox^[45] from his temperature and velocity profiles.

In order to fit his combustion plume model to a large quantity of flame height data, Steward^[46] found that only 400% excess air was entrained up to the flame tip, i.e., the flame has entrained about 5 times the stoichiometric requirements.

Using $k - \epsilon - g$ model, Tamanini^[18] produced 9 times stoichiometric at flame tip. This value was thought to be low, due to the deficiencies in the treatment of large scale eddies near the point of transition to turbulence.

Zukoski's^[5] hood collection technique produced an equivalence ratio of $0.067 \pm 10\%$ measured value at flame tip, which yields about 15 times stoichiometric.

Based on point measurement techniques coupled to an integral model of the fluid dynamics behavior, McCaffrey and Cox^[45] got the number to be about 20 times the stoichiometric requirement.

$$\dot{m}_{e,f} = 0.007\dot{Q} \approx 20(s_a\dot{m}_f) \quad (32)$$

Beyler^[47] measured the entrainment rate using the hood technique. He got

$$\dot{m}_{e,f} / \dot{Q} = 0.045 \text{ kg/k/kW}, \quad (33)$$

representing about 13 times the stoichiometric air requirement of the flame.

Based on Zukoski's data on entrainment at flame tip, Heskestad^[48] assumed self-preserving density deficiency profiles instead of the assumption of self-preserving excess temperature profiles used by Cetegen et al.^[49] It is found that **12** times the mass stoichiometric air is required at the flame tip.

$$\dot{m}_{e,f} = 0.0054\dot{Q}_c = 0.0038(s_a\dot{m}_f)(\Delta h_c / s_a) \approx 12(s_a\dot{m}_f) \quad (34)$$

Using an apparatus similar to Ricou and Spalding^[50], Delichatsios and Orloff^[51] found that the air entrainment is about **10** times the stoichiometric requirements at the flame height of turbulent buoyant fires. This number had been used directly to derive the flame height correlations from the entrainment correlations^[9].

Examining a lot of data using an integral model approach, Quintiere et al.^[17] derived the entrainment and the flame height separately, and by comparison of coefficients, found $n=9.6$ for both axi-symmetric and linear plumes.

Hence, the range of n is found to be 10 ± 5 .

4. Simulation Results

4.1. Simulation Summary

Generally in fire research, a circular burner is used more widely than a square burner which is used in McCaffrey's experiments. Measurements by Hasemi et al.^[6] for square and round gas burners show little effect of the burner shape when for the square burners, D is taken as the diameter of a circular burner of equal area. Subsequent measurements of Hasemi and Nishita^[35] have indicated tendencies to slightly higher flame-height ratio than circular burner data for small fires. Investigation by Orloff^{[36][37]} revealed that the height of a peripheral rim or lip above the surface of a circular pool fire affects the burning rate and flame shape, but has little effect on the flame height (except through Q_D^*). Other geometric effects on flames have attracted attention. Without further comment, these include interactions with ceilings, interaction with walls and corners, and interaction/merging of proximate flames.

Here for the numerical plume simulation, we are dealing with an unconfined, free burning, square burner surface, no rim or lip, pool fire with propane as typical fuel, and with fire sizes ranging from $Q_D^* = 0.1$ to 10.0. (For our 0.3x0.3m square burner, the fire size ranges from 7.37 kW to 737 kW). Unless stated, all simulations are based on constant radiative loss fraction ($X_r = 0.35$). The mass flow rate of the propane was specified **and** supplied with uniform velocity. The platform for the simulation is the

Pentium IV, 2.0GHz, 1GB RAM, and Windows 2000. All cases are run for 10 seconds of simulation with last 4 seconds for steady state averaging.

Table 2. List of simulation inputs

Q*	Grids	Q(input)	z*	Grid	R*	Q(out)	Error_Q	Run_time
		kW	m	cm		kW		hrs
0.10	64x64x64	7.37	0.13	0.69	0.0510	7.33	-0.01	3.91
0.20	64x64x48	14.74	0.18	0.91	0.0510	14.49	-0.02	2.64
0.50	48x48x64	36.86	0.26	1.25	0.0487	37.41	0.01	2.29
0.80	32x32x96	58.98	0.31	1.56	0.0505	58.25	-0.01	1.39
1.00	32x32x80	73.72	0.34	1.69	0.0499	74.84	0.02	1.23
1.50	32x32x80	110.59	0.40	2.00	0.0502	114.79	0.04	1.19
2.00	32x32x96	147.45	0.45	2.25	0.0504	156.28	0.06	1.30
5.00	32x32x96	368.62	0.64	3.25	0.0504	413.25	0.12	1.08
8.00	32x32x96	589.79	0.78	3.88	0.0498	652.86	0.11	1.02
10.00	32x32x96	737.23	0.85	4.25	0.0500	803.10	0.09	0.98
0.30	48x48x144	22.12	0.21	1.05	0.0500	21.54	-0.03	5.07

As Zukoski^[4] pointed out, when $\dot{Q}_D^* < 0.10$, the combustion region is divided into many flamelets that lean toward the axis of the source and that have flame lengths much smaller than the diameter of the source. For values above 1.0, the flames are more than three diameters high and have a columnar form. In the middle regime the short flamelets merge as \dot{Q}_D^* increases and form a single short flame near $\dot{Q}_D^* = 0.1$. Here the simulations produced similar results as shown in Figure 4.

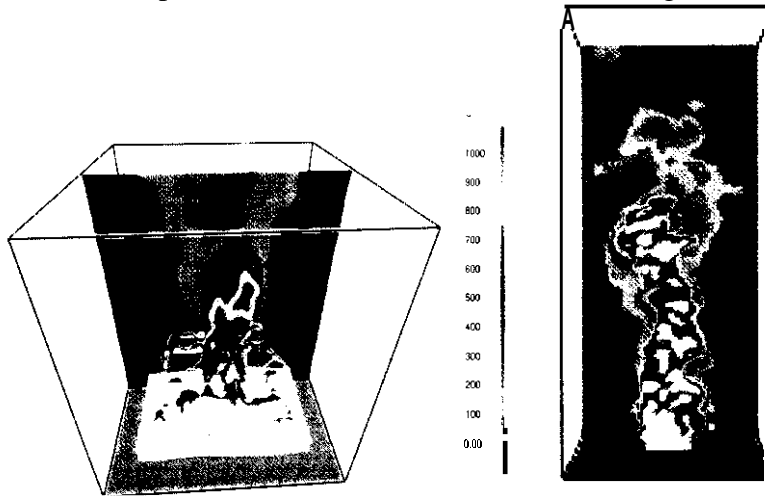


Figure 4. Snapshot of fire plume at $\dot{Q}_D^* = 0.20$ and $\dot{Q}_D^* = 10.0$

The reason that we could not show results for $\dot{Q}_D^* < 0.2$ fires here is that for very low fire intensity, the $Z = Z_{sl}$ contour will be very close to the burner, even for a very well resolved gridsize. As the cells get larger, the mixture fraction value at the burner

surface is too small to reach its stoichiometric value. Sometimes, for low enough Q_D^* , the $Z = Z_{eff}$ will be located inside the burner, which is invisible in **SMOKEVIEW**^[52], the visualization tool for FDS. We still can see the flame structure if a smaller mixture fraction value is used, but this has less physical meaning.

4.2. Flame Height

There are some different definitions of flame height. The averaged luminous flame height is generally defined as the height at which the flame is observed at or above that height 50% of the time^[16]. Hasemi's flame height was defined as the limit above which flame tips have never been observed by eye^[6]. Visual observation tends to yield slightly over-estimates of the 50% flame heights^[16]. Video image analysis seems to provide the best estimates though averaging a number of one-second exposure photographs. Cox and Chitty found the flame lengths from 3 seconds time exposure by photographs of fires^[7].

For our simulation, there are many parameters available that can serve as indicators of flame height, such as temperature, fuel concentration, mixture-fraction, or energy release, etc. Here we couldn't use 50% intermittency, as the frequency of fire pulsation is still not accurately resolved. Instead, we choose a more fundamental one, local energy release rate (\dot{Q}'''), as the parameter for flame height. For calculating the flame height, first we average the recorded slice file for \dot{Q}''' . Generally, we choose to average the frames of 4 s steady fire simulation. Then the \dot{Q}''' value was integrated over the combustion domain upwards from the burner surface. So we have an energy release rate as a function of height. The critical value for flame tip was considered as 95%, 99%, or 99.9%. After a series of simulations, we decided that 99% is a good indicator for flame height (Figure 5.). That is to say, our flame tip is defined as the level below which 99% of the chemical reaction occurred.

The impact of gridsize on simulation results is an important consideration for any CFD analysis. Generally, good CFD software should have a relative constant result in a certain gridsize range. Baum et al.^[29] suggested that to correctly capture the impact of burner surface, it is necessary to have 10x10 grids over the burner surface. Here since we are dealing with a wide range of fire intensity, this empirical rule is not enough. The choice of gridsize should reflect not only the impact of fire dimension, but also the fire size. The characteristic length, defined by equation (19), combines the impact from both burner diameter and the fire size, so it is widely used in fire research field. Here we can define the resolution of fire plume simulation as a dimensionless parameter,

$$R^* = \frac{\max(\delta x, \delta y, \delta z)}{z^*} \quad (35)$$

To simulate the fire correctly, non-uniform grid is allowed and the aspect ratio of grid size should not exceed 2. Here we have uniform grid size in all three dimensions in all runs, i.e. $\delta x = \delta y = \delta z$. The simulation resolutions for all cases are listed in Table 2.

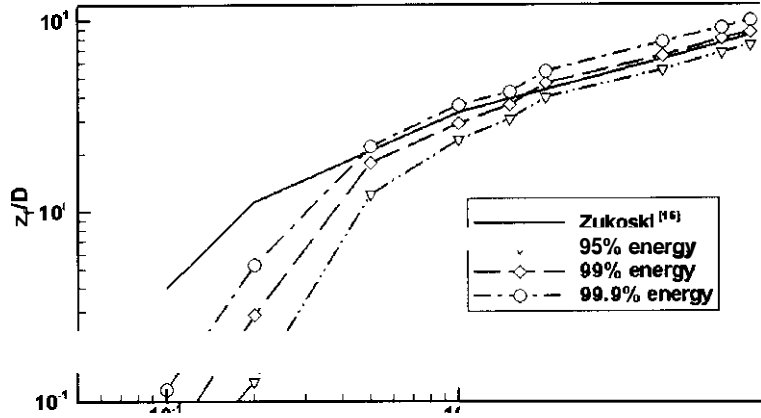


Figure 5. Flame height prediction as a function of combustion termination.

After a lot of simulation runs, the optimum resolution for flame height simulation was found to be $R^* = 0.05$. Above this value, the simulations tend to under-predict the flame height. Below, then the flame height is over-predicted. It is found ^[29] that the plume dynamics can only be accurately simulated if the resolution limit is about $R^* = 0.1$ or smaller. Our result is even strict. The flaming region has the chemical reactions and wide range of turbulence scales, so a finer grid size is needed.

A closer look at other critical parameters at the flame height (calculated using Zukoski's correlation) shows the following result (Figure 6.). For fires between $Q_D^* = 1.0$ to $Q_D^* = 10.0$, the temperature at flame height is about $T = 350$ °C, which is close to Zukoski's value. The critical mixture fraction $Z = 0.01$ is also close to the result calculated using equation 4(a). For small fires ($Q_D^* < 0.5$) the reaction happens only one or two grid cells from the burner surface, the high value at flame tip is caused mainly by diffusion alone, where the turbulence is low and the entrainment is not enough. The fire is more laminar-like, rather than turbulent. But the temperature prediction follows the correlation over a wide range of fires.

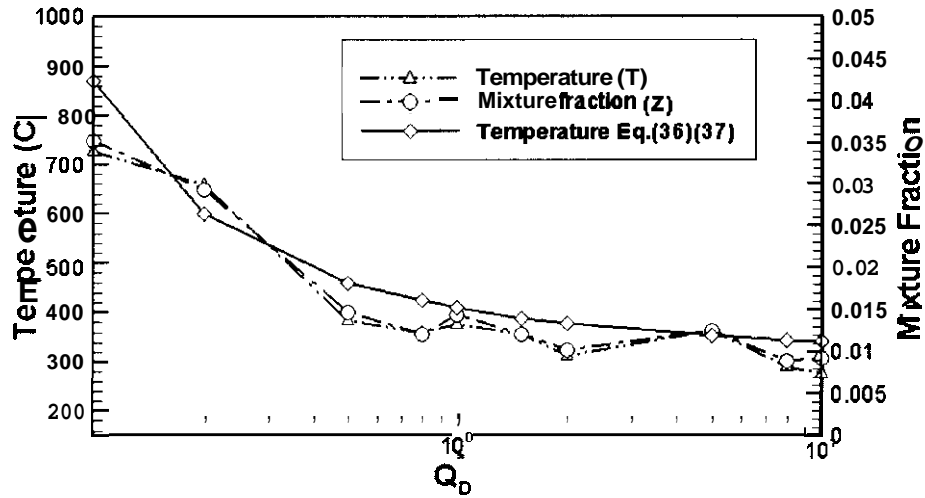


Figure 6. Temperature and Mixture fraction at the flame tip.

As Tamanini ^[44] pointed out, since our combustion model is based on the concept of mixture fraction, the temperature and the mixture fraction share the same governing equation. When using a constant radiative loss fraction, the temperature and the mixture fraction are linearly related, so these two lines should converge into one line, or parallel to each other. Figure 6 shows this trend. As mixture fraction level is an indication of the mixing level, it is also deduced that the mixture fraction level at flame tip is 0.013, which is about one sixth of its stoichiometric value. This shows that the flame entrains about 6 times stoichiometric air to the flame tip.

Currently there are no direct data available on temperature measurement at the flame tip. But using McCaffrey's well-accepted temperature distribution ^[13] and Heskestad's simple flame height correlation ^[14], we can deduce an empirical value of temperature at the flame tip. McCaffrey's correlation for temperature has the form,

$$\frac{2g\Delta T}{T_{\infty}} = \left(\frac{k}{C}\right)^2 \left(\frac{z_f}{Q^{2/5}}\right)^{2n-1} \quad (36)$$

Here the flame tip should be somewhere in the intermittent region. The according constants for intermittent region are, $k=1.9$, $C=0.9$, and $n=0$. The flame height using Heskestad's correlation, which is very simple in form:

$$z_f = 0.235\dot{Q} - 1.020 \quad (37)$$

The solid line in Figure 6 shows the temperature prediction from equation (36) and (37).

4.3. Buoyant Froude Number

Figure 7 shows the computational results for the averaged centerline Froude number. The Froude number, after the flow develops away from the burner surface, ranges from 2 for a very small fire to 1.1 for a very large fire. For fire intensity \dot{Q}_D^* from 0.2 to 1.0, which covers McCaffrey ^[4] experimental range, the Froude number lies within the range of 1.5 to 1.8, while McCaffrey got 1.62. This value is virtually

invariant throughout the fire plume region, from the intermittent zone right down through the continuous flames at the base of the burner.

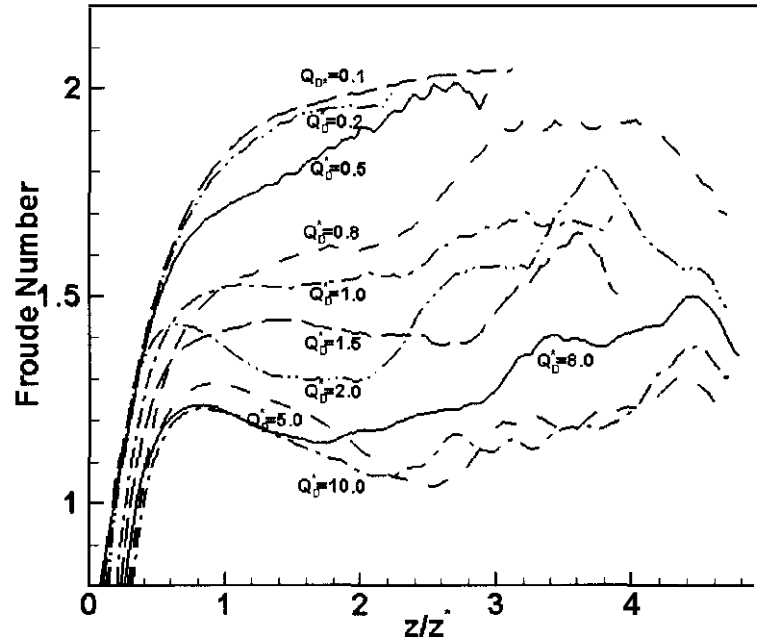


Figure 7. Centerline Froude number

For low Q_D^* fires, the reaction zone is very small, the flow is less turbulent and perhaps inviscid and, i.e., Froude number is close to 2.0. For fires of large Q_D^* , the flame is more jet-like. The computed results are in the range of experimental results, i.e. $Fr = 1.5 \pm 0.1$, and show a systematic effect of Q_D^* which appears related to viscous effects.

4.4. McCaffrey's Experiment

McCaffrey^[4] did a series of classical experiments in 1979. He used natural gas at varied controlled rates on a 0.3 m square burner. His experimental data is used widely to test combustion models. Here we directly compare the simulation result with his experiments. His Q_D^* is 0.3 for this fire.

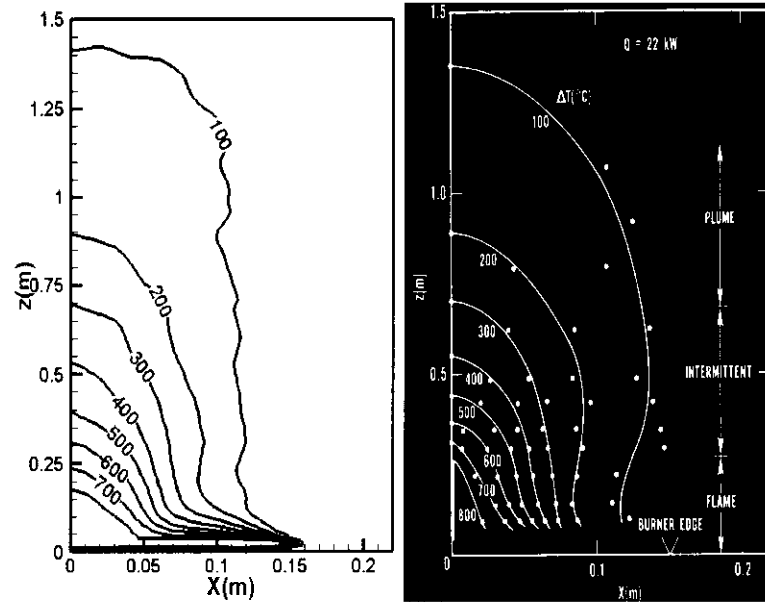


Figure 8. Temperature simulation (left) with McCaffrey's 22 kW fire (right)^[4]

From Figure 8, it is apparent that the vertical temperature distribution is fairly good, while the flame is slightly thinner than the real measurement. A caution should be made here that the temperature in McCaffrey's experiment is acquired without correction of thermocouple data. So the numerical simulation is still low for this fire size (approx. $Q_D^*=0.3$). The centerline temperature distribution shows this trend.

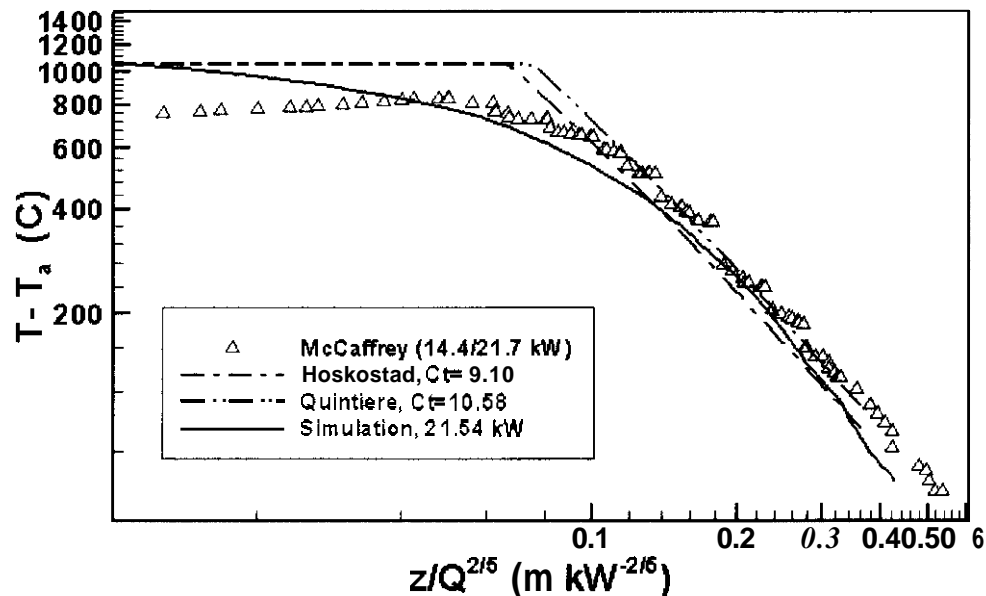


Figure 9. Centerline temperature distribution with McCaffrey's 22 kW fire^[4]

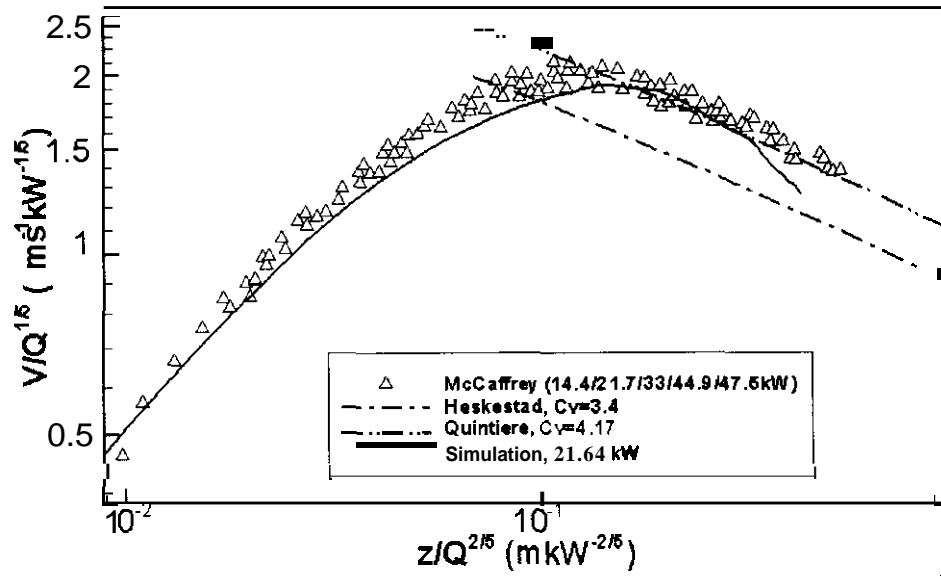


Figure 10. Centerline velocity distribution with McCaffrey's 22 kW fire ^[4]

Deep in flames, the mean temperature reaches approximately 900 °C. Values of mean temp as high as 1000 °C have been observed by Gregory ^[40] in large 9x18m² pool fires. Also Smith et al ^[33] recorded a peak mean temperature of 1260 °C for 17.9 kW natural gas flame. The simulated temperature fits well in the plume region, while over-predicted in the flaming region. The velocity from McCaffrey's experiment contracted together into one curve, our simulation fits well with the measurement data.

4.5. Temperature Distribution

Figure 11 shows the temperature distribution along the centerline for a range of fire size. It shows that the simulated temperature distribution follows the correlation well in plume region. But the temperature rise in the combusting region is still a little high, and the temperature drops earlier than expected in the plume region. For the temperature near the burner surface, the unexpected low values for large fires and the high values for small fires come from the main assumption that the combustion is assumed to be infinitely fast reaction, so most reaction happens close to a flame sheet. The location of the flame sheet determines the flame structure and all other global parameters.

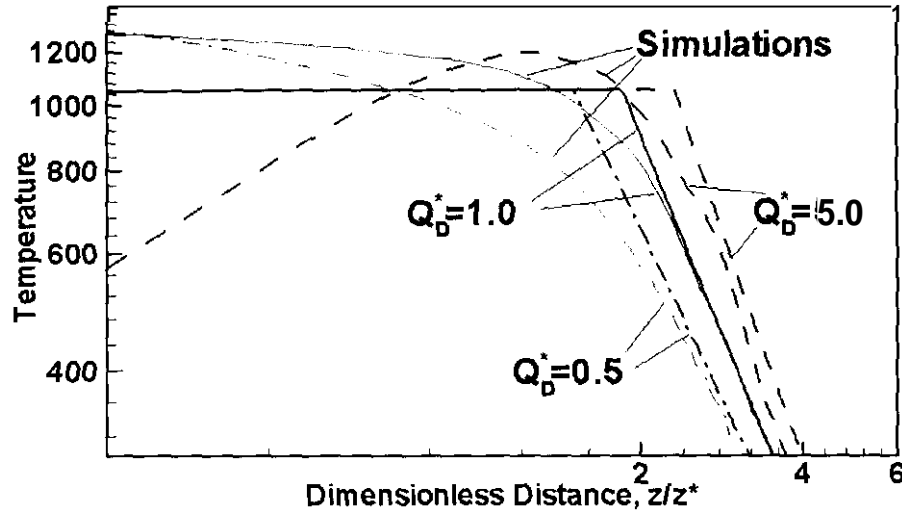


Figure 11. Centerline temperature distribution with Heskestad's correlation, equation (20)(21)(23).

We do not have good temperature data in the flame over a wide range of Q_D^* . The correlation of Eq. (23) is approximate. Here from Table 2 and Figure 5, it can be shown that there are more grid cells over the burner diameter for $Q_D^*=0.5$, while the same number of grid cells is over the flame height. It is not clear why the simulation gives such a unusual effect in the combustion region, but good results in the far-plume region. It is due in part to a high fuel (cool) flow rate for high Q_D^* that lowers the flame temperature near the burner.

4.6. Entrainment Number

As pointed out by Delichatsios^[9], the entrainment number n , the entrained air to stoichiometric air required ratio at the flame tip, is important in determining the flame height. Due to the complexity of entrainment measurements and its variations in theoretical development, this number is found to have many values. Here we check the entrainment behavior of the flame height cases and find the computed entrainment behavior at different levels (shown in Figure 12). The entrainment numbers at flame tip are shown in Figure 13, where the stoichiometric air to fuel mass ratio for propane is found to be 17.3.

EVALUATION STUDIES OF THE FLAME SPREAD AND BURNING RATE PREDICTIONS BY THE FIRE DYNAMICS SIMULATOR

M. Liang

Evaluation Studies of the Flame Spread and Burning Rate Predictions
by the Fire Dynamics Simulator

by

Ming Liang

Thesis submitted to the Faculty of the Graduate School of the
University of Maryland, College Park in partial fulfillment
of the requirements for the degree of
Master of Science
2002

Advisory Committee:

Professor James G. Quintiere, Chair
Professor Frederick W. Mowrer
Professor Andre Marshall

ABSTRACT

Title of Thesis: Evaluation Studies of the Flame Spread and Burning Rate
Predictions by the Fire Dynamics Simulator

Degree candidate: Ming Liang

Degree and year: Master of Science in Fire Protection Engineering, 2002

Thesis directed by: Professor James G. Quintiere
Department of Fire Protection Engineering

Flame spread and burning rate is examined in a 5-m high PMMA vertical slab, using the Fire Dynamics Simulator (FDS), a Computational Fluid Dynamics model. Coupled descriptions of the controlling mechanisms of hydrodynamics model for buoyancy-driven flow, mixture-fraction model for combustion, convection model, banded gray-gases transportation model for radiation, 1-dimensional conduction model for pyrolysis and burning rate model are included. The approaches for pyrolysis and burning rate model are evaluated in a sub-model level, and the refined algorithms are presented.

The models are first tested on a non-spread case to examine the accuracy of prediction for heat **flux** and gas temperature. Results were validated with the literature and the radiation sub-model is tested with various parameters.

Further predictions are made on a more complex large-scale flame spread case involving a PMMA wall, 5 m tall and **0.6** m wide, with perpendicular steel draft containing the flame sheets. Predictions on heat flux, gas and solid temperature, flame spread, and mass burning rate are evaluated.

Generally, good agreement for flame spread and energy release rate is achieved with experiments at levels of spatial resolution that are compatible with the computational demands of field model predictions in compartment fire scenarios.

ACKNOWLEDGEMENTS

Firstly, I would like to thank my advisor, Professor Jim Quintiere, for his continuous motivation, patient guidance and sparkling ideas. I am grateful to Dr. Fred Mowrer and Dr. Andre Marshall for serving in my review committee. A special thanks is extended to the faculty and staff of the Department of Fire Protection Engineering at the University of Maryland. Specifically, I would like to thank Dr. Milke, Dr. di Marzo and Dr. Trouve for instruction along the way. I cannot thank Cindy Gilbert, Allison Spurrier and Sylvia Keane enough for the help and support provided. There are many others whose friendship and support have been important to me during the past 2 years. A partial list follows: Tingguang, Alwin, Boonmee, Kauro, Ali, Clarence, Johnny, Yao... Thank you very much! It is truly an honor to have received an education from the Department.

This project would not have been possible without the financial support of the National Institute of Standards and Technology monitored by Dr. Thomas Ohlemiller. In particular, I would like to thank Dr. Thomas Ohlemiller and Dr. Kevin McGrattan of NIST for their infinite patience and invaluable advice while working on this project.

Finally, words alone cannot express the thanks I owe to my wife, Helen, for her endless love, encouragement and assistance.

TABLE OF CONTENTS

<u>LIST OF FIGURES</u>	v
<u>LIST OF TABLES</u>	vii
<u>NOMENCLATURE</u>	viii
<u>1 INTRODUCTION</u>	1
<u>1.1 Motivation</u>	1
<u>1.2 Background</u>	6
<u>1.3 Approaches and Objectives</u>	8
<u>2 FIRE DYNAMICS SIMULATOR</u>	10
<u>2.1 General and Hydrodynamics Model</u>	10
<u>2.2 Diffusive Terms (LES)</u>	11
<u>2.3 Combustion Models</u>	13
<u>2.4 Convective Heat Transfer to Walls</u>	18
<u>2.5 Radiative Heat Transfer to Walls</u>	18
<u>2.6 Pyrolysis Model – Thermally Thick Solid</u>	21
<u>2.7 Proposed Algorithm for Surface Temperature of Thermally-thick Material</u>	23
<u>2.8 Proposed Algorithm for Burning Rate of Thermally Thick Material</u>	24
<u>3 BACK’S WALL FIRE TESTS</u>	30
<u>3.1 Description of the Wall Fire Experiment</u>	30
<u>3.2 Back’s Experimental Results</u>	31
<u>4 EVALUATION OF THE FDS-PREDICTION ON BACK’S WALL TEST</u>	34
<u>4.1 FDS Input</u>	34

4.2	<u>FDS Predictions on the Centerline Temperature</u>	35
4.3	<u>FDS Predictions on the Wall Heat Flux Distribution</u>	36
4.4	<u>FDS Predictions on the Flame Height</u>	38
4.5	<u>Summary of the FDS Predictions on Beck's Wall Fire Tests</u>	39
5	<u>FM'S LARGE-SCALE PMMA WALL FIRE TEST.....</u>	40
5.1	<u>FMRC 500-kW-Scale Flammability Apparatus and the Experimental Setup</u>	40
5.2	<u>A Close Look at PMMA's Thermal Properties</u>	44
5.3	<u>FMRC Experimental Results</u>	49
6	<u>EVALUATION OF THE FDS PREDICTION ON THE PMMA WALL TEST...</u>	51
6.1	<u>FDS Implementation Issues</u>	51
6.2	<u>Comparison of the Heat Release Rate History</u>	54
6.3	<u>Comparison of the Flame Spread</u>	55
6.4	<u>Comparison of the Total Heat Flux</u>	57
6.5	<u>Comparison of the Burning Rate</u>	58
7	<u>EVALUATION OF THE FDS PREDICTION ON THE SMALL-SCALE PMMA WALL TEST.....</u>	61
7.1	<u>Small-scale Flame Spread Experimental Setup</u>	61
7.2	<u>SOFI-2 and FDS Calculations</u>	61
7.3	<u>The PMMA Thermal Properties</u>	62
7.4	<u>Comparison of the Results</u>	65
8	<u>SUMMARY AND CONCLUSIONS.....</u>	71
9	<u>REFERENCES.....</u>	77

LIST OF FIGURES

Figure 1	<u>Relationship of mixture fraction and species concentration for burning PMMA</u>	16
Figure 2	<u>Heat & Mass Transfer Processes for a Thermally Thick Material</u>	26
Figure 3	<u>Experimental Setup for Beck's Wall Fire</u>	31
Figure 4	<u>Measured centerline heat flux</u>	33
Figure 5	<u>FDS Simulation Domain for Beck's Wall Fire Test</u>	34
Figure 6	<u>Centerline Gas Temperature (1.25 cm against wall) All Tests</u>	36
Figure 7	<u>Heat Flux Distribution</u>	37
Figure 8	<u>Heat Flux Distribution for Test 6</u>	38
Figure 9	<u>Flame Height</u>	39
Figure 10	<u>Full Scale PMMA Wall Fire Test</u>	41
Figure 11	<u>FMRC 50-kW Flammability Apparatus as shown. The 500-kW apparatus is similar except for size</u>	42
Figure 12	<u>PMMA</u>	45
Figure 13	<u>Heat Capacity of various solid and molten PMMA</u>	46
Figure 14	<u>Thermal Conductivity of Various Solid and Molten PMMA</u>	47
Figure 15	<u>Thermocouple Reading on the Surface of the Samples at the onset of pyrolysis</u>	48
Figure 16	<u>Total Heat Flux Distribution at Various Time</u>	49
Figure 17	<u>Pyrolysis Height History</u>	50
Figure 18	<u>Heat Release Rate History</u>	50

Figure 19	Input File for FDS Simulation of the FM Wall Fire Test.....	53
Figure 20	Comparison of HRR History, After Synchronized (34 kW)	54
Figure 21	Comparison of Flame Spread.....	56
Figure 22	PMMA Surface Temperature Calculated by FDS	56
Figure 23	Comparison of Total Heat Flux Distribution at Various Times	57
Figure 24	Comparison of Mass Burning Rate	60
Figure 25	Comparison Of k	64
Figure 26	Comparison Of α	64
Figure 27	Heat Release Rate Given By FDS Calculation For The Small-Scale Test..	65
Figure 28	Cross Comparison For Heat Release Rate Given By FDS Calculation For The Large- And Small-Scale Tests	66
Figure 29	Cross Comparison Between Predicted Flame Spread Velocity By SOFIE And FDS And Experimental Measurements By Orloff	67
Figure 30	FDS-Calculated Surface Temperature Vs. Height, Varied By Time	68
Figure 31	Incident Convective Heat Flux Comparison.....	69
Figure 32	Incident Radiative Heat Flux Comparison Between Predictions And The Experimental Values	70
Figure 33	Numerical Solution of Equation 83.....	75

LIST OF TABLES

Table 1	Experimental Results and Flame Height	33
Table 2	PMMA Thermal Properties Used in the FDS Simulation	44
Table 3	Air Thermal Properties Used in Ahmad & Faeth's Correlations	59
Table 4	Thermal Properties Used In SOLID And FDS	63

NOMENCLATURE

a	thermal diffusivity (m^2/s)
c_p	constant pressure specific heat capacity (kJ/kg-K)
δ	thickness, thermal penetration depth (m)
D	Diffusion coefficient (m^2/s)
ΔH_c	heat of combustion (kJ/kg)
ΔH_v	heat of vaporization (kJ/kg)
Fr	Froude number (dimensionless)
Gr	Grashof number (dimensionless)
g	gravitational acceleration (m/s^2)
κ	absorption coefficient (%)
k, k_s	thermal conductivity (W/m-K)
\dot{m}_F''	mass burning rate of fuel per unit area, ($\text{kg/m}^2\text{-s}$)
Q	heat release rate of the fire or firepower (kW)
Pr	Prandtl number (dimensionless)
P	pressure (Pa)
\dot{q}''	heat flux (kW/m^2)
ρ	density (g/mL and kg/m^3)
r, χ_r	radiation fraction (%)
Re	Reynolds number (dimensionless)

s	stoichiometric number (dimensionless)
Sc	Schmidt number (dimensionless)
T	temperature (K and °C)
T_p	pyrolysis temperature (K and °C)
t, τ	time (s)
u	velocity (m/s)
ν	viscosity (N-s/m ²)
Y_i	mass fraction (%)
z^*	characteristic length of fire power (m)
Z	mixture fraction (%)

$()_{\infty}, ()^{\infty}$	ambient value
$()^*$	dimensionless quantity
$(\dot{ })$	rate of change
$(\dot{ })''$	rate of change per unit area
$(\dot{ })'''$	rate of change per unit volume
$()_c$	convection heat transfer value
$()_k$	conduction heat transfer value
$()_r$	radiation heat transfer value
$()_{RR}$	re-radiation heat transfer value
$()_F$	fuel value
$()_O$	oxygen value

1 INTRODUCTION

Numerical field modeling of fires, as emerging since the 1980's, has provided an economic and reasonably accurate approach to the assessment of fire hazard. At the National Institute for Standards and Technology (NIST), the Fire Dynamics Simulator (FDS) has been developed based on the fundamental conservation of heat, momentum and mass using a Large Eddy Simulation (LES) method. The effort to develop FDS and all other computer-based models has been paralleled by a continual effort to determine the accuracy of the predictions by comparing the models to laboratory experiments. As a result of various validation studies, the FDS has proved to do well, especially in flow-related aspects, *i.e.* in simulating the smoke movement¹ and smoke plume trajectory¹. Spearpoint et al.³ simulated a fully furnished compartment fire, and discovered unsatisfactory predictions in his flashover scenario of a room fire.

1.1 Motivation

Fire modeling was formally introduced to the fire research and engineering arena in 1960. Along with the introduction of fire modeling, the knowledge of fire dynamics has grown significantly. This knowledge has led to the development of complex fire models that can only be practically implemented by computers. Many of these models are widely used in Fire Protection Engineering to analyze the hazards and risks associated with building fires⁴. Their uses have become widespread in the performance-based-design applications.

Fire simulation computer codes provide a means to evaluate the performance-based design for fire safety under a range of possible fire scenarios. With wide applications in smoke movement, detector/sprinkler activation, fire growth and development, to building structure response, the fire simulation codes are helping the fire protection engineering arena in many aspects.

Jones ⁵ pointed out the need to ensure the validity of fire model applications in a regulated environment. An evaluation process for model validation typically includes the following components ^{6,7}: conceptual validation, model verification, and operational evaluation. Conceptual validation consists of determining the correctness of the assumptions and theoretical basis for a model with respect to its intended purpose. Model verification is the process of determining the correct mathematical implementation of the underlying theory. Operational evaluation is quantifying the accuracy of model results. The first two processes, conceptual validation and model verification, are typically performed during the model's development in hope of resolving any preliminary issues regarding its fundamental validity. The last process, operational evaluation, is critical to establishing the acceptable uses and limitations of the model.

Evaluation is the process of determining the models range of application and consists of comparing model output to reliable data. There is a wide range of possible scenarios for model evaluation. Hence, this process has historically been a post-development endeavor that continues throughout the model's life.

In a recent project, Ma³¹ explored the accuracy and limitations of FDS on axisymmetric fire plumes. They examined the FDS for unconfined fires of different dimensionless heat release rate Q^* . The gridsize plays an important role in deciding the flame structure. As the simulation resolution was defined as the grid size over the characteristic length, they found that the optimum resolution of a pool fire simulation is 0.05. In other words, the characteristic length is defined as

$$z^* = \left(\frac{Q}{\rho_\infty c_p T_\infty \sqrt{g}} \right)^{2/5} = (\dot{Q}_D^*)^{1/5} \cdot D, \text{ and the grid size may be defined as 5\% of } z^* \text{ so as to}$$

obtain accurate results. Their work was fundamental to further work on the flame-spread prediction by FDS.

Lewis, Rubini and Moss⁸ performed a field modeling of flame spread. Using the SOFIE code⁹, a simplified model of non-charring solid pyrolysis has been coupled with detailed descriptions of turbulent combustion, soot production and radiative exchange to create a field model for fire spread prediction. The sensitivity of the predictions to alternative soot models and to the level of resolution employed is demonstrated by comparison with established two-dimensional experiments on **PMMA** slabs reported in the literature by Orloff et al³⁶. The SOFIE Code uses a two-equation k - ϵ turbulence model for modeling of buoyant turbulent flow, while the FDS uses the LES as its turbulence model. It was reported that the level of agreement between measurements of flame spread velocity, mass loss rate and incident heat flux is generally good.

On another recent related research by Wang et al. at the Université de Poitiers ¹⁰, where non-spread vertical wall fire tests with a narrow range of Q^* are examined, it was found out that the FDS-computed, time-averaged flame height, velocity and temperature profiles are relatively in good agreement with the measured value by Orloff ³⁶, but the deviation increases as the height increases. The simulation results in this work match their findings.

Spearpoint et al. ³ investigated the FDS simulation of a fully furnished compartment fire, using an earlier version of FDS, and compared to the zone model Fire MD. The field model compared unsatisfactory with zone model simulation, partly because of inadequacy of the sub-models of radiation and boundary conditions.

Floyd ¹¹ performed simulations comparing model predictions with full-scale nuclear facility fire test data. The code did poorly for situations where the fire is under-ventilated or in the flashover stage. The weaknesses were attributed to the crude radiation and combustion models.

A series of simulations were performed by Friday and Mowrer ⁶ to validate FDS with data from Factory Mutual and Sandia National Laboratories for mechanically ventilated enclosure fires. Functional analysis is performed for comparing results. A grid dependent plume study was performed to investigate the relationship of grid resolution and plume temperature predictions. Increasing the number of grid cells in the plume region does not improve temperature predictions significantly, but does result in more accurate simulation of plume turbulent structures. This laid a solid foundation for our grid-dependent study in the combusting region.

In the newly released version 2.0 of **FDS** debuted on December 4, 2001, the new features mainly consist of substantial improvements in combustion, radiation transport and the boundary conditions¹².

In the new combustion model, a more comprehensive method that handles oxygen consumption more naturally solves an equation for a conserved scalar quantity, known as the mixture fraction, which is defined as the fraction of gas at a given point in the flow field that originated as fuel. The model assumes that combustion is mixing-controlled, and that the reaction of fuel and oxygen is infinitely fast. The mass fractions of **all** of the major reactants and products can be derived from the mixture fraction by means of “state relations,” empirical expressions arrived at by a combination of simplified analysis and measurement.

The **FDS** Version 2 handles radiative heat transfer in a better way, by returning to the fundamental radiation transport equation for a non-scattering gray gas. The equation is solved using a technique similar to finite volume methods for convective transport, thus the name given to it is the Finite Volume Method (FVM). Using approximately 100 discrete angles, the finite volume solver requires about 15 % of the total CPU time of a calculation, a modest cost given the complexity of radiation heat transfer.

For the boundary conditions, the few changes include that the requirement that **all** internal obstructions (like walls) be at least *two* cells thick is gone in **FDS** 2. This is due to a revised method of storing information about solid surfaces. It is transparent to

the user, but does result in less “leakage” of heat and mass through one cell thick obstructions.

However, there are few validations and the subsequent discussion on the ignition and flame spread on FDS predictions, partly because the earlier versions of FDS are more smoke movement and fire plume focused. But with the introduction of the more advanced sub-models as mentioned above, the need for validation and further improvement of the ignition and flame spread prediction is in demand. Much of the work presented here focuses on the ignition and flame spread issues, plus their relationship with the incident heat flux distribution.

1.2 Background

For a computer code simulating a fire scenario with the emphasis on ignition and flame spread, it is most important that models regarding initiation and development of the burning of materials are properly deployed. Ignition and flame spread is a result of the thermal decomposition of the combustibles and the ignition of the resulting gaseous pyrolysis products of the gaseous mixture above the combustible’s surface. It is a complex phenomenon that involves chemical and physical processes in both gas and solid phases. The combustible’s thermal properties and the environmental variables are the two main groups of factors controlling the ignition and flame spread process. The thermal properties usually include thermal inertia ($k\rho c$), thermal diffusivity (a), density (ρ) or surface density ($\rho\delta$), heat of combustion (ΔH_c), heat of vaporization (ΔH_v) and pyrolysis temperature (T_p) etc. The environmental properties generally include incident

heat fluxes, geometry factors, flame versus gas-flow orientation etc. While the incident heat fluxes consist of radiation, convection and conduction heat flux, thus further making the scenario a more complex one. Quintiere¹³ provides a very good description of this.

Natural fires typically involve diffusion flames spreading over the surface of solid combustibles. The spread of the flames results from the complex interaction of transport and chemical processes that occur in the vicinity of the boundary separating the burning and non-burning regions. For a flame to spread over the surface of a combustible material, sufficient heat must be transferred from the burning region of the fuel to the unburnt material to cause the fuel to pyrolyze. This is a primary condition that must be met for the flames to spread. Once the fuel pyrolyzes, propagation can proceed. The gas phase reaction of fuel vapor and oxidizer introduces two central controlling mechanisms – heat transfer to the unburnt fuel and gas phase chemical reaction – are often separately identifiable.¹⁴

In the fire science arena, the flame spread phenomena is broken down into two stages in a time sequence: ignition and flame spread. However, the controlling mechanism mentioned above defines whether the flame is self-sustainable and can propagate.

The gas phase ignition from a solid combustible is started by heating up the solid by an incident heat flux, which can be a heat flux from the flame or an external source independent from the solid combustible in question. The combustible surface is heated up and raised to the pyrolysis temperature (T_p). After attaining T_p , the pyrolyzed

vapor leaves the surface, is diffused and convected outwards, mixes with the oxygen, creating a flammable mixture near the solid surface. Flaming ignition will occur, if the mixture temperature is increased so that the energy from the chemical reaction is self-sustained.

Once the fuel is ignited, the flame propagates across the surface, establishing a diffusion flame on it. The flame transfers heat to the surface and more fuel is vaporized, providing the necessary gaseous fuel to sustain the flame. Three independent heat sources lead to the spread of a flame: gas phase heat convection, solid conduction, and external heat contribution. Despite the heat sources, there are other phenomena which can play an important role in flame spread, such as air flow which can aid or delay the flame spread.

Many of these phenomena have been considered and some of the well-developed theoretical models have been implemented into the development of FDS, especially Version 2.

1.3 Approaches and Objectives

In this work, an assessment is conducted for the ability of the FDS model to predict heat flux to a vertical wall from a floor burner²⁹. Furthermore, FDS prediction of flame spread on PMMA is examined by using data from Factory Mutual³³ as the benchmark.

A static case of no spread but with **PMMA** burning is also investigated. It is to validate the dynamic results provided by FDS with the steady state case and to the

correlations developed by Ahmad and Faeth ¹⁵ for wall fire heat flux and mass burning flux.

In examining flame spread, it is attempted to develop a simpler model for determining the surface temperature and mass flux that would avoid a detailed computation of wall conduction.

2 FIRE DYNAMICS SIMULATOR

The purpose of this chapter is to provide a description of the fundamentals for the FDS models involving ignition and flame spread.

2.1 General and Hydrodynamics Model

The idea of numerically simulating a fire scenario has emerged and been continuously developed by scientists and engineers. Indeed, the fundamental conservation equations governing fluid dynamics, heat transfer, and combustion were first written down over a century ago. Despite this, practical mathematical models of fire (as distinct from controlled combustion) are relatively recent due to the inherent complexity of the problem. The governing equations are:

Conservation of Mass:

$$\frac{\partial \rho}{\partial t} + \nabla \cdot \rho \mathbf{u} = 0 \quad \text{Equation 1}$$

$$\text{or: } \frac{D\rho}{Dt} + \rho(\nabla \cdot \mathbf{u}) = 0 \quad \text{Equation 2}$$

Conservation of Species:

$$\frac{\partial \rho Y_i}{\partial t} + \nabla \cdot \rho Y_i \mathbf{u} = \nabla \cdot \rho D_i \nabla Y_i + \dot{W}^m \quad \text{Equation 3}$$

Conservation of Momentum:

$$\frac{\partial (\rho \mathbf{u})}{\partial t} + \nabla \cdot \rho \mathbf{u} \mathbf{u} = -\nabla p + \rho \mathbf{g} + \nabla \cdot \boldsymbol{\tau} \quad \text{Equation 4}$$

$$\text{or: } \rho \frac{D\mathbf{u}}{Dt} = -\nabla p + \rho \mathbf{g} + \nabla \cdot \boldsymbol{\tau} \quad \text{Equation 5}$$

Conservation of Energy:

$$\frac{\partial(\rho h)}{\partial t} + \nabla \cdot \rho h \mathbf{u} = \frac{Dp}{Dt} + \dot{q}''' + \nabla \cdot k \nabla T \quad \text{Equation 6}$$

Equation of State:

$$p = \Re \rho T \quad \text{Equation 7}$$

When rewriting the above equations, note that for a given scalar quantity $\phi_{(x,y,z,t)}$, because of the mass conservation equation, it is often convenient to write the transport equations between these two forms:

$$\frac{\partial \rho \phi}{\partial t} + \nabla \cdot \rho \mathbf{u} \phi = \rho \frac{D\phi}{Dt} \quad \text{Equation 8}$$

While dealing with the governing equations, these unknown parameters are solved so that people can predict a fire scenario. These to-be-solved unknowns are: density, ρ ; velocity, \mathbf{u} ; enthalpy, h and pressure, p . To do this, the following parameters must be provided: the firepower per unit volume, \dot{q}''' ; the turbulent viscous stress, $\boldsymbol{\tau}$; and the thermal conductivity term, $\nabla \cdot k \nabla T$.

2.2 Diffusive Terms (LES)

The viscous stress tensor in the momentum equation is given by:

$$\boldsymbol{\tau} = \mu \left(2 \text{def } \mathbf{u} - \frac{2}{3} (\nabla \cdot \mathbf{u}) \mathbf{I} \right) \quad \text{Equation 9}$$

where \mathbf{I} is the identity matrix and the deformation tensor is defined as:

$$\text{def } \mathbf{u} = \frac{1}{2} [\nabla \mathbf{u} + (\nabla \mathbf{u})^T] = \begin{pmatrix} \frac{\partial u}{\partial x} & \frac{1}{2} \left(\frac{\partial u}{\partial y} + \frac{\partial v}{\partial x} \right) & \frac{1}{2} \left(\frac{\partial u}{\partial z} + \frac{\partial w}{\partial x} \right) \\ \frac{1}{2} \left(\frac{\partial v}{\partial x} + \frac{\partial u}{\partial y} \right) & \frac{\partial v}{\partial y} & \frac{1}{2} \left(\frac{\partial v}{\partial z} + \frac{\partial w}{\partial y} \right) \\ \frac{1}{2} \left(\frac{\partial w}{\partial x} + \frac{\partial u}{\partial z} \right) & \frac{1}{2} \left(\frac{\partial w}{\partial y} + \frac{\partial v}{\partial z} \right) & \frac{\partial w}{\partial z} \end{pmatrix} \quad \text{Equation 10}$$

In the numerical model, there are two options for treating the dynamic viscosity μ . For a Large Eddy Simulation (LES) where the grid resolution is not fine enough to capture the mixing processes at all relevant scales, a sub-grid scale model for the viscosity is applied. Following the analysis of Smagorinsky¹⁶, the viscosity can be modeled as:

$$\mu_{\text{LES}} = \rho (C_s \Delta)^2 \left(2(\text{def } \mathbf{u}) \cdot (\text{def } \mathbf{u}) - \frac{2}{3} (\nabla \cdot \mathbf{u})^2 \right)^{\frac{1}{2}} \quad \text{Equation 11}$$

where C_s is an empirical constant value, Δ is a length on the order of the size of a grid cell, and the deformation term is related to the Dissipation Function:

$$\begin{aligned} \Phi = \boldsymbol{\tau} \cdot \nabla \mathbf{u} &= \mu \left(2(\text{def } \mathbf{u}) \cdot (\text{def } \mathbf{u}) - \frac{2}{3} (\nabla \cdot \mathbf{u})^2 \right) \\ &= \mu \left[2 \left(\frac{\partial u}{\partial x} \right)^2 + 2 \left(\frac{\partial v}{\partial y} \right)^2 + 2 \left(\frac{\partial w}{\partial z} \right)^2 + \left(\frac{\partial v}{\partial x} + \frac{\partial u}{\partial y} \right)^2 + \right. \\ &\quad \left. \left(\frac{\partial w}{\partial y} + \frac{\partial v}{\partial z} \right)^2 + \left(\frac{\partial u}{\partial z} + \frac{\partial w}{\partial x} \right)^2 - \frac{2}{3} \left(\frac{\partial u}{\partial x} + \frac{\partial v}{\partial y} + \frac{\partial w}{\partial z} \right)^2 \right] \end{aligned} \quad \text{Equation 12}$$

The dissipation function is the rate at which kinetic energy is transferred to thermal energy. It is a source term in the energy conservation equation that is usually

neglected because it is small – an approximation consistent with the low Mach number equations.

In an LES calculation, the thermal conductivity and material diffusivity are related to the turbulent viscosity by

$$k_{\text{LES}} = \frac{\mu_{\text{LES}} C_p}{\text{Pr}} \quad ; \quad (\rho D)_{\text{LES}} = \frac{\mu_{\text{LES}}}{\text{Sc}} \quad \text{Equation 13}$$

The Prandtl number, Pr, and the Schmidt number, Sc, are assumed constants for a given scenario. There have been numerous refinements of the original Smagorinsky model^{17,18,19}, but it is difficult to assess the improvements offered by these newer schemes. There are two reasons for this. First, the structure of the fire plume is so dominated by the large-scale resolvable eddies that even a constant eddy viscosity gives results almost identical to those obtained using the Smagorinsky model²⁰. Second, the lack of precision in most large-scale fire test data makes it difficult to assess the relative accuracy of each model. The Smagorinsky model with the empirical fixed value C_s produces satisfactory results for most large-scale applications where boundary layers are not well resolved.

2.3 Combustion Models

There are two types of combustion models used in FDS. The choice depends on the resolution of the underlying grid. For a DNS calculation where the diffusion of fuel and oxygen can be modeled directly, a global one-step, finite-rate chemical reaction is most appropriate. However, in an LES calculation where the grid is not fine enough to

resolve the diffusion of fuel and oxygen, a mixture fraction-based combustion model is used. In this work, the simulations are done by the Mixture Fraction model.

The mixture fraction combustion model is based on the assumption that large-scale convective and radiative transport phenomena can be simulated directly, but physical processes occurring at small length and time scales must be represented in an approximate manner. The nature of the approximations employed is necessarily a function of the spatial and temporal resolution limits of the computation, as well as the current, often limited, understanding of the phenomena involved. The actual chemical rate processes that control the combustion energy release are often unknown in tire scenarios. Even if they were known, the spatial and temporal resolution limits imposed by both present and foreseeable computer resources places a detailed description of combustion processes beyond reach. Thus, the mixture fraction model is based on the assumption that the combustion is mixing-controlled. This implies that all species of interest can be described in terms of a mixture fraction $Z(\mathbf{x}; t)$. The mixture fraction is a conserved quantity representing the fraction of material at a given point that originated as fuel. The relations between the mass fraction of each species and the mixture fraction are known as “state relations.” The state relation for the oxygen mass fraction provides the information needed to calculate the local oxygen mass consumption rate. The form of the state relation that emerges from classical laminar diffusion flame theory is a piecewise linear function. This leads to a “flame sheet” model, where the flame is a two dimensional surface embedded in a three dimensional space. The local heat release rate is computed from the local oxygen consumption rate at the flame surface, assuming that

the heat release rate is directly proportional to the oxygen consumption rate, which is an input but with the default as propane, although the heat release rate per unit mass of oxygen, ΔH_O , does not change much with different types of fuels.

In the FDS simulations, the combustion heat release is assumed to be mixing controlled. The fuel selected for model validation is PMMA, reflecting the wealth of experimental data available for comparison between prediction and experiment. PMMA is assumed to thermally pyrolyse to the simple monomer $C_5H_8O_2$ and, at its simplest, chemical reaction then proceeds with the single step:



The mixture fraction Z is defined as:

$$Z \equiv \frac{sY_F - (Y_O - Y_O^\infty)}{sY_F^\infty + Y_O^\infty} \quad \text{Equation 15}$$

while $Z=1$ in the fuel stream and $Z=0$ for pure air, with $Y_O = Y_O^\infty \approx 0.23$, and for PMMA

$$\text{monomer, } s = \frac{\nu_O M_O}{\nu_F M_F} = \frac{(6)(32)}{(1)(100)} = 1.92$$

Recalling the equations of specie conservation for oxygen and fuel, and using the following transformations,

$$\frac{s}{sY_F^\infty + Y_O^\infty} \times \left[\rho \frac{DY_F}{Dt} = \nabla \cdot \rho D \nabla Y_F + \dot{W}_F''' \right] \quad \text{Equation 16}$$

$$\frac{-1}{sY_F^\infty + Y_O^\infty} \times \left[\rho \frac{D(Y_O - Y_O^\infty)}{Dt} = \nabla \cdot \rho D \nabla (Y_O - Y_O^\infty) + \dot{W}_O''' \right] \quad \text{Equation 17}$$

and summing up the above two equations, yielding:

$$\rho \frac{DZ}{Dt} = \nabla \cdot \rho D \nabla Z \quad \text{Equation 18}$$

The assumption that the chemistry is “fast” means that the reactions that consume fuel and oxidizer occur so rapidly that the fuel and oxidizer cannot co-exist. The requirement that fuel and oxidizer simultaneously vanish defines a flame surface as: (where Z_f here is the location of “flame sheet” or stoichiometric reaction)

$$Z(\mathbf{x}, t) = Z_f \quad \text{and} \quad Z = \frac{Y_f^\infty}{sY_F^\infty + Y_O^\infty} \quad \text{Equation 19}$$

The assumption that fuel and oxidizer cannot co-exist leads to the “state relation” between the oxygen mass fraction Y_O and mixture fraction Z ,

$$Y_O(Z) = \begin{cases} Y_O^\infty (1 - Z/Z_f) & Z < Z_f \\ 0 & Z > Z_f \end{cases} \quad \text{Equation 20}$$

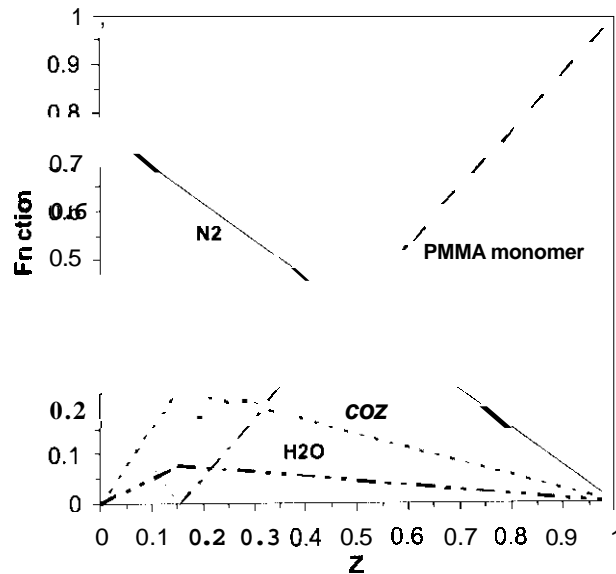


Figure 1 –Relationship of mixture fraction and species concentration for
burning **PMMA**

The oxygen mass conservation equation can be transformed into an expression for the local heat release rate using the conservation equation for the mixture fraction and the state relation for oxygen $Y_o(Z)$:

$$\rho \frac{DY_o}{Dt} = P \frac{dY_o}{dZ} \frac{DZ}{Dt} = \frac{dY_o}{dZ} \nabla \cdot \rho D \nabla Z \quad ; \quad \rho D \nabla Y_o = \rho D \frac{dY_o}{dZ} \nabla Z \quad \text{Equation 21}$$

Yielding:

$$-\dot{m}_o''' = \nabla \cdot \left(\rho D \frac{dY_o}{dZ} \nabla Z \right) - \frac{dY_o}{dZ} \nabla \cdot \rho D \nabla Z \quad \text{Equation 22}$$

The main purpose of mixture fraction model is to obtain the heat release rate per unit volume, \dot{q}''' , which is based on the consumption of oxygen, \dot{m}_o''' :

$$\dot{q}''' = \Delta H_o \cdot \dot{m}_o''' \quad \text{Equation 23}$$

The mixture fraction model has provided the basis for the combustion model by solving only one additional scalar diffusion equation, and the infinite rate of combustion is consistent with LES length and time scales. Furthermore, all the product species can be expressed as a function of mixture fraction.

However, the assumptions of mixture fraction model also bring some limitations. Firstly, the diffusion coefficient, D , has to be same for all gas species. Secondly, the chemical kinetics is simplified to one step reaction with infinite reaction rate. Thirdly, fuel and oxygen are always reacted eventually, regardless of temperature, thus limiting the usage of this model to certain scenarios – such as the ventilation-controlled cases. In these cases, due to low temperature and reduced oxygen

concentration, the oxygen and fuel does not react as predicted by the Mixture Fraction Model.

2.4 Convective Heat Transfer to Walls

The heat flux to a solid surface consists of the summation of gains and losses due to convection and radiation. In an LES calculation, the convective heat flux to the surface is obtained from a combination of correlations for natural and forced convection:

$$\dot{q}_c'' = h \cdot \Delta T \quad \text{Equation 24}$$

$$h = \max \left[C |\Delta T|^{\frac{1}{3}}, 0.037 \frac{k}{L} \left(\frac{L}{\nu} \right)^{\frac{1}{3}} \Pr^{\frac{1}{3}} \right] \quad \text{Equation 25}$$

where ΔT is the difference between the wall and the gas temperature, C is the coefficient for natural convection (1.43 for a horizontal surface and 0.95 for a vertical surface)²¹, L is a characteristic distance related to the size of the plate, k is the thermal conductivity of the gas, and ν is the kinetic viscosity of the gas.

2.5 Radiative Heat Transfer to Walls

The Radiative Transport Equation (RTE) for a non-scattering gray gas is:

$$\mathbf{s} \cdot \nabla I_{\lambda}(\mathbf{x}, \mathbf{s}) = \kappa(\mathbf{x}, \lambda) [I_b(\mathbf{x}, \lambda) - I(\mathbf{x}, \mathbf{s})] \quad \text{Equation 26}$$

where $I_\lambda(\mathbf{x}, \mathbf{s})$ is the radiant intensity at wave length λ , $I_b(\mathbf{x}, \mathbf{s})$ is the source term given by the Planck function, \mathbf{s} is the unit normal direction vector and $\kappa(\mathbf{x})$ is the gray-gas absorption coefficient. In practical simulations, the spectral dependence cannot be solved accurately. Instead, the radiation spectrum is divided into a relatively small number, n , of bands, and a separate RTE is derived for each band.

$$\mathbf{s} \cdot \nabla I_n(\mathbf{x}, \mathbf{s}) = \kappa_n(\mathbf{x}) [I_{b,n}(\mathbf{x}, \mathbf{s}) - I_n(\mathbf{x}, \mathbf{s})] \quad n = 1 \dots N \quad \text{Equation 27}$$

The limits of the bands are selected to give an accurate representation of the most important radiation bands of CO₂ and water. When the intensities corresponding to the bands are known, the total intensity is calculated by summing over all the bands:

$$I(\mathbf{x}, \mathbf{s}) = \sum_{n=1}^N I_n(\mathbf{x}, \mathbf{s}) \quad \text{Equation 28}$$

Even with a reasonably small number of bands, the solution of N RTE's is very time consuming. Fortunately, in most large-scale fire scenarios soot is the most important combustion product controlling the thermal radiation from the fire and hot smoke. As the radiation spectrum of soot is continuous, it is possible to assume that the gas behaves as a gray medium. The spectral dependence is lumped into one absorption coefficient ($N = 1$) and the source term is given by the blackbody radiation intensity:

$$I_b(\mathbf{x}) = \frac{\sigma T(\mathbf{x})^4}{\pi} \quad \text{Equation 29}$$

In optically thin flames, where the amount of soot is small compared to the amount of CO₂ and water, the gray gas assumption may produce significant over-predictions of the emitted radiation^{**}. For the calculation of the gray or band-mean

absorption coefficients, κ_n , a narrow-band model, RADCAL²³, has been implemented in FDS. At the start of a simulation, the absorption coefficients are tabulated as a function of mixture fraction and temperature. During the simulation, the local absorption coefficient is found by table-lookup. In calculations of limited spatial resolution, the source term, I_b , in the RTE requires special treatment in the neighborhood of the flame sheet because the temperature values are smeared out over a grid cell and are thus considerably lower than one would expect in a diffusion flame. Because of its dependence on the temperature raised to the fourth power, the source term must be modeled in those grid cells cut by the flame sheet. Elsewhere, there is greater confidence in the computed temperature, and the source term can assume its ideal value there:

$$\kappa I_b = \begin{cases} \frac{\kappa \sigma T^4}{\pi} & \text{Outside flame zone} \\ \frac{\chi_r \dot{q}'''}{4\pi} & \text{Inside flame zone} \end{cases} \quad \text{Equation 30}$$

Here, \dot{q}''' is the chemical heat release rate per unit volume and χ_r is the *local* fraction of that energy emitted as thermal radiation. There is a difference between the prescriptions of a local χ_r and its resulting global equivalent. For a fire with $D < 1$ m, the local χ_r is approximately equal to its global counterpart. However, as the fire increases in size, the global value will typically decrease due to a net re-absorption of the thermal radiation by the increasing smoke mantle.

The boundary condition for the radiation intensity leaving a gray diffuse wall is given as the following, and the radiative heat flux at the surface is obtained from the boundary condition,

$$I_w(\mathbf{s}) = \varepsilon I_{bw} + \left(\frac{1 - \varepsilon}{\pi} \right) \int_{\mathbf{s}' \cdot \mathbf{n}_w < 0} I_w(\mathbf{s}') |\mathbf{s}' \cdot \mathbf{n}_w| d\Omega \quad \text{Equation 31}$$

where $I_w(\mathbf{s})$ is the intensity at the wall, ε is the emissivity of the wall, and I_{bw} is the black body intensity at the wall.

The radiant heat **flux** vector \mathbf{q}_r is defined as:

$$\mathbf{q}_r(\mathbf{x}) = \int \mathbf{s} I(\mathbf{x}, \mathbf{s}) d\Omega \quad \text{Equation 32}$$

The radiative loss term in the energy equation is

$$-\mathbf{V} \cdot \mathbf{q}_r(\mathbf{x}) = \kappa(\mathbf{x}) \int_{4\pi} I(\mathbf{x}, \mathbf{s}) d\Omega - 4\sigma T(\mathbf{x})^4 \quad \text{Equation 33}$$

In words, the net radiant energy gained by a grid cell is the difference between that which is absorbed and that which is emitted.

2.6 Pyrolysis Model – Thermally Thick Solid

This work only discusses the pyrolysis model for a thermally thick solid, which is also referred to semi-infinite solid. For a thermally thick solid, the slab is heated on one side only, with insignificant heat losses from the rear face. In many fire engineering problems involving transient surface heating, it is adequate to assume "thermally thick behavior" if $\Delta > \delta$, where Δ is the thickness of the solid in interest, δ is the thermal penetration depth and $\delta \propto \sqrt{\alpha t}$ ²⁴.

Firstly, the solid is heated by incident heat **flux** and the surface temperature is increased. One-dimensional heat conduction equation for the material temperature, $T_s(x; t)$ is applied in the direction x pointing into the air/solid interface ($x = 0$):

$$\rho_s c_s \frac{\partial T_s}{\partial t} = k_s \frac{\partial^2 T_s}{\partial x^2} \quad \dots \text{ for } T_s < T_p \quad \text{Equation 34}$$

$$-k_s \left. \frac{\partial T_s}{\partial x} \right|_{\text{surface}} = \dot{q}_c'' + \dot{q}_r'' - \dot{q}_{RR}'' \quad \text{Equation 35}$$

where ρ_s , c_s and k_s are the constant density, specific heat and conductivity of the solid;

\dot{q}_c'' , \dot{q}_r'' and \dot{q}_{RR}'' are the convective, radiative and re-radiation heat fluxes at the surface.

While the heat-up proceeds to a level that the surface temperature attains to a prescribed pyrolysis temperature of the solid, T_p , the boundary conditions of the above 2 equations change to:

$$T_s(0, t) = T_p, \quad \dot{q}_p'' = \dot{q}_c'' + \dot{q}_r'' - \dot{q}_{RR}'' - k_s \left. \frac{\partial T_s}{\partial x} \right|_{\text{surface}} \quad \text{Equation 36}$$

Here, \dot{q}_p'' is energy available for pyrolyzing fuel via the simple relationship:

$$\dot{m}'' = \frac{\dot{q}_p''}{\Delta H_v} \quad \text{Equation 37}$$

where \dot{m}'' is the burning rate or mass loss rate, while ΔH_v is the heat of vaporization,

2.7 Proposed Algorithm for Surface Temperature of Thermally-thick Material

In FDS, a solid has thickness δ . This thickness is divided into N cells.

Temperature in i th cell, $T_{s,i}$, is obtained in time with a Crank-Nicholson scheme:

$$\frac{T_{s,i}^{n+1} - T_{s,i}^n}{\delta t} = \frac{\alpha}{2} \left(\frac{T_{s,i+1}^n - 2T_{s,i}^n + T_{s,i-1}^n}{\delta x_s^2} + \frac{T_{s,i+1}^{n+1} - 2T_{s,i}^{n+1} + T_{s,i-1}^{n+1}}{\delta x_s^2} \right) \quad \text{Equation 38}$$

where $1 \leq i \leq N$. Boundary condition is discretized as:

$$-k_s \frac{T_{s,1} - T_{s,0}}{\delta x_s} = \dot{q}_c'' + \dot{q}_r'' - \dot{q}_{RR}'' \quad \text{Equation 39}$$

and wall temperature $T_w = (T_{s,0} + T_{s,1}) / 2$.

As δ is defined by the user, and N is 20 by default, the accuracy of the results by the Crank-Nicholson scheme depend upon the resolution of the FDS grid size.

An alternative algorithm is proposed, that has no dependency upon the resolution of grid size. It is based on the same physical model of 1-D heat conduction, i.e. equation 29. A solution was developed to estimate the surface temperature when a solid is exposed to a time-related net surface heat flux $\dot{q}_{net}''(\tau) = \dot{q}_c'' + \dot{q}_r'' - \dot{q}_{RR}''$:

$$T_s - T_\infty = \frac{1}{\sqrt{\pi k \rho c}} \int_0^t \frac{\dot{q}_{net}''(\tau)}{\sqrt{t-\tau}} d\tau \quad \text{Equation 40}$$

In order to solve the above equation, the incident heat flux as a function of time has to be provided as a given input.

The detailed derivation of the solution for the above equation is enclosed as Appendix A, and the solution is:

$$T_s^{n+1} = T_\infty + \frac{1}{\sqrt{\pi \cdot k \rho c}} (I_1 + I_2) \quad \text{Equation 41}$$

where $I_1 = \Delta t \left[\frac{1}{2} \frac{\dot{q}_{net}''(t^{(1)})}{\sqrt{t^{(n+1)} - t^{(1)}}} + \frac{\dot{q}_{net}''(t^{(2)})}{\sqrt{t^{(n+1)} - t^{(2)}}} + \dots + \frac{\dot{q}_{net}''(t^{(n-1)})}{\sqrt{t^{(n+1)} - t^{(n-1)}}} + \frac{1}{2} \frac{\dot{q}_{net}''(t^{(n)})}{\sqrt{t^{(n+1)} - t^{(n)}}} \right]$ and

$$I_2 = \sqrt{\Delta t} (\dot{q}_{net}''(t^{(n+1)}) + \dot{q}_{net}''(t^{(n)})).$$

Comparing to the existing algorithm for surface temperature, the proposed algorithm is independent of the resolution of FDS domain. Furthermore, this is computationally cost-effective.

2.8 Proposed Algorithm for Burning Rate of Thermally Thick Material

The following algorithm was developed and presented by Quintiere et al.^{25, 26, 27} using a one-dimensional heat transfer model.

First, the preheating period before pyrolysis is examined to obtain the thermal penetration depth which is a function of time. Again, the one dimensional unsteady conduction equation, as Equation 34, applies; plus the constant initial temperature,

$$t = 0, T = T_\infty \quad \text{Equation 42}$$

and at the surface.

$$\left(-k \frac{\partial T}{\partial y} \right)_{solid, y=0} = \dot{q}_{net}'' = [-h_c (T_s - T_g)] + \dot{q}_{f,r}'' + (1-r)\dot{q}_r'' - \epsilon \sigma T_s^4 \quad \text{Equation 43}$$

Employing a standard approximate integral solution to solve the above problem, at some penetration depth, δ , from the surface, the temperature is T_∞ and the heat **flux** is zero, i.e.:

$$y = \delta, T = T_0 \text{ and } \frac{\partial T}{\partial y} = 0 \quad \text{Equation 44}$$

The integral equation is derived by integrating Equation 34 for $0 \leq y \leq \delta(t)$. It can be shown that it becomes:

$$\frac{d}{dt} \int_0^\delta (T - T_\infty) dy = -\alpha \left(\frac{\partial T}{\partial y} \right)_{y=0} \quad \text{Equation 45}$$

A polynomial profile for T within δ is assumed:

$$T = Ay^2 + By + C \quad \text{Equation 46}$$

A, B, and C are determined by applying the boundary conditions given by Equation 42, Equation 43, and Equation 44. This follows as:

$$A = -\frac{B}{2\delta} \quad \text{Equation 47}$$

$$C = T_\infty - \frac{B}{2\delta} \quad \text{Equation 48}$$

$$kB + h_c \frac{B}{2\delta} + \dot{q}_{f,r}'' + (1-r)\dot{q}_r'' - \epsilon\sigma \left(T_\infty - \frac{B}{2\delta} \right)^4 = 0 \quad \text{Equation 49}$$

Substituting this profile into Equation 45, along with the initial conditions:

$$t=0, \delta=0 \quad \text{Equation 50}$$

yields,

$$\delta = \sqrt{6\alpha t}$$

Equation 51

which is independent of the parameter B.

The complete solution is found by solving Equation 49 at each time by a Newton-Raphson method to find B. Then the solution is carried out in time until $T(0,t)=C=T_p$. The values of δ and the temperature profile at the time of the onset of pyrolysis provide the initial conditions for the gasification period discussed next.

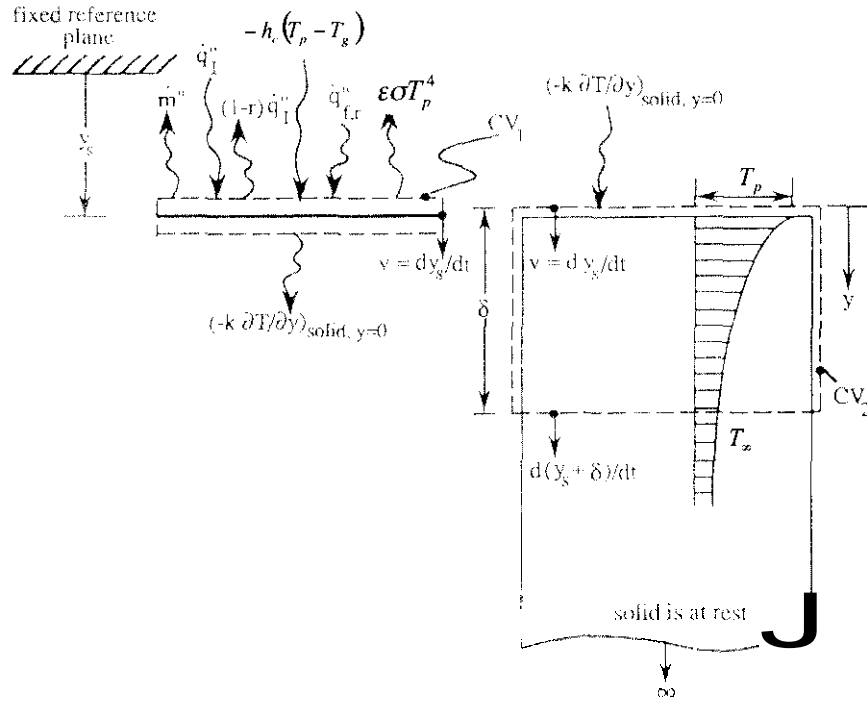


Figure 2 – Heat & Mass Transfer Processes for a Thermally Thick Material ²⁷

Then, the gasification period following the preheating stage is discussed. The governing equations for the gasification period of thermally thick material can be derived in integral form from the control **volumes** (CVI and CV2) selected in Figure 2

for the vaporization plane and solid respectively. The integral equation can also be derived by integrating the partial differential equation of Steckler et al.²⁸ over the penetration depth, δ .

Conservation of mass applied to the solid CV2 expresses that the rate of mass changed in CV2, which is defined by an increasing δ , is equal to the rate of mass entering the control volume at $y = \delta$. Conservation of energy applied to CV2 considers enthalpy transport across the moving vaporization surface, before vaporization occurs, by the mass flux ρv (v is the surface regression velocity, $v = dy_s/dt$); and enthalpy transfer across the surface defined by δ due to the mass flux, $\rho (d\delta/dt + v)$, which enters the CV. Specific heat for the solid at constant pressure and volume are assumed equal and the reference state for enthalpy is taken at T_∞ . Hence, for CV2:

$$\rho c \frac{d}{dt} \int_0^\delta (T - T_\infty) dy + \dot{m}'' c (T_p - T_\infty) = \left(-k \frac{\partial T}{\partial y} \right)_{solid, y=0} \quad \text{Equation 52}$$

Conservation of energy for CVI yields:

$$\dot{m}'' \Delta H_V = \left[-h_c (T_p - T_g) \right] \left(-k \frac{\partial T}{\partial y} \right)_{solid, y=0} + \dot{q}_{f,r}'' + (1-r) \dot{q}_r'' - \varepsilon \sigma T_p^4 \quad \text{Equation 53}$$

With the boundary conditions:

$$\begin{aligned} y = 0, T &= T_v \\ y = \delta, T &= T_0 \text{ and } \frac{\partial T}{\partial y} = 0 \end{aligned} \quad \text{Equation 54}$$

Again, a polynomial temperature profile within δ is assumed for the integral solution:

$$T = Ay^2 + By + C \quad \text{Equation 55}$$

Using the three boundary conditions in Equation 54, the parameters A, B, and C are obtained:

$$A = \frac{(T_p - T_\infty)}{\delta^2}, \quad E = -2\frac{(T_p - T_\infty)}{6}, \quad C = T_p \quad \text{Equation 56}$$

Substituting Equation 55 and Equation 56 into Equation 52, it becomes:

$$\frac{\rho c(T_p - T_\infty) d\ddot{a}}{3} + \dot{m}'' c(T_p - T_\infty) = -\frac{2k(T_p - T_\infty)}{\ddot{a}}, \text{ or:}$$

$$\frac{1}{3} \frac{da}{dt} + \frac{\dot{m}''}{\rho} = \frac{2a}{a} \quad \text{Equation 57}$$

The initial conditions at the onset of pyrolysis are the values when the surface temperature of the heat-up process achieves T_p . And the initial value of δ in Figure 2 right before pyrolysis is $\delta(t = t_p) = \sqrt{6\alpha t_p}$. In summary, the initial conditions at the onset of pyrolysis are:

$$t = t_p, \quad T_s = T_p \text{ and } \delta(t = t_p) = \sqrt{6\alpha t_p} \quad \text{Equation 58}$$

Let $\dot{q}_{net}''(\tau) = \dot{q}_c'' + \dot{q}_r'' - \dot{q}_{RR}''$ as the net surface heat **flux**, or:

$$\dot{q}_{net}'' = [-h_c(T_p - T_g)] + \dot{q}_{f,r}'' + (1 - r)\dot{q}_r'' - \varepsilon \sigma T_p^4 \quad \text{Equation 59}$$

Substituting Equation 59 into Equation 53, and substituting Equation 56 into the derivative of $\frac{\partial T}{\partial y}$, Equation 53 can be rewritten as:

$$\left(-k \frac{\partial T}{\partial y}\right)_{solid, y=0} = \dot{q}_{net}'' - \dot{m}'' \Delta H_V = \frac{2k(T_p - T_\infty)}{\delta} \quad \text{Equation 60}$$

Explicitly,

$$\dot{m}'' = \frac{\dot{q}_{net}'' - \frac{2k(T_p - T_\infty)}{\delta}}{\Delta H_V} \quad \text{Equation 61}$$

Utilizing the initial condition at pyrolysis as Equation 58, and discretizing Equation 57, the burning rate algorithm is summarized as:

$$\text{Before ignition: } t \leq t_{ig} : \begin{cases} T_s^{n+1} = T_\infty + \frac{1}{\sqrt{\pi \cdot k \rho c}} (I_1 + I_2) \\ \dot{m}'' = 0 \end{cases} \quad \text{Equation 62}$$

$$\text{After ignition: } t > t_{ig} : \begin{cases} T_s = T_l \\ \delta_{n+1} = \left(\frac{6\alpha}{\delta_n} - \frac{3\dot{m}_n''}{\rho} \right) \cdot \Delta t + \delta_n \\ \dot{m}_{n+1}'' = \frac{1}{\Delta H_V} \cdot \left[\dot{q}_{net, n+1}'' - \frac{2k(T_p - T_\infty)}{\delta_{n+1}} \right] \end{cases} \quad \text{Equation 63}$$

In summary, the existing FDS algorithm utilizes similar physics while the proposed model eliminates the need for a repeated solution of the PDE. A benefit is reduced computation cost. The potential weakness of the proposed model for mass burning rate is that it is for a non-charring semi-infinite solid.

The proposed algorithm is not incorporated into the FDS code and is a subject of future study for quantifying its computational benefits, and the following evaluations on the FDS code are based on the existing models.

3 BACK'S WALL FIRE TESTS

The series of experiments used in the study was performed by Back et al.²⁹ These fire tests showed that the peak wall heat fluxes, for fires of 50-500 kW, could be 40–120 kW/m². Such heat fluxes are sufficient to ignite most combustible materials. It is crucial that the heat flux prediction by FDS can be maintained at a reasonably accurate level, in order to achieve reasonable results for surface flame spread and subsequent flashover prediction. This work is to provide a comparison between the FDS prediction and the experimental data.

3.1 Description of the Wall Fire Experiment

Incident wall heat flux distributions have been measured for square propane burner fire sources placed against the wall. Peak heat fluxes of 40–120 kW/m² were measured for energy release rates of 50–500 kW/m² and burner edge lengths of 0.28–0.7 m. **Peak** heat flux was found to be a strong function of energy release rate but were insensitive to burner size. The experimental apparatus is shown in Figure 3. The specific test conditions are included in Table 1.

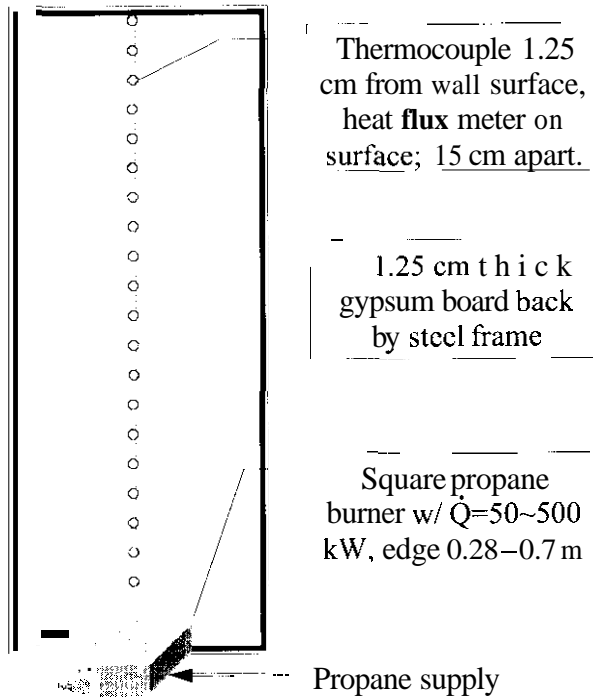


Figure 3 – Experimental Setup for Beck's Wall Fire

Eight Medtherm total heat flux transducers were installed flush with the wall surface. A vertical array of thermocouples was installed beside the total heat flux array, approximately 1.25 cm from the wall surface.

3.2 Back's Experimental Results

Flame Height

Flame heights were measured by visual analysis of the videotape and thermocouple measurements. The time-averaged and 50% visual intermittence results of these measurements are shown in Table 1.

Centerline Temperatures

After adjusting the data for the experimental virtual source (z_0), the data appear to lie in two discrete regions, the flame and the plume. The temperatures in the continuous combustion region are approximately constant (900 °C). The temperatures in the non-reactive zone decrease as a function of height and the energy release and are well represented by the following correlation:

$$\Delta T_{CL} = 40.6 \dot{Q}^{2/3} (z - z_0)^{-5/3} \quad \text{for } (z - z_0) / \dot{Q}^{2/5} > 0.16 \quad \text{Equation 64}$$

Beck et al. also found out that their experimental virtual source, z_0 , was in agreement with Heskestad's correlations:

$$z_0 = 0.083 \dot{Q}^{2/5} - 1.020 \quad \text{Equation 65}$$

Heat Flux

The centerline measured heat flux profiles are shown in Figure 2 with the height normalized by the flame height. The flux is approximately equal to the peak flux over the lower 40% of the flame height and decays to 20 kW/m² at the flame height. The consistency of the 20 kW/m² incident flux at the flame height and its correspondence with a blackbody at 500 °C is good, as 500 °C matches the visible flame.

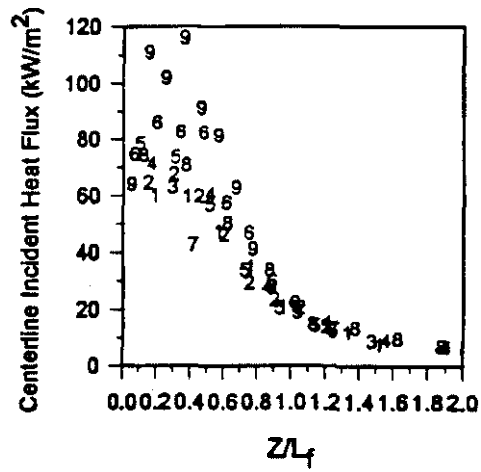


Figure 4 – Measured centerline heat flux

Test Number	\dot{Q} (kW)	D (m)	Z^* (m)	\dot{Q}_D^*	50% Visual Intermittence Flame Height (m)	Time-averaged 500 °C Flame Height (m)
1	53	0.28	0.298	0.867	0.79	0.78
2	56	0.70	0.305	0.093	0.36	0.33
3	68	0.48	0.330	0.289	0.60	0.51
4	106	0.37	0.394	0.864	1.00	1.02
5	136	0.48	0.435	0.578	0.87	0.86
6	204	0.48	0.512	0.868	1.45	1.45
7	220	0.70	0.527	0.364	1.20	1.29
8	313	0.57	0.607	0.866	2.20	2.29
9	523	0.70	0.746	0.866	--	2.90

Table 1 – Experimental Results and Flame Height

4 EVALUATION OF THE FDS-PREDICTION ON BACK'S WALL TEST

4.1 FDS Input

The geometry data, i.e. the wall and the burner, was taken directly from the experimental setup. The domain consists of a solid wall against the burner on the floor, and all other walls are set as openings to the ambient. Ma has recommended that the cell size be 5% of z^* , the characteristic plume length scale, for accurate simulation results using the FDS³¹. And z^* is represented by:

$$z^* = \left(\frac{\dot{Q}}{\rho_{\infty} c_p T_{\infty} \sqrt{g}} \right)^{2/5} = (\dot{Q}_D^*)^{1/5} \cdot D \quad \text{Equation 66}$$

Where in this case, the ambient temperature is selected as 20 °C.



Figure 5 – FDS Simulation Domain for Back's Wall Fire Test

In the test, the wall was constructed of gypsum wallboard with a very low conductivity and back-surface heat loss. Keeping this in mind, a wall with actual gypsum thermal properties was used with the values³⁰ of $k=0.48$ W/m-K, $\alpha=4.1 \times 10^{-7}$ m²/s and thickness=0.013 m. This unreleased version of FDS used in this paper, V. 1.99 dated April 30th 2001, has incorporated variable specific heat as a function of temperature.

4.2 FDS Predictions on the Centerline Temperature

The time-averaged centerline temperature was correlated by Equation 64. That was measured 1.25 cm from the wall, at the center of the burner. The corresponding results were computed from the FDS. Runs for each test configuration in Table 1 were computed for 10 seconds of simulation time. This was done on a Pentium3-866MHz, 384MB computer which took 1–1.5 hour for about each simulation second. The corresponding time-averaged temperature were computed from 3 to 10 seconds of simulation time. The comparison between the experimental correlation and the FDS simulation is shown in Figure 6, the numbered curves correspond to the Test Number in Table 1. Both sets descend while \dot{Q}_D^* decreases. In the lower part of the flame region, the model over-predicts by 20–30% the gas temperature, which is empirically defined by a fixed temperature of 900 °C. In the upper part of the flame region and in the plume region, the FDS-predicted temperature falls quickly and the result is poor.

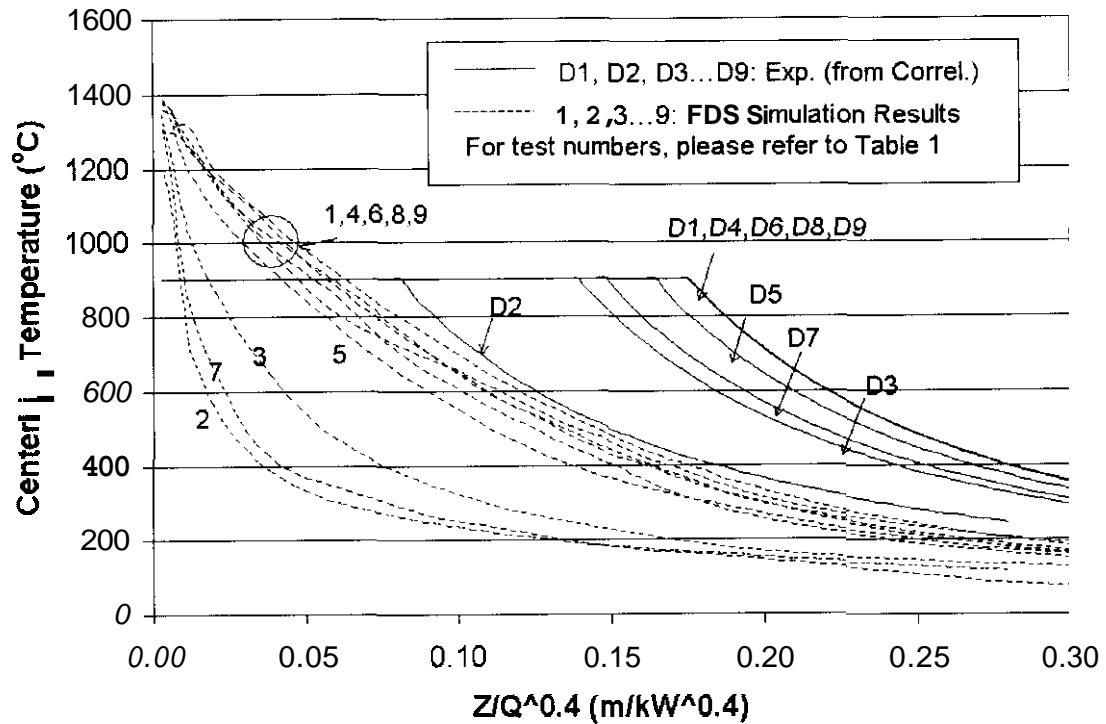


Figure 6 – Centerline Gas Temperature (1.25 cm against wall) – All Tests

4.3 FDS Predictions on the Wall Heat Flux Distribution

As shown in Figure 7, the model successfully predicts the maximum flux, which is located just above the fuel surface. However, similar to the predictions for temperature, the predictions for heat flux level decay quickly. For **example**, the experimental data showed that flame height is at 1.45 m for Test 6; however, at this height, the model predicts a total heat flux as low as 5 kW/m₂, which is substantially lower than the measured total heat flux of 20 kW/m₂ at the flame height.

As shown in Figure 8, the heat flux was broken down as radiative heat flux and convective heat **flux**, and compared to the experimental results.

The distribution of radiation heat flux and convective heat flux is satisfactory. Convective heat fluxes are predicted at maximum 20 kW/m^2 at the base of the wall, and it gradually decreases to $2\text{--}5 \text{ kW/m}^2$ while the height increases. The radiative portion, that is dominant, is decreasing quickly as the height increases, and this finding may suggest further improvement in the radiation sub-model he needed.

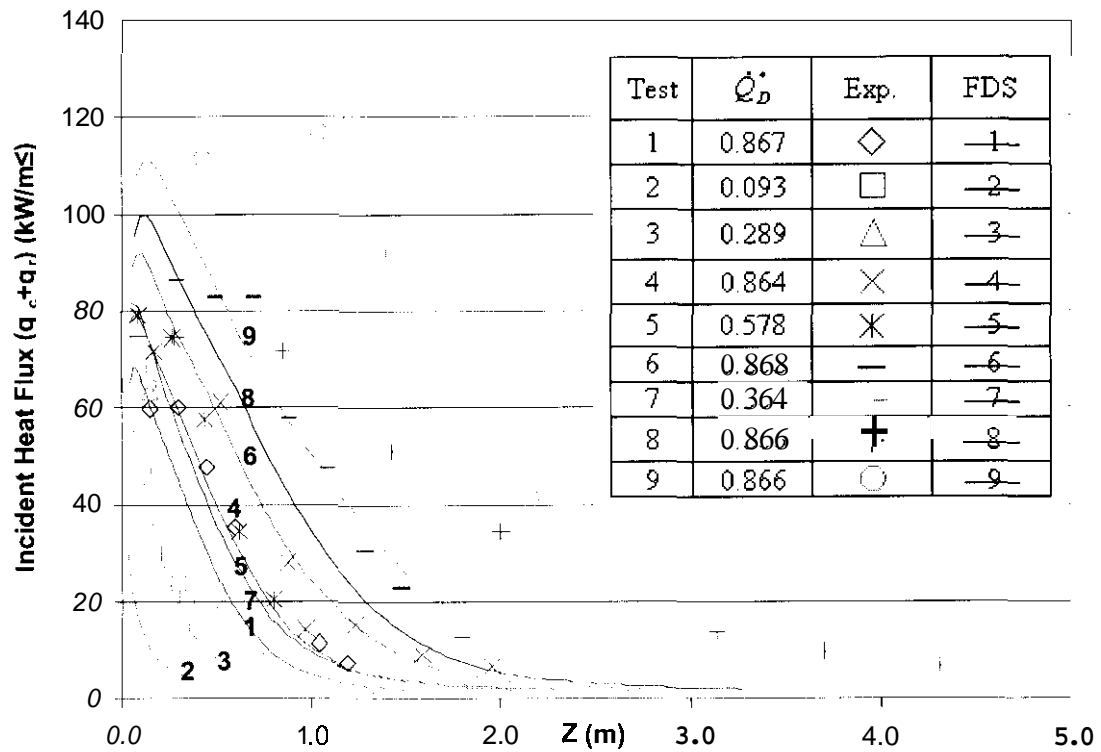


Figure 7 – Heat Flux Distribution

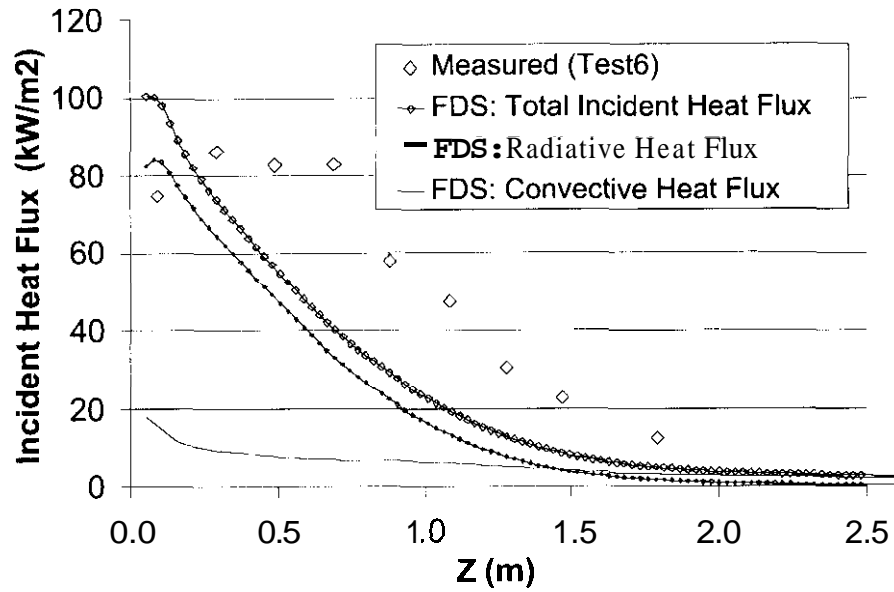


Figure 8 – Heat Flux Distribution for Test 6

4.4 FDS Predictions on the Flame Height

Figure 7 plots the dimensionless results for flame height. The data are indicated by the test numbers. The correlation for the axisymmetric freestanding fires is given by Heskestad:

$$z_f = 0.23\dot{Q}^{2/5} - 1.02D \quad \text{Equation 67}$$

The simulation flame height was based on the time averaged from 3 to 10 seconds for the locus of the energy released rate at which it achieves 99, 99.9, and 99.99% of its full value. Ma³¹ found that the 99.99% locus best matched axisymmetric free tire plume data.

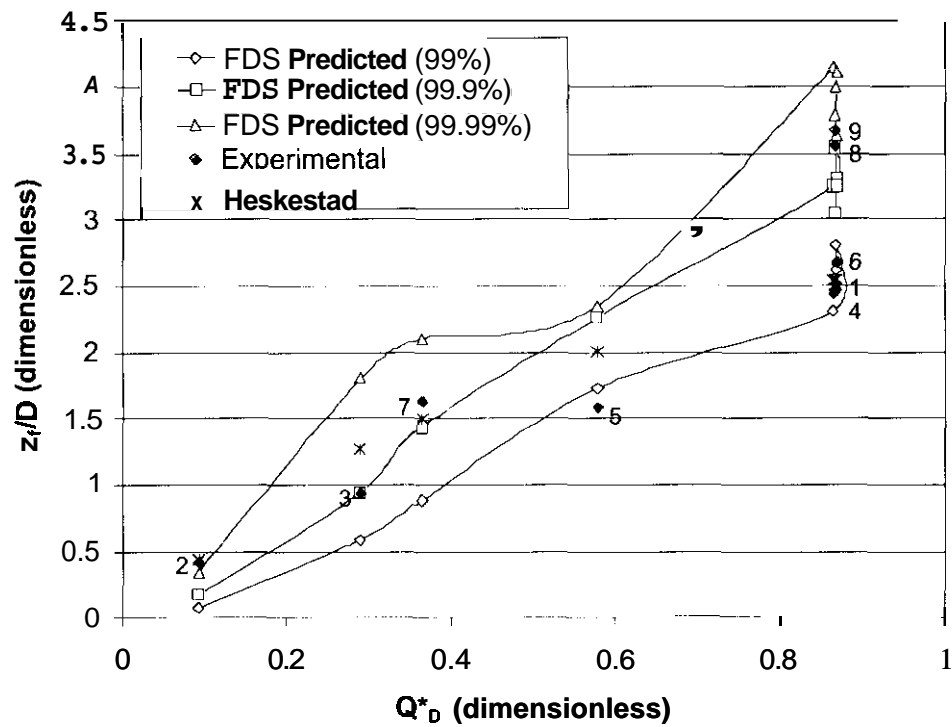


Figure 9 – Flame Height

4.5 Summary of the FDS Predictions on Beck's Wall Fire Tests

The FDS/LES model gives results for temperature, wall heat flux, and flame in qualitative agreement with data. The temperature and the heat flux are within about 30% of measured results for peak values near the base of the wall, but both drop much quicker than the experimental results. The weakness appears to be combustion model which is giving too high temperature predictions inside the flame region (Figure 6).

5 FM'S LARGE SCALE PMMA WALL FIRE TEST

The benchmark data set to be compared with the FDS prediction was developed by Factory Mutual Research Corporation. Tewarson³² performed a comprehensive study on the flammability, flame spread, and flame extinction behaviors of polymethylmethacrylate (PMMA) slabs. A couple of years later, Wu et al.³³ at FMRC continued the research. In validating FMRC's Flame Spread & Growth model, as well as providing badly needed full-scale heat flux data, an upward fire spread experiment was carried out under the Fire Products Collector at the FMRC Test Center.

5.1 FMRC 500-kW-Scale Flammability Apparatus and the Experimental Setup

In the experiments³², polycast PMMA with a density of 1190 kg/m^3 was used. The 500-kW Scale Flammability Apparatus consists of a lower section and an upper section.

The lower section is used for the measurements of time to ignition, mass loss rate during pyrolysis and combustion, pyrolysis and flame heights, and flame spread rate, as well as concentrations of Y_θ and gaseous agents and water application rate required for flame extinction. The upper section is used for the measurements of total mass and volumetric flow rates of chemical compounds – air mixtures, temperature, concentrations of CO, CO₂, O₂, total gaseous hydrocarbons, H₂O, particulates, and other compounds such as HCl, NO, and NO₂, and optical transmission, corrosive nature of the chemical compounds-air mixture, and electric charge on the particulates.

The full-scale, upward fire spread experiment was conducted, using a 0.025 m thick PMMA wall, 0.58 m wide x 5 m high. The PMMA wall was extended another **0.3** m on each side by Marinite panels. At the outer edge of the Marinite panels, a perpendicular 0.6 m flow barrier (24 gauge) steel is used *to* minimize the effects of room drafts. On the top of the wall, a 3 m extension provides a background for measuring the flame heights. Among many data acquisition instruments, seven total heat flux gauges and thermocouples were placed at various on the PMMA wall.

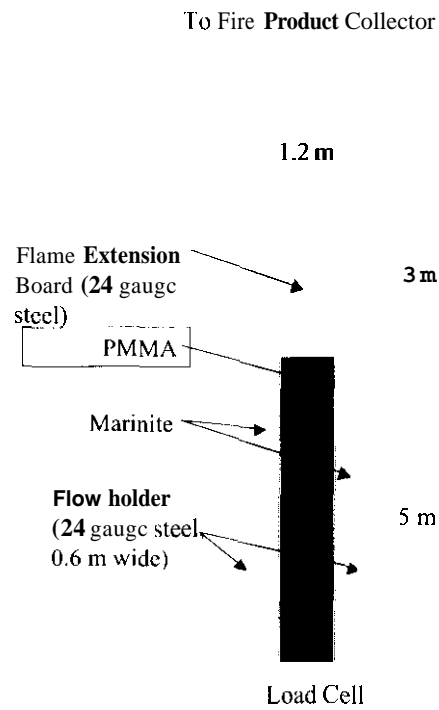
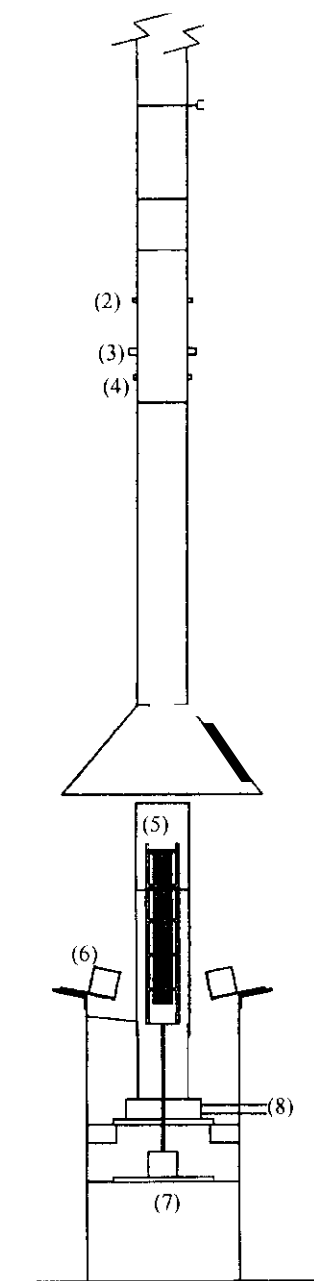


Figure 10 – Full Scale PMMA Wall Fire Test³³



Symbol	Equipment List
1	Blast gate and linear actuator control
2	Particular sampling; pressure and corrosion measurement
3	Optical transmission measurement
4	Gas temperature measurement
5	Vertical testing sample slab
6	Infrared heaters
7	Load cell
8	Air and oxygen inlet

Figure 11 – FMRC 50-kW Flammability Apparatus as shown. The 500-kW apparatus is similar except for size.³²

The experiment was performed in the 500-kW Scale Flammability Apparatus, using vertical slabs. To hold the samples in a vertical orientation, a ladder-like sample holder was used, as shown in Figure 11. Flame spread was restricted to a single surface by tightly covering the back of the slab with a 3-mm thick ceramic paper.

For ignition of flame spread with a uniform pyrolysis front for each test, a 0.025-m-high, 0.025-m-wide, 0.10-m-long aluminum dish containing about 10 ml methanol was placed at the bottom of the slab and ignited by a match.

For the measurement of pyrolysis height and flame spread rate, lines were marked at intervals of 25 mm on the surface across the width of the slabs. For the measurement of flame height, lines were marked every 25 mm on the sample holder and holes were made every 25 mm on the aluminum extension. A stopwatch was used to record visually times for pyrolysis front and flame tip arrival at each line.

Most of the flame spread experiments were performed at $v_g = 0.09$ m/s with v_g as the environment air velocity; the other value used was 0.18 m/s. These values were not expected to affect the flame spread rate, as they are significantly less than $v_g = 0.30$ m/s, at or above which flame spread is affected by the gas flow¹³.

In the experiments, mass loss rate during flame spread was not measured. However, initial and final weights of the samples were recorded.

In the upper section, all the compounds generated during pyrolysis, combustion, flame spread and extinction were captured, along with ambient air in the sampling duct. The upper section operates as large-scale cone calorimeter, so this is not of the interest of this work.

Thermal Properties	Value and Unit
k , conductivity	0.209 W/m-K
c_p , specific heat of the solid	1.46 kJ/kg-K
ρ , density of the solid	1 190 kg/m ³
$k\rho c_p$, thermal inertia	0.364 kW ² -s/m ⁴ -K ²
α , thermal diffusivity	1.2E-7 m ² /s
T_p , pyrolysis temperature	363 °C
ΔH_c , heat of combustion	26000 kJ/kg
ΔH_v , heat of vaporization	1108 kJ/kg

Table 2 – PMMA Thermal Properties Used in the FDS Simulation

5.2 A Close Look at PMMA's Thermal Properties

Poly(methyl methacrylate) (Figure 12), which is usually referred to as PMMA, is commonly called by its trade name PLEXIGLASTM. As a polymer undergoing a polymerization process, PMMA contains no cross-linking between long chain molecules, therefore it can be considered as a thermoplastic. PMMA is a vinyl polymer composed of vinyl monomers which is containing carbon-carbon double bonds. PMMA is thus the product of the polymerization of free vinyl radicals called monomer methyl methacrylate.

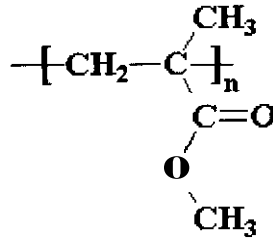


Figure 12 – PMMA

In a recent research done in the University of Maryland, College Park, Steinhaus and Torero ³⁵ evaluated the thermophysical properties of PMMA. The research investigated the temperature dependencies of many thermal properties of PMMA, which is determined by using the time to ignition t_{ig} and the time to pyrolysis t_p as obtained from the Forced Flow and Flame Spread Test. The following are the results presented by Steinhaus.

Density ρ

It is known that the density decreases linearly with increasing temperature and that the slope is constant. The following expression was obtained for the temperature dependent density, where the temperature T is given in degree Celsius:

$$\rho = -7.316 \cdot 10^{-4} \cdot T + 1.4045 \left[\frac{\text{g}}{\text{cm}^3} \right] \quad \text{Equation 68}$$

As denoted by the above expression, there is approximate 20% difference for the density at between 20 °C and 380 °C.

Specific Heat, c_p

The specific heat has to be broken down into two time dependent equations, as dictated by the glass transition phenomena of PMMA, as shown in Figure 13.


$$c_p = 2.041 \cdot 10^2 \cdot T^{-2} + 4.341 \cdot 10^{-3} \cdot T + 0.173 \left[\frac{J}{gK} \right] \quad \text{Equation } \mathbf{69}$$

$$c_p = 2.547 \cdot 10^{-3} \cdot T + 1.212 \left[\frac{J}{gK} \right] \quad \text{Equation 70}$$

Many investigators have conducted research on the thermal conductivity of A, and their results are summarized in Figure 14:

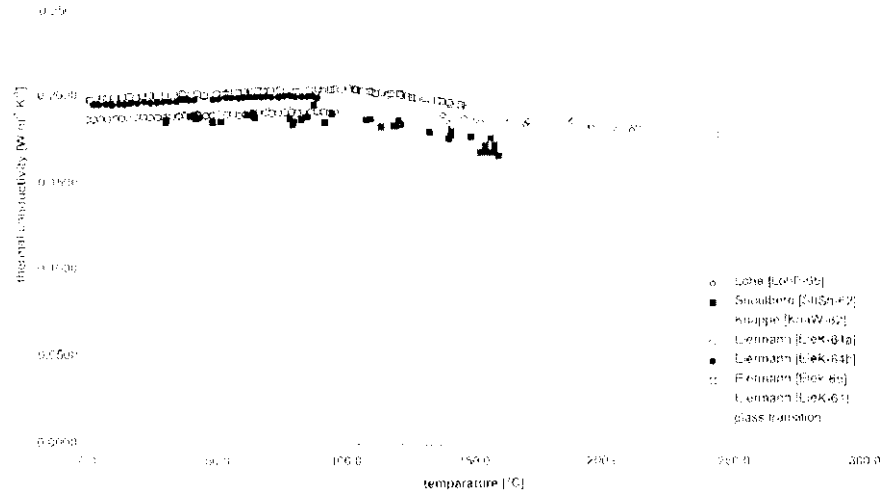


Figure 14– Thermal Conductivity of Various Solid and Molten PMMA ³⁵

The obtained curves for the thermal conductivity as a function of time for the area below the glass transition temperature are presented in Equation 71, while the area above the glass transition temperature is expressed in Equation 72. The temperature is in °C.

$$k = 4.954 \cdot 10^{-5} \cdot T + 0.1959 \left[\frac{W}{m \cdot ^\circ C} \right] \quad \text{Equation 71}$$

$$k = -2.318 \cdot 10^{-3} \cdot T + 0.2249 \left[\frac{W}{m \cdot ^\circ C} \right] \quad \text{Equation 72}$$

Pyrolysis Temperature, T_p

A series of tests were conducted and the results are presented in Figure 15, where the literature pyrolysis temperature is given by the manufacture of PMMA (Cyrus Industries) used by Steinhaus ³⁵:

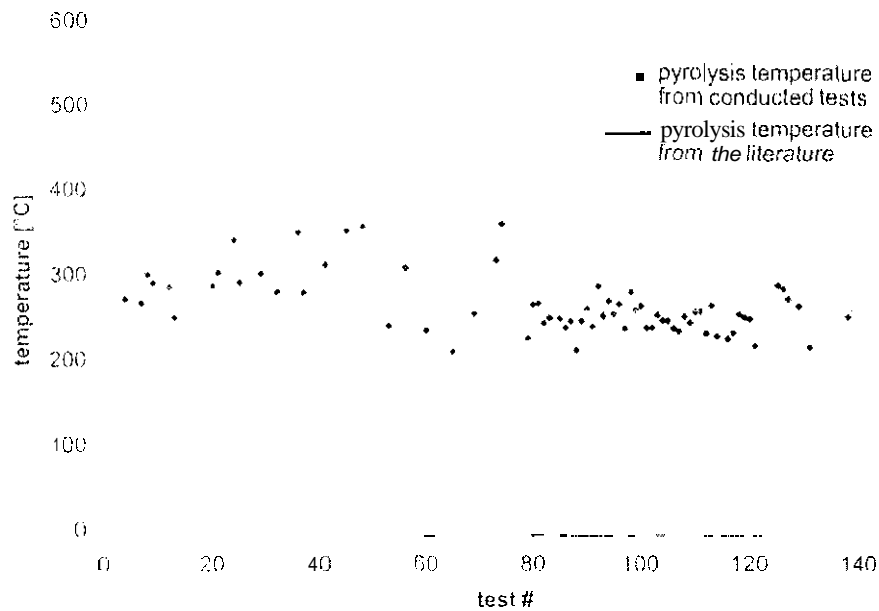


Figure 15 – Thermocouple Reading on the Surface of the Samples at the onset of pyrolysis³⁵

Obviously the PMMA used by Steinhaus is different from the one used by the FMRC benchmark experiment, however, Steinhaus' study showed that PMMA's thermal properties could vary by a great percentage between ambient temperature and pyrolysis temperature. Such nature of PMMA causes a major challenge to the numerical simulation of fire using FDS, which uses constant thermal properties for whole course of simulation, regardless of the sample temperature

5.3 FMRC Experimental Results

The measured total heat flux histories at various locations on the PMMA wall provide an important insight into the heat flux distributions in an upward propagating flame. As shown in Figure 16, the total heat flux histories along various heights were given. The pyrolysis height reached the top of the PMMA wall at about 1200 seconds.

The heat **flux** distributions are clearly going through three phases. Initially, the flame starts with a triangle-like profile. As the flame races up the PMMA wall, the profiles have a top-hat distribution with peak values between about 30–40 kW/m². Finally, after the pyrolysis zone reached the top of the PMMA wall, the profile evolves toward the steady state shape. Summing up the total energy gives a radiation fraction of about 0.26.

The pyrolysis height history is given in Figure 17, while the chemical heat release rate history is plotted in Figure 18.

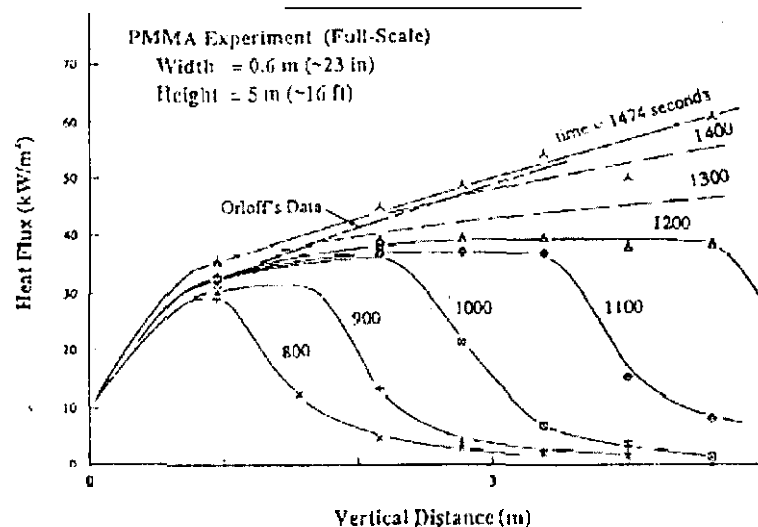


Figure 16 – Total Heat Flux Distribution at Various Time³³

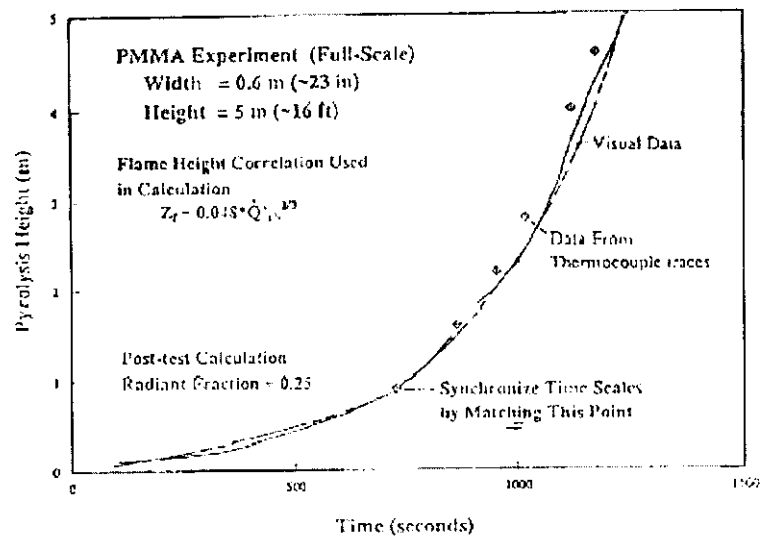


Figure 17 – Pyrolysis Height History³³

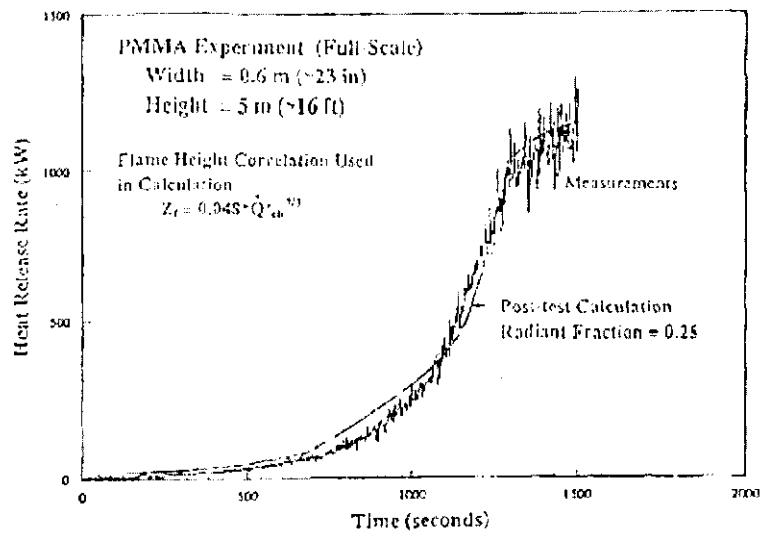


Figure 18 – Heat Release Rate History³³

6 EVALUATION OF THE FDS PREDICTION ON THE PMMA WALL TEST

6.1 FDS Implementation Issues

The FDS application of the existing burning rate model (Equation 34 – Equation 37) is examined hereinafter. The FDS input file used for the simulations follows in Figure 19. The FDS simulation domain is constructed as close to the real fire test as possible. All items in the real fire test is constructed into the Simulation Domain, including the PMMA vertical fuel wall, the marinite panels extended from the fuel wall and the steel sheet perpendicular to the marinite panels which is used to minimize the effects of room drafts.

According to Ma's finding³¹ on the dependency between the resolution of FDS domain and accuracy of FDS prediction, optimal results could be obtained if grid cell was set at about **5%** of z^* , where z^* is shown as a sole function of the fire intensity:

$$z^* = \left(\frac{\dot{Q}}{\rho_{\infty} c_p T_{\infty} \sqrt{g}} \right)^{2/5} = (\dot{Q}_D)^{1/5} \cdot D \quad \text{Equation 73}$$

In the FDS simulation, the fire intensity ranges from about 20 kW at the beginning as a result of the ignition device, to approximately 700 kW at the stage of quasi-steady burning over the whole PMMA wall. The corresponding z^* ranges from 0.21 m to **0.86 m**, while, **5%** of z^* gives a value between 1.0 cm and 4.3 cm. If the resolution of the FDS domain is chosen as 1.0 cm, however, there will be 3.6 millions cells in the domain, which is out of the existing FDS's handling capacity. Even with the

unofficial working version of FDS V2.2 that has been doubled the stacking size, such resolution may take months for a single simulation of 1500 seconds' flame spread test.

Then, the resolution had to be chosen as 3.75 cm, as a compromised result between fine resolution and length of computer time. With this resolution, the total number of cells is approximately 66,000. The simulations were calculated on a 1.7GHz Pentium IV[®] computer with 2048 MB of RDRAM memory. It took this computer approximately 150 hours of computer time for a simulation of 1800 seconds' flame spread.

In the Experiment, an ignition device was used and data had been recorded since the ignition device was turned on. The ignition device was a long hut narrow pan of alcohol pool fire along the wall base, ignited by a match, and lasted until self-sustained flame spread could be achieved on the wall. If to perfectly mimic such ignition device with a $z^* = 10$ mm, an unrealistic ultrahigh resolution would be needed and the number of cells would be as high as 10 millions. Hence, the exact simulation of the ignition device is impossible.

In the FDS Simulation, a small block of horizontal propane gas burner was placed at the bottom of the fuel wall, with prescribed initial fire size, to mimic the actual alcohol ignitor. The fire intensity of this mimicked ignitor was set as minimum as needed for ignition of the PMMA wall, and this was achieved by hand calculations and trials. The resulted fire intensity is around 20 kW, while compared to the actual fire test of approximate 10 kW, it is considered acceptable under the current computational power available in the market.

FDS INPUT FILE

```

&HEAD CHID='pmma'.TITLE='PMMA Wall Fire' /
LGRID IBAR=32, JBAR=16, KBAR=128 /
&PDIM XBAR=1.2, YBAR=0.60, ZBAR=5 /
&TIME TWFN=3000./

LMISC NFRAMES=3000, DTCORE=30, RESTART_FILE='pmma.restart', REACTION='MMA' /

LREAC ID='MMA',
      FYI='MMA monomer, C_5 H_8 O_2'
      EPUMO2=13542
      MW_FUEL=100
      NU_O2=6
      NU_H2O=4
      NU_CO2=5
      SOOT-YIELD=0.022 /

&SURF ID='PMMA'
      HEAT_OF_VAPORIZATION=1108
      HEAT_OF_COMBUSTION=26090
      DELTA=0.025
      KS=0.209
      ALPHA=1.2E-7
      DENSITY=1190
      TMPIGN=363 /

&SURF ID='FIRE', HRRPUA=2000 /

&SURF ID='MARINITE'
      ALPHA=1.14E-7
      KS=0.12
      DELTA=0.0254 /

&SURF ID='SHEET METAL'
      FYI='18 gauge sheet metal'
      C_DELTA_RHO=4.7
      DELTA=0.0013 /

&VENT CB='ZBAR', SURF_ID='OPEN' /
&VENT CB='YBAR', SURF_ID='OPEN' /

&VENT XB=0.00,0.30,0.0,0.0,0.00,5.00, SURF_ID='MARINITE' /
&VENT XB=0.90,1.20,0.0,0.0,0.00,5.00, SURF_ID='MARINITE' /

&VENT CB='XBAR0', SURF_ID='SHEET METAL' /
&VENT CB='XBAR', SURF_ID='SHEET METAL' /

LVENT XB=0.30,0.90,0.0,0.03,0.0,0.0, SURF_ID='FIRE' /
&VENT XB=0.30,0.90,0.0,0.0,0.0,5.00, SURF_ID='PMMA' /

&SLCF XB=0.00,1.20,0.05,0.05,0.00,5.00, QUANTITY='TEMPERATURE' /
&SLCF XB=0.60,0.60,-0.05,0.60,0.00,5.00, QUANTITY='TEMPERATURE' /

&BNDF QUANTITY='WALL-TEMPERATURE' /
&BNDF QUANTITY='BURNING RATE' /
&BNDF QUANTITY='HEAT_FLUX' /
&BNDF QUANTITY='CONVECTIVE_FLUX' /

```

Figure 19— Input File for FDS Simulation of the FM Wall Fire Test

6.2 Comparison of the Heat Release Rate History

Here, the experimental Heat Release Rate history (Figure 18) is used as the ground for synchronizing. By matching the initial HRR of 34 kW to Figure 18, the synchronizing point should be 350th seconds. When calculated ignition output was 34 kW, this was “synchronized” with the experiment time of 350 s. After synchronized, the Heat Release Rate history comparison is shown in Figure 20. Note that in all the following comparison, the time scales are synchronized by matching the 350th seconds.

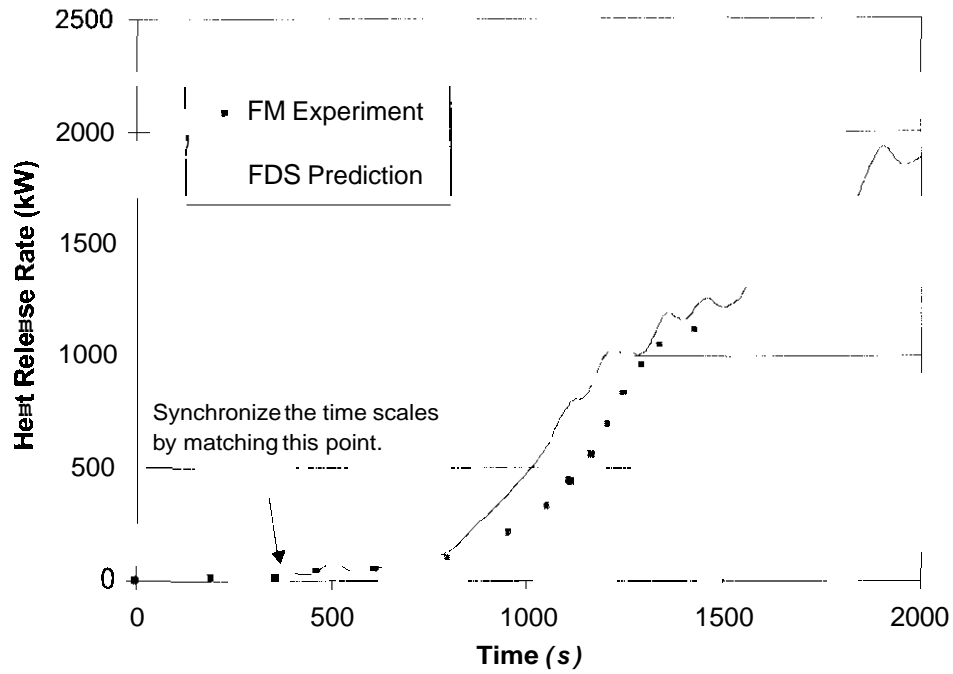


Figure 20 – Comparison of HRR History, After Synchronized (34 kW)

The FDS predicted HRR shown in Figure 20 are obtained by the equation

$\dot{Q} = \Delta H_c \cdot \sum \dot{m}_{cell}'' \cdot A_{cell}$. The FDS prediction is in excellent agreement with the experimental measurements

By default, the FDS uses $\dot{q}''' = \Delta H_o \cdot \dot{m}_o'''$ (Equation 23) for the Heat Release Rate per unit volume, and $Q = \sum \dot{q}''' \cdot V_{cell}$. However, if Equation 23 were to be used, the HRR would be underestimated by 50% maximum (not shown in Figure 20). The reason for such an underestimated heat release rate is that there is a limitation with the FDS domain described in Section 6.1. The actual experimental domain, as described in Figure 10 and Figure 11, includes a 3-m-high extension board above the 5-m-high PMMA wall. The fire product collector was installed above the extension board, and was taking account the whole combustion products. However, due to the constraints of time frame and computational power, the FDS domain used in this work is 8 m high, just including the PMMA wall. Thus, the combustion occurred above the 8 m PMMA wall that is out of this FDS domain, is not taken into account, and the heat released above the domain is not taken into account neither.

6.3 Comparison of the Flame Spread

Pyrolysis height predicted by the FDS is observed by mass **flux** ≥ 0 , or in other word, at the time of the pyrolyzed fuel starting to inject into the air. The result for pyrolysis height is shown in Figure 21. The code successfully simulated the upward flame spread in a satisfactory way.

The surface temperature profile predicted by FDS is presented in Figure 22. It shows the heating process of the PMMA wall by the wall fire. And it conforms to the upward flame spread phenomena, because the surface temperature increases when time

and height increases. The maximum value of the surface temperature is the prescribed pyrolysis temperature, in this case, 363 °C.

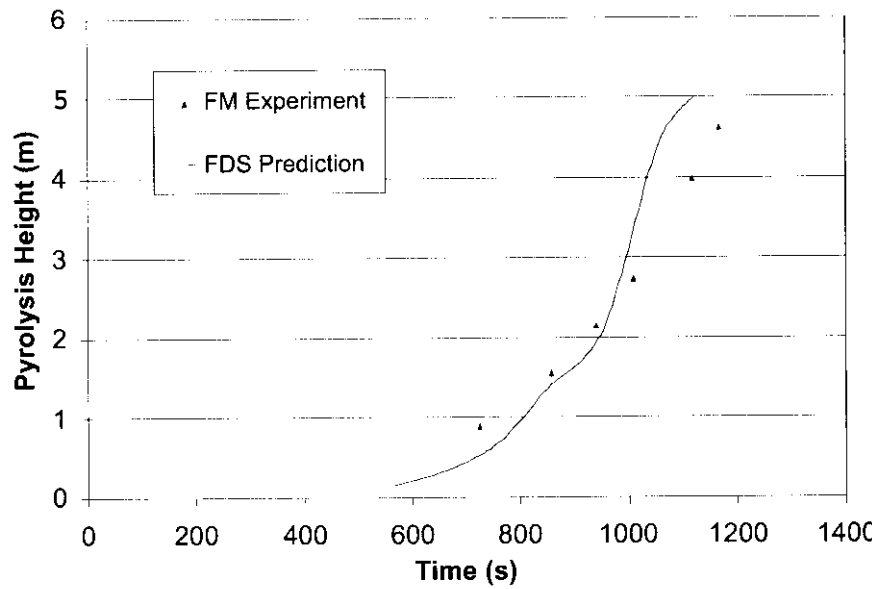


Figure 21 – Comparison of Flame Spread

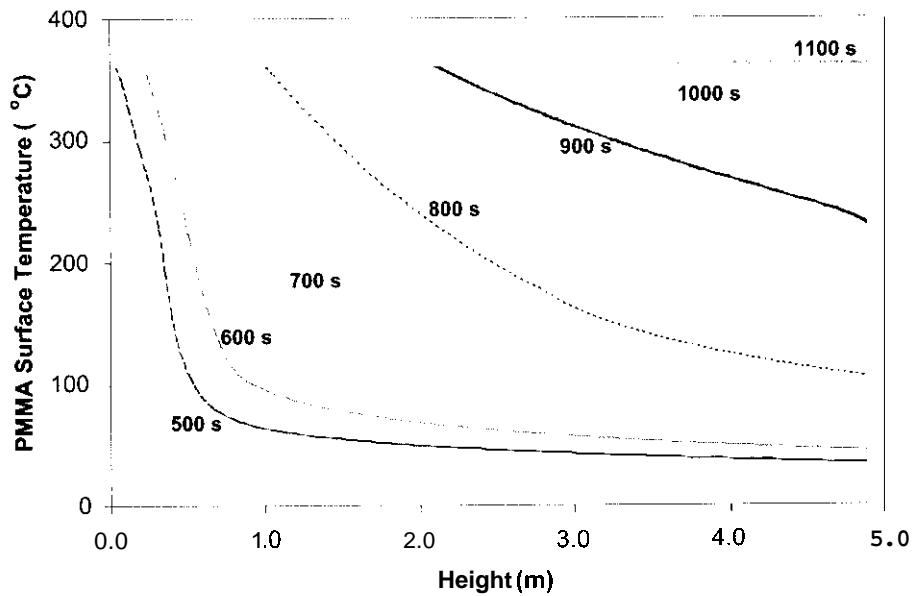


Figure 22 – PMMA Surface Temperature Calculated by FDS

6.4 Comparison of the Total Heat Flux

At various height, the measured maximum values for total heat fluxes are within the range of 30–40 kW/m². In FDS, the predictions gave the maximum values as high as 30 kW/m². However, the heat flux prediction decreases too quickly as the height increases. The finding is in good agreement with the finding in the no-spread case described in Section 4. The comparison of total heat flux distributions at various times is shown in Figure 23.

The FDS predictions on heat flux histories are time-averaged values of those values of the nearest ± 3 seconds, in order to minimize the moment fluctuations.

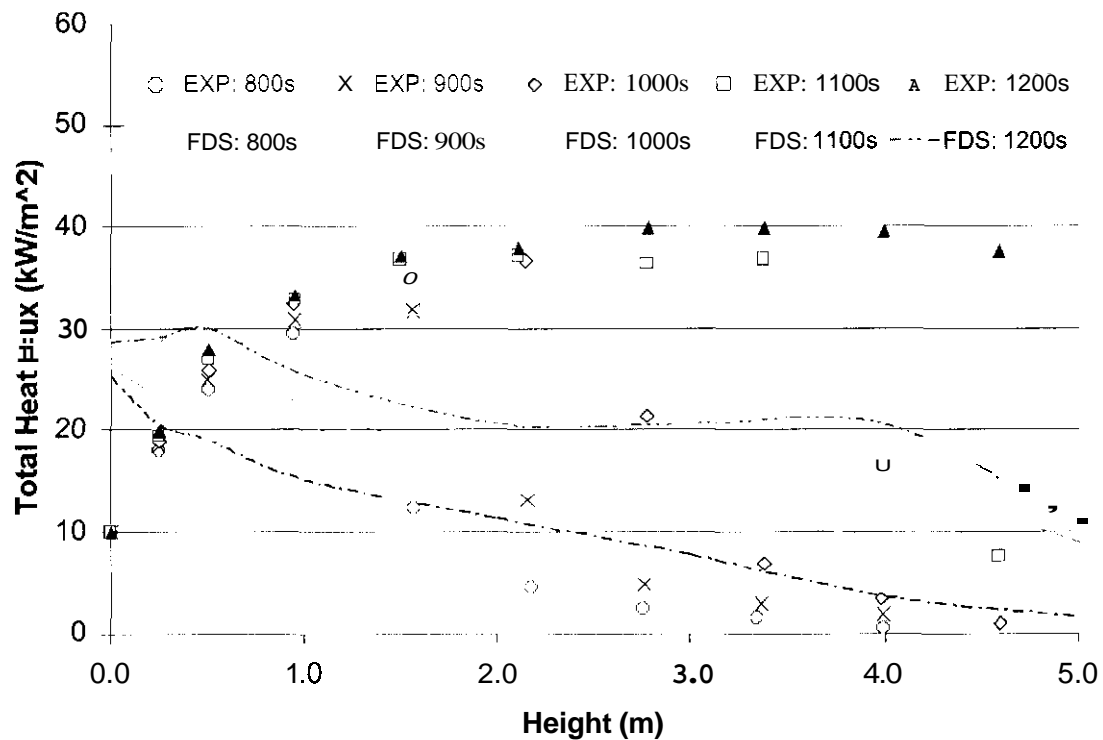


Figure 23 – Comparison of Total Heat Flux Distribution at Various Times

6.5 Comparison of the Burning Rate

Predictions of burning rate is taken from the quasi-steady stage during which the whole PMMA wall is involved, i.e. 1200s – 1500s. Although Wu's paper³³ didn't provide experimental data on the burning rate, the correlations by Ahmad and Faeth¹⁵ on turbulent convective burning of vertical plate is used as the benchmark. Orloff and co-workers at FMRC³⁶ had performed a smaller flame-spread experiment on the PMMA wall up to 1 m high as an earlier work prior to Wu's. Those experimental measurements are also served as benchmark data to validate the FDS predictions, which is time-averaged for the data between 1200s–1500s. The comparison is presented at Figure 24.

Ahmad and Faeth's correlation, as rewritten by Quintiere³⁷, for the average burning rate \bar{m}_F'' for a distance x measured from the start of the plate is given by the formula below:

$$\frac{\bar{m}_F'' \cdot x \cdot c_p}{k} = 0.0285 \left(Gr_x^* \right)^{0.73} / \Sigma \quad \text{Equation 74}$$

Where:

$$Gr_x^* = \left(\frac{L}{4c_p T_\infty} \right) \left(\frac{gx^3}{\nu^2} \right) \quad \text{Equation 75}$$

$$\Sigma = \left[\frac{(1+B)}{B \ln(1+B)} \right]^{0.5} \left[\frac{1+0.5 \text{Pr}/(1+B)}{3(B+\tau_o)\eta_f + \tau_o} \right]^{0.25} \quad \text{Equation 76}$$

$$\tau_o = \frac{c_p (T_p - T_\infty)}{L} \quad \text{Equation 77}$$

$$\eta_f = 1 - \left[\frac{r_o(B+1)}{B(r_o+1)} \right]^{1/3} \quad \text{Equation 78}$$

$$r_o = \frac{Y_{O_2,\infty}}{rY_{F_0}} \quad \text{Equation 79}$$

$$\bar{m}_F'' = \frac{1}{x} \int_0^x \dot{m}_F'' dx \quad \text{Equation 80}$$

The exact thermal properties of the PMMA as shown in Table 2 are used in Ahmad & Faeth's correlations, plus the environment variables for air at ambient temperature as shown in Table 3. The mass burning rate (\dot{m}_F'') from Ahmad & Faeth's correlation, as shown in Figure 24, are discretized values from the *averaged* mass burning rate (\bar{m}_F'') directly given by Equation 80

Thermal Properties	Value and Unit
K	25E-3 W/m-s
ν	15E-6 m ² /s
Pr	0.70
ρ	1.1 kg/m ³
c_p	1.05 kJ/kg-K
T_∞	293 K

Table 3 – Air Thermal Properties Used in Ahmad & Faeth's Correlations

Below, Figure 24 is the results when the whole PMMA wall is involved, for the quasi-steady burning stage. The results are time-averaged for the period between 1500–1800 s.

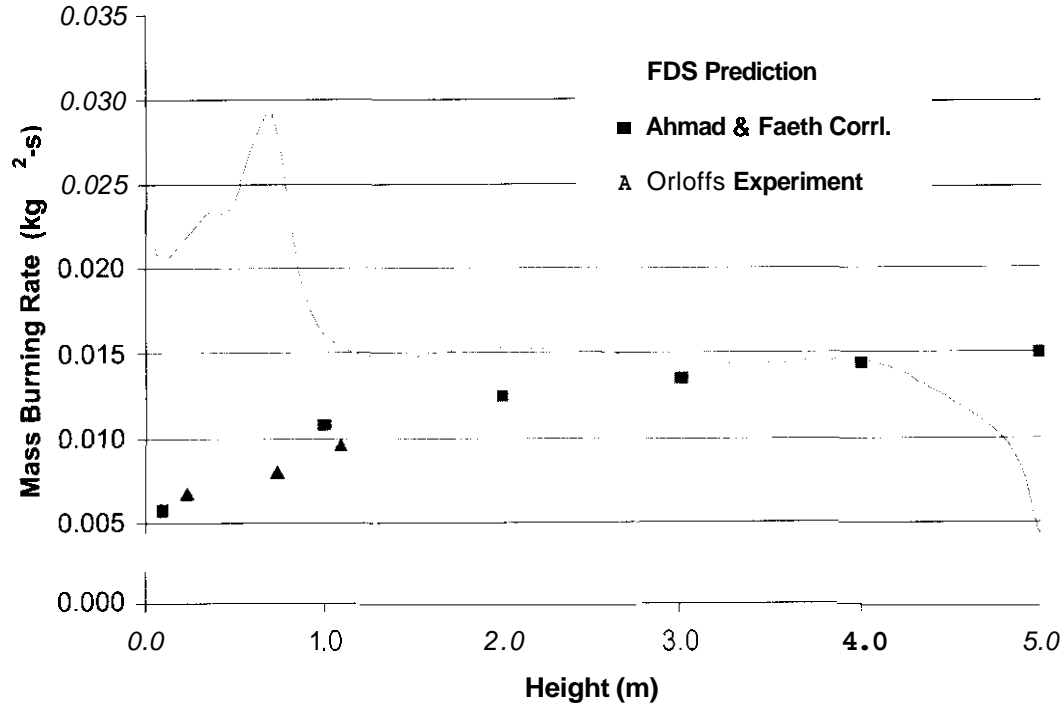


Figure 24 –Comparison of Mass Burning Rate

Again, the findings from Figure 24 shows an over-prediction of mass burning rate at the base of the vertical plate and somewhat under-prediction at the top of the vertical plate. This finding could be a result of heat flux and gas temperature prediction by FDS in the no-flame-spread case as examined in Figure 6, Figure 7 and Figure 8, where approximately 30% over-prediction of gas temperature within the flame region is observed. The mass burning rate for the region between 4 m and 5 m is underestimated. This may due to the limitation of the FDS domain used in this simulation, which omits the 3-m extension board. The heat flux feedback that is from the combustion gas out of the FDS domain is not taken into account, making a substantially underestimated mass burning rate

7 EVALUATION OF THE FDS PREDICTION ON THE SMALL-SCALE PMMA WALL TEST

7.1 Small-scale Flame Spread Experimental Setup

Two-dimensional upward flame spread and subsequently steady turbulent burning of a thermally thick vertical fuel surface is examined experimentally³⁶. Upward fire spread measurements were made using 4.5 cm thick, 41 cm wide, 157 cm high vertical slabs of PMMA cut from a single original slab. Since the upward spread process accelerates and is therefore intrinsically unstable, great care was taken to insure truly two-dimensional spread all the way up to the top of the slab. Sidewalls (15 cm deep) were used to prevent lateral air entrainment. It was necessary to water-cool the side-walls to prevent excessive radiant heat transfer to the slab. A uniform line ignition was achieved at the bottom edge by using a narrow acetone ignitor tray. The averaged pyrolysis height (is., the advancing fuel vaporization front) was measured by visual observations of surface bubbling by peering through the rear of the slab. These results were reproduced in Figure 29.

7.2 SOFIE and FDS Calculations

Lewis, Rubini and Moss⁸ performed a field modeling of flame spread. Using the SOFIE code⁹, a simplified model of non-charring solid pyrolysis has been coupled with detailed descriptions of turbulent combustion, soot production and radiative

exchange to create a field model for fire spread prediction. The predictions is demonstrated by comparison with established two-dimensional experiments on PMMA slabs reported in the literature by Orloff et al ³⁶. The SOFIE Code uses a two-equation ***k-E*** turbulence model for modeling of buoyant turbulent flow, while the FDS uses the LES as its turbulence model. It was reported that the level of agreement between measurements of flame spread velocity, mass loss rate and incident heat flux is generally good.

In order to perform a cross-comparison for the predictions by FDS and SOFIE and the experimental measurements, a FDS domain is designed and the simulation method is similar to the large-scale, 5-m-high flame spread case. The only exception is that the thermal properties that is used in this small-scale domain is chosen to be as close as possible with those used by SOFIE calculations ⁸.

A baseline computation has been defined for model comparison purposes on a 117 x 32 mesh (H x W) on the PMMA surface. Atop of the PMMA wall is a 1-m-high gypsum board extension, served as the flame holder. The FDS domain consists of 32 x 12 x 256 by its width, depth and height, and there were over 75,000 cells in the calculation domain. The resolution of the domain is as small as 1.3 cm, and falls into the range of 5% of z^* , the characteristic length of the firepower.

7.3 The PMMA Thermal Properties

In FDS, fixed values are used for thermal properties to be used as inputs for the calculation. However, it seems that SOFIE uses the variable thermal properties for the

PMMA thermal properties³⁸. Then, averaged values for k and α are picked for the use of FDS calculations. The thermal properties are shown in Table 4, and the comparison of values of thermal conductivity and thermal diffusivity are shown in Figure 25 and Figure 26 respectively.

Thermal properties	SOFIE ³⁸	FDS
Specific heat (C_p)	$2.374 T + 1100$ J/Kg/K	-
Density (ρ)	1190 Kg/m ³	1190 Kg/m ³
Conductivity (k)	$2.49e-4 T + 0.118$ W/m/K	0.23366 W/m-K
Thermal diffusivity (α)	-	8.9141E-8 m ² /s
Heat of vaporization (ΔH_v)	1.108 MJ/kg	1,108MJ/kg
Ignition temperature (T_p)	636 K	636 K

Table 4 – Thermal Properties Used In SOFIE And FDS

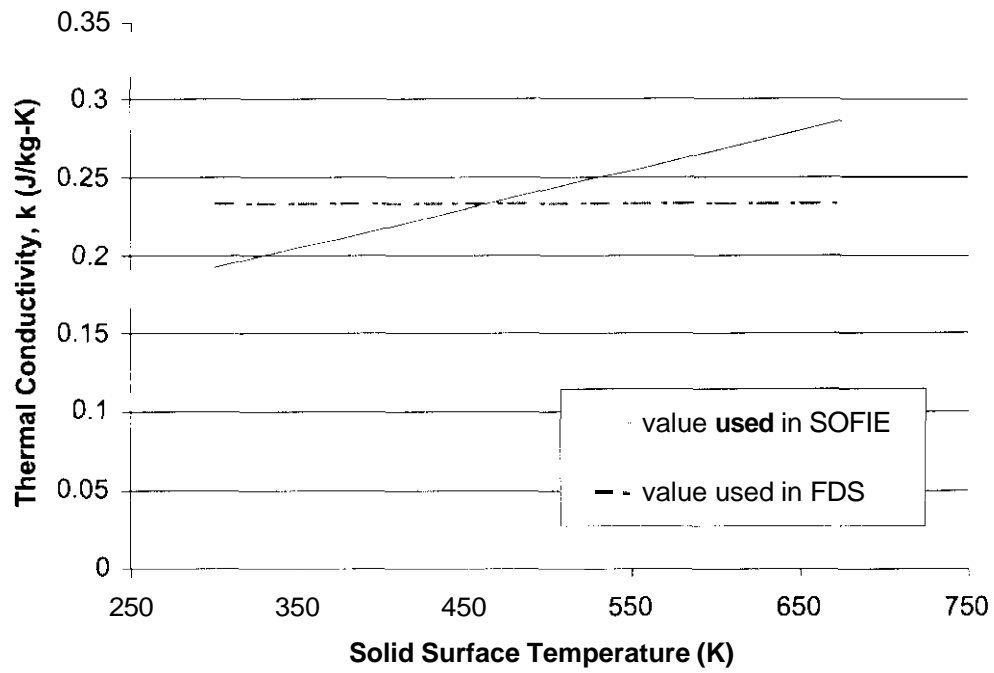


Figure 25 – Comparison Of k

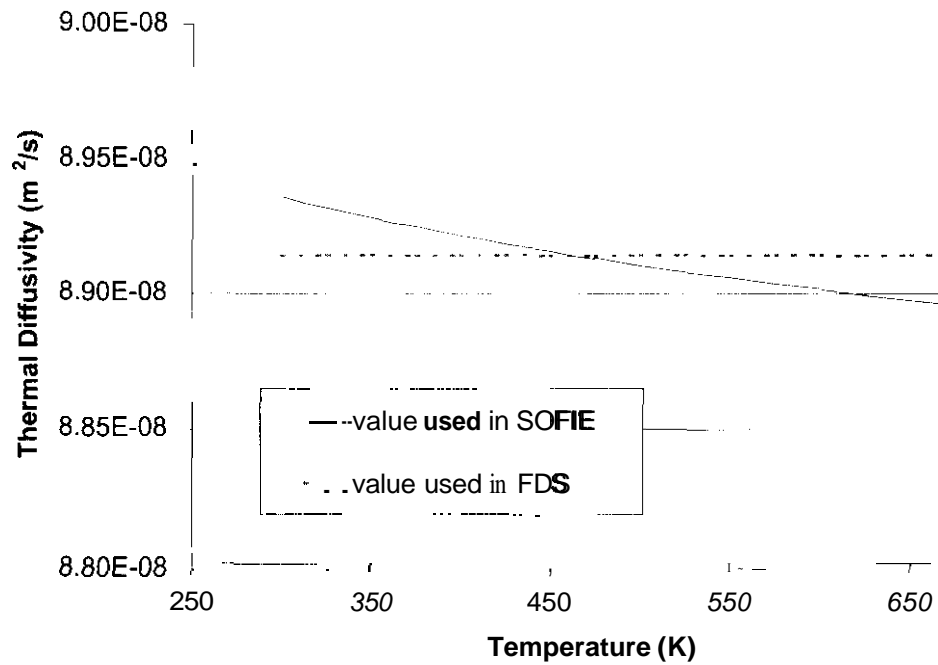


Figure 26 – Comparison Of α

7.4 Comparison of the Results

The FDS code (V 2.0) does not finish the calculations, as it ends automatically, but accidentally, when the HRR increases in a very rapid rate. In all the cases, the calculations ended with unknown reasons, regardless of the thermal properties and domain resolutions. In the FDS calculations, various thermal properties are used one by one for numerous trials: reduced k (0.209 W/m-K); increased α ($1.2\text{E-}7 \text{ m}^2/\text{s}$); increased ΔH_v (1.6 MJ/kg), etc. In addition, the resolution has been modified and coarse resolution (cell number reduced 50%) has been tried. In all these calculations, the similar “blow up” phenomena are occurred and FDS ends the calculations accidentally.

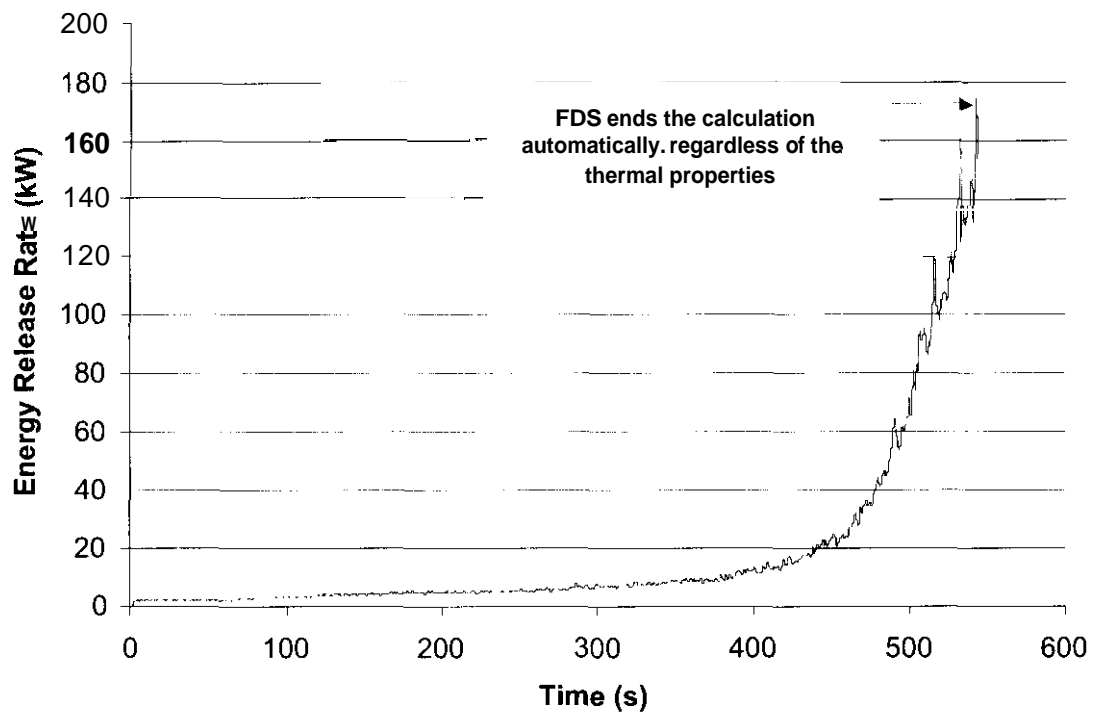


Figure 27 – Heat Release Rate Given By FDS Calculation For The Small-Scale Test

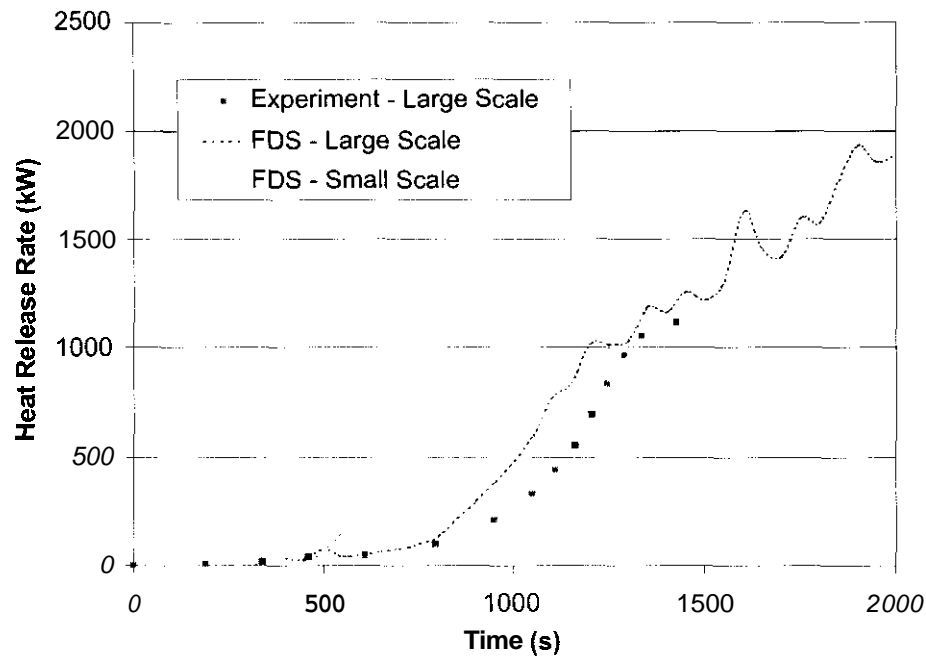


Figure 28 – Cross Comparison For Heat Release Rate Given By FDS Calculation For The Large- And Small-Scale Tests

In Figure 28, the FDS-calculated results for large and small-scale flame spread tests are compared with the 5-m experiment. There are differences for the geometry settings between the large and small-scale tests. One of those is that between the perpendicular side-plates, the large-scale test installed two 60-cm-wide gypsum boards beside the PMMA wall, while the small-scale test didn't. This may cause that a higher heat flux on the fuel surface for the small-scale test and therefore faster flame-spread.

The FDS domain for the large-scale test, due to the constrain of long computing time, uses a coarse resolution (3.7 cm), and causes inconsistencies in simulating the ignition device which is located at the base of the PMMA wall. To address this problem, the FDS-calculated results are synchronized to match the same heat release rate of the actual ignition device. When calculated ignition output was 34 kW, this was

“synchronized with the experiment time of 350 s. However, the FDS-domain for the small-scale test uses a much better resolution (1.3 cm), so that the ignition device can be simulated rather accurately. In Figure 28, the FDS result for large-scale test is the synchronized one, while the FDS result for the small-scale test is its original result.

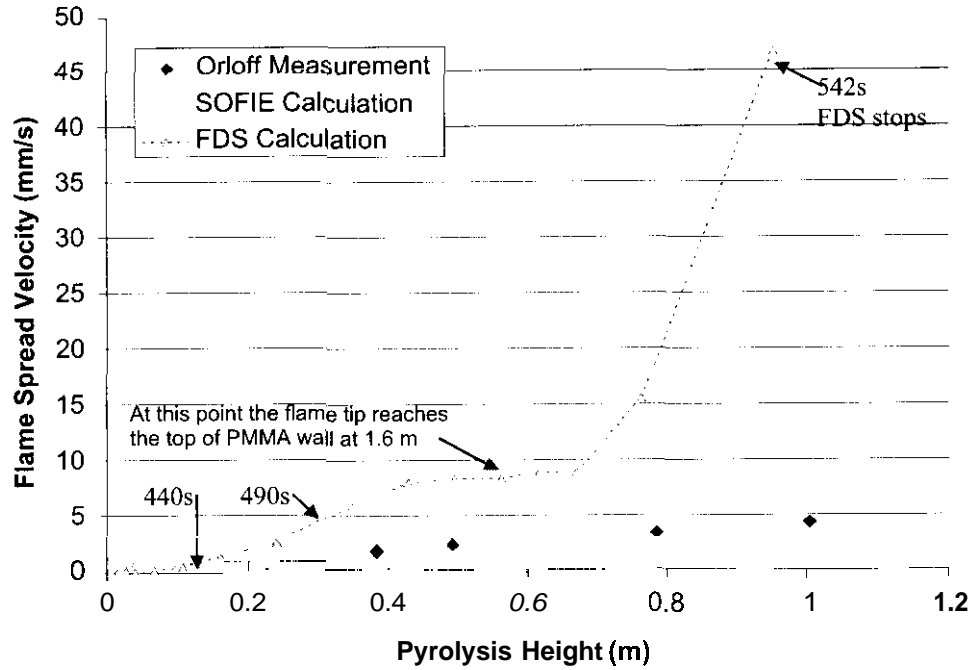


Figure 29 – Cross Comparison Between Predicted Flame Spread Velocity By SOFIE And FDS And Experimental Measurements By Orloff

Figure 29 shows the FDS-predicted flame spread velocity is higher than the experimental results. The flame spread velocity, v , is related to the surface temperature ($v \propto 1/(T_{ig} - T_s)^2$). When $T_s \rightarrow T_{ig}$, $v \rightarrow \infty$. Accelerated flame spread between 490s and 542s is shown in Figure 29. The relationship of T_s and T_{ig} is also shown in Figure 30.

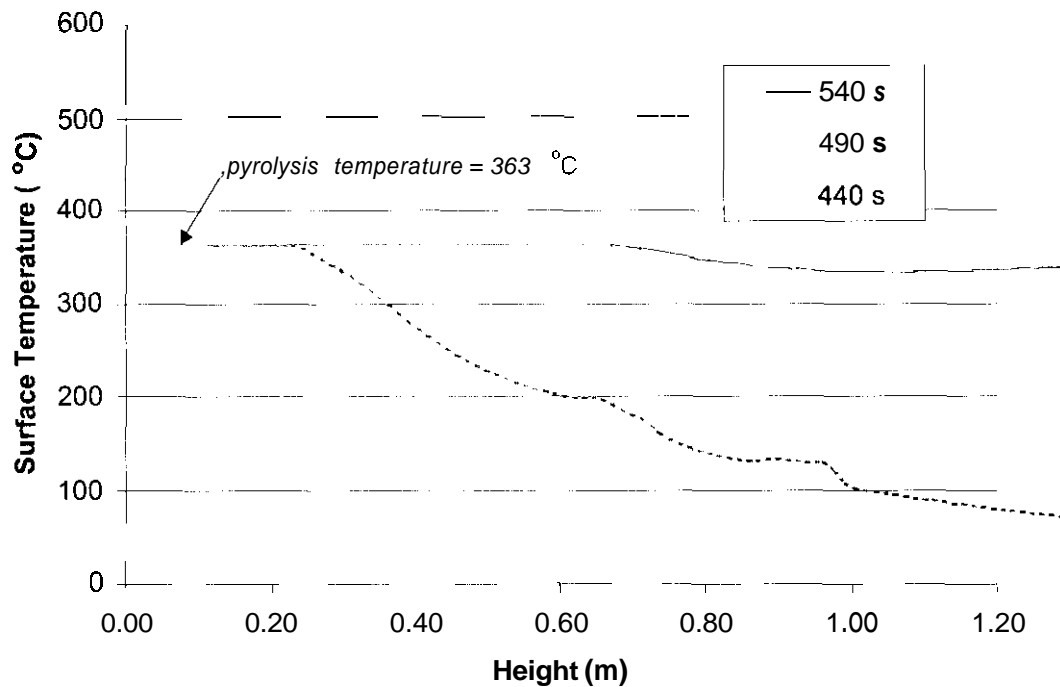


Figure 30 – FDS-Calculated Surface Temperature Vs. Height, Varied By Time

Compared to Figure 22, the surface temperature calculated by FDS appears to be much faster increase. This may be the result of higher heat flux as shown in Figure 31 and Figure 32.

In Figure 31 and Figure 32, the steady stage for Orloff's experimental results and SOFIE-calculated results are time-averaged values at an “after spread” stage, when the entire **PMMA** wall is burned and is maintained quasi-steadily. These results are compared to the FDS-calculated results that are taken for developing times, and the FDS simulation never reaches a steady stage because it stops unexpectedly.

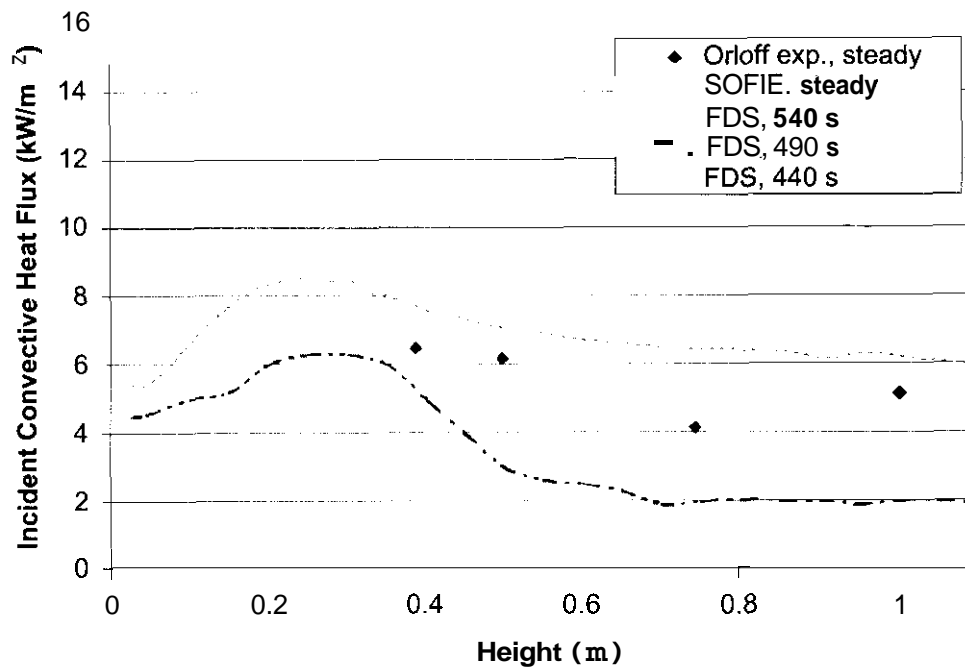


Figure 31 – Incident Convective Heat Flux Comparison

Figure 31 shows the results for convective heat flux, which is not dominant comparing to radiative heat flux. The Orloff's experimental results give that the convective heat flux, in general, consists of less than 20% of the total incident heat flux. The FDS gives satisfactory prediction for the convective heat flux.

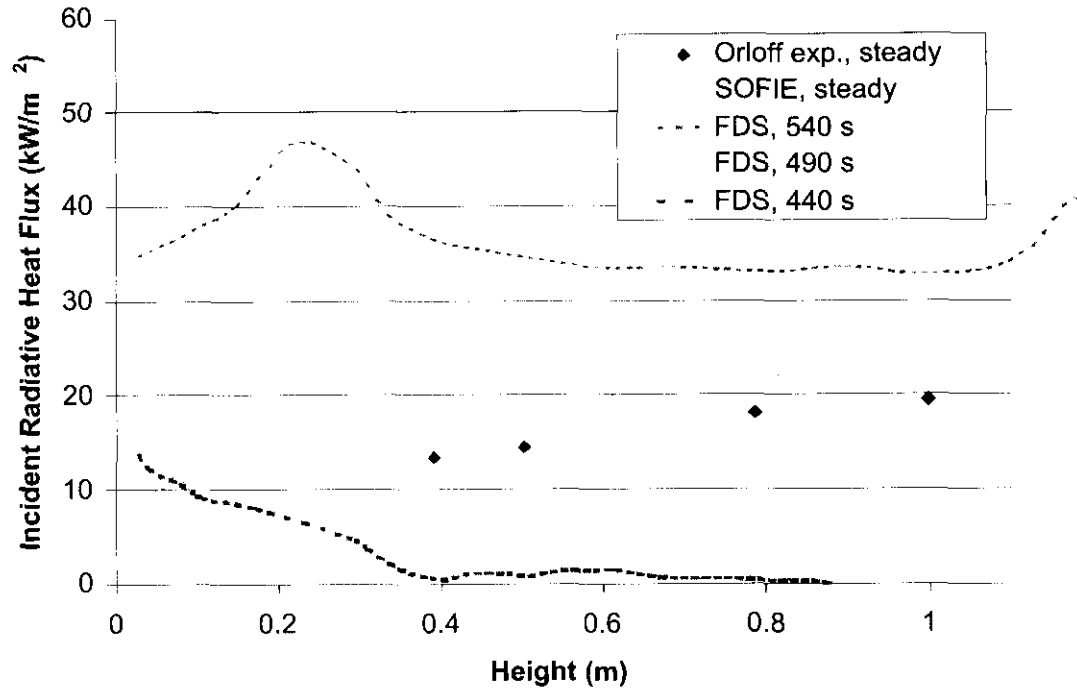


Figure 32 – Incident Radiative Heat Flux Comparison Between Predictions And The Experimental Values

Figure 32 shows the results for radiative heat flux. The trend of FDS is very different from the one given by SOFIE or the experimental result. The radiative heat flux, \dot{q}_r'' , is related to the flame temperature T_f in: $\dot{q}_r'' \propto \epsilon \sigma T_f^4$. As the flame temperature is expected to be approximately constant, and the emissivity $\epsilon \approx 1 - e^{-(\kappa \delta)} \approx \kappa \delta$ where δ is the boundary layer thickness which increases with height. Hence, the radiative heat flux should increase as the height increases. Figure 32 shows SOFIE gives the proper results while FDS does not. The reason might be that FDS is giving an incorrect flame temperature, as shown in Figure 6

8 SUMMARY AND CONCLUSIONS

Flame spread and burning rate is examined in a 5-m high **PMMA** vertical slab, using a CFD code, the Fire Dynamics Simulator (FDS). Coupled descriptions of the controlling mechanisms of hydrodynamics model for buoyancy-driven flow, mixture-fraction model for combustion, convection model, banded gray-gases transportation model for radiation, one-dimensional conduction model for pyrolysis and burning rate model are included. The approaches for pyrolysis and burning rate model are evaluated in sub-model level, and the refined algorithms are presented. The new algorithms bring in the concept of thermal penetration depth. One of the major benefits of this new term is that the thermal penetration depth is independent of the resolution of FDS domain, thus reducing the dependency of FDS prediction on surface temperature and burning rate. The proposed algorithm is not incorporated into the FDS code and is a subject of future study for quantifying its computational benefit, and the validation works are based on the existing models.

The models are first tested on a non-spread case to examine the accuracy of prediction for heat flux and gas temperature distribution. Results were compared with the literature and the radiation sub-model is tested. The FDS/LES model gives good results for flame height. The results for temperature, wall heat flux, and flame height are in qualitative agreement with data. The temperature and the heat flux are within about 30% of measured results for peak values near the base of the wall, but both decay much quicker than the experimental results.

Further predictions are made on a more complex large-scale flame spread case involved a PMMA wall, which is 5 m tall and 0.6 m wide, with perpendicular steel draft containing the flame sheets. Predictions on heat flux, gas and solid temperature, flame spread, and mass burning rate **are** evaluated. The FDS model gives satisfactory flame spread predictions. The heat release rates are within 50% of the measured experimental values. The total heat flux predictions are within 30% of measured results at the lower part of the PMMA wall but it drops quickly, and the deviation increases as the height increases. This is in agreement with the indications of gas temperature and heat flux in the non-spread case. The model over-predicts the burning rate at the lower part of the PMMA wall. But the model gives an excellent result for the 2–4 m region, as the predictions are within 10% range of Ahmad and Faeth's correlations. The poor predictions for the top region (4–5 m) are probably due to the reason that the computational domain lacks the upper extended steel sheets (as shown in Figure 10) that act as a “holder” to reduce flame fluctuations, while the experimental setup did equip such extensions.

A cross-comparison is made for FDS and SOFIE for a small-scale flame spread test. It appears that SOFIE does a better job, and **FDS** gives inconsistent results for the prediction of radiative heat flux. It seems that FDS suffers from poor accuracy for near fuel base where fuel is rich. Here the gas temperature is overestimated, and the data is underestimated when the system becomes fuel lean at the far field.

Generally, reasonable agreement is achieved with experiments at levels of spatial resolution that **are** compatible with the computational demands of field model

predictions in compartment **fire** scenarios. The strength of FDS appears in that entrainment is calculated accurately since flame extent is well predicted. The deficiency of **FDS** seems to be that combustion details are distorted, giving higher gas temperature in region of the fuel-rich area and lower gas temperature for the fuel-lean area.

APPENDIX A

Proposed Algorithm of Predicting Solid Fuel's Surface Temperature

The numerical solution was developed and provided informally by Professor James G. Quintiere from the Department of Fire Protection Engineering at the University of Maryland. The solution was also given in the dissertation of Francisco Joglar-Billoch at the University of Maryland³⁹. Here is a reproduction of the solution.

Recalling the solution for the differential equation of 1-D conduction problem, the following solution was developed to estimate the surface temperature when a solid is exposing to a time-related net surface heat **flux** $\dot{q}_{net}''(\tau) = \dot{q}_c'' + \dot{q}_r'' - \dot{q}_{RR}''$:

$$T_s - T_\infty = \frac{1}{\sqrt{\pi k \rho c}} \int_0^t \frac{\dot{q}_{net}''(\tau)}{\sqrt{t-\tau}} d\tau \quad \text{Equation 81}$$

Rewrite as,

$$\Delta T = \Psi \int_0^t \frac{\dot{q}_{net}''(\tau)}{\sqrt{t-\tau}} d\tau \quad \text{Equation 82}$$

where the variable Ψ is used to represent the constant term of the equation $1/\sqrt{\pi k \rho c}$.

Equation 81 can be represented into a "time step" form:

$$T_s^{t(n+1)} - T_\infty = \Psi \int_0^{t(n)} \frac{\dot{q}_{net}''(\tau)}{\sqrt{t^{(n+1)} - \tau}} d\tau + \Psi \int_{t(n)}^{t(n+1)} \frac{\dot{q}_{net}''(\tau)}{\sqrt{t^{(n+1)} - \tau}} d\tau \quad \text{Equation 83}$$

Using the trapezoidal rule, the first integral in the right hand side of the equation can be solved. However, the second integral has a singularity since $\tau = t + 1$. This singularity can be removed by first considering Figure 33:

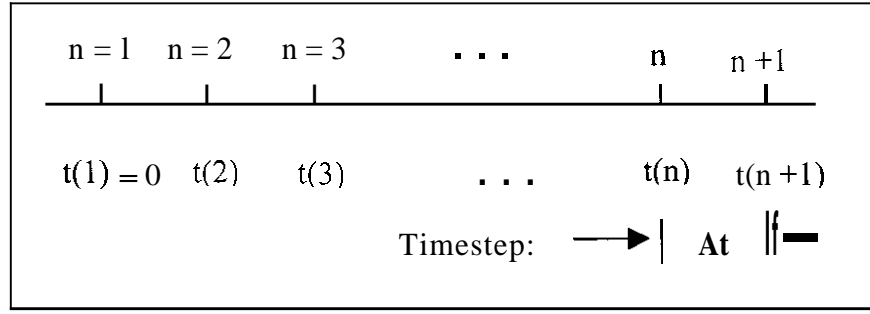


Figure 33 – Numerical Solution of Equation 83

The first integral in the right hand side of the Equation 83,

$$I_1 = \int_0^{t(n)} \frac{\dot{q}_{net}''(\tau)}{\sqrt{t^{(n+1)} - \tau}} d\tau \quad \text{Equation 84}$$

can be expressed using the trapezoidal rule as:

$$I_1 = \Delta t \left[\frac{1}{2} \frac{\dot{q}_{net}''(\tau)}{\sqrt{t^{(n+1)} - t^{(1)}}} + \frac{\dot{q}_{net}''(\tau)}{\sqrt{t^{(n+1)} - t^{(2)}}} + \dots + \frac{\dot{q}_{net}''(\tau)}{\sqrt{t^{(n+1)} - t^{(n-1)}}} + \frac{1}{2} \frac{\dot{q}_{net}''(\tau)}{\sqrt{t^{(n+1)} - t^{(n)}}} \right] \quad \text{Equation 85}$$

The second integral in Equation 83,

$$I_2 = \int_{t(n)}^{t(n+1)} \frac{\dot{q}_{net}''(\tau)}{\sqrt{t^{(n+1)} - \tau}} d\tau \quad \text{Equation 86}$$

due to the singularity mentioned earlier the following substitution is required:

$$u^2 = t^{(n+1)} - \tau$$

$$2u du = -d\tau$$

$$\text{At } \tau = t(n), u^2 = t^{(n+1)} - t(n) \text{ or } u = \sqrt{\Delta t}$$

$$\text{At } \tau = t(n+1), u^2 = 0$$

Therefore, in the transformed variable u ,

$$I_2 = \int_{\sqrt{\delta}}^0 \frac{-2u \cdot \dot{q}_{net}''(t^{n+1} - u^2)}{u} du \quad \text{or} \quad I_2 = 2 \int_0^{\sqrt{\delta}} \dot{q}_{net}''(t^{n+1} - u^2) du \quad \text{Equation 87}$$

and using again the trapezoidal rule,

$$I_2 = 2 \left(\frac{\dot{q}_{net}''(t^{(n+1)}) + \dot{q}_{net}''(t^n)}{2} \right) \sqrt{\Delta t} \quad \text{or} \quad I_2 = \sqrt{\Delta t} (\dot{q}_{net}''(t^{(n+1)}) + \dot{q}_{net}''(t^n)) \quad \text{Equation 88}$$

Finally, the solution for Equation 81 is given by:

$$T_s^{n+1} = T_\infty + \frac{1}{\sqrt{\pi \cdot k \rho c}} (I_1 + I_2) \quad \text{Equation 89}$$

9 REFERENCES

- 1 McGrattan, K.B., Baum, H.R., Rehm, R.G., *Large Eddy Simulations of Smoke Movement*, Fire Safety Journal, 20 (1998) 161-178.
- 2 McGrattan, K.B., *Smoke Trajectory Modeling*, NIST SP 935, 1999
- 3 Spearpoint, M., Mowrer, F.W., McGrattan, K., *Simulation of a Compartment Flashover Fire Using Hand Calculations. Zone Models. and a Field Model*, ICFRE3, 1998
- 4 Mowrer, F.W., Stroup, D.W., *Features Limitations and Uncertainties in Enclosure Fire Hazard Analyses – Preliminary Review*, NISTIR 6152, National Institute of Standards and Technology, 1998
- 5 Jones, W.W., *Progress Report of Fire Modeling and Validation*. NISTIR 5835, National Institute of Standards and Technology, 1996
- 6 Friday, P.A., Mowrer, F.W., *Comparison of FDS Model Predictions with FM/SNL Fire Test Data*, NIST GCR 01-810, National Institute of Standards and Technology, 2001
- 7 ASTM E 1355-97, *Standard Guide for Evaluating the Predictive Capability of Deterministic Fire Models*, Annual Book of Standards, American Society of Testing and Materials, pp. 690-695, 1997
- 8 Lewis, M.J., Rubini, P.A., Moss, J.B., *Field Modelling of Non-Charring Flame Spread*, Proceeding of the 6th International Symposium of Fire Safety Science, IAFSS, pp. 683-694, 1999
- 9 Lewis, M.J., Moss, J.B., and Rubini, P.A., *CFD Modelling of Combustion and Heat Transfer in Compartment Fire*, Proceeding of 5th International Symposium on Fire Safety Science, IAFSS, pp. 463-474, 1997
- 10 Wang, H.Y., Coutin, M., Most, J.M., *Large-eddy-simulation of Buoyancy-driven Fire Propagation Behind a Pyrolysis Zone Along a Vertical Wall*, Fire Safety Journal 37, pp. 259-285, 2002

-
- 11 Floyd, J., Wolf, L., Krawiec, J., *Evaluation of the HDR Fire Test Data and Accompanying Computational Activities With Conclusion From Present Code Capabilities*, NIST GCR 97-727, National Institute of Standards and Technology, 1997
- 12 McGrattan, K.B., Forney, G.P., Floyd, J.E., Hostikka, S., *Fire Dynamics Simulator (Version 2) – User's Guide*, NISTIR 6784, National Institute of Standards and Technology, 2001
- 13 Quintiere, J.G., *Surface Flame Spread*, Chapter 2-14 of SFPE Handbook of Fire Protection Engineering, 2nd Edition, 1995
- 14 Fernandez-Pello, A. C., *Controlling Mechanisms of Flame Spread*, *Combustion Science and Technology*, Vol. 32, pp. 1-31, 1983
- 15 Ahmad, T., Faeth, G.M., *Turbulent Wall Fires*, 17th Symposium (International) on Combustion, pp. 1149-1160, Combustion Institute, 1979
- 16 Smagorinsky, J., *General Circulation Experiments with the Primitive Equations. I. The Basic Experiment*. Monthly Weather Review, 91:99–164, 1963
- 17 Deardorff, J.W., *Numerical Investigation of Neutral and Unstable Planetary Boundary Layers*, Journal of Atmospheric Sciences, 29:91–115, 1972
- 18 Germano, M., Piomelli, U., Moin, P., and Cabot, W.H., *A Dynamic Subgrid-Scale Eddy Viscosity Model*, Physics of Fluids A, 3:1760–1765, 1991
- 19 Lilly, D.K., *A Proposed Modification of the Germano Subgrid-Scale Closure Method*, Physics of Fluids A, 4:633–635, 1992
- 20 Baum, H.R., McGrattan, K.B., and Rehm, R.G., *Three Dimensional Simulations of Fire Plume Dynamics*, Journal of the Heat Transfer Society of Japan, 35:45–52, 1997
- 21 Holman, J.P., *Heat Transfer*, McGraw-Hill, New York, 5th edition, 1989
- 22 McGrattan, K.B., Baum, H.R., Rehm, R.G., Hamins, A., Forney, G.P., Floyd, J.E., Hostikka, S., *Fire Dynamics Simulator (Version 2) – Technical Reference Guide*, NISTIR 6783, National Institute of Standards and Technology, Gaithersburg, Maryland 20899, 2001
- 23 Grosshandler, W., *RadCal: A Narrow Band Model for Radiation Calculations in a Combustion Environment*, NIST Technical Note (TN 1402), National Institute of Standards and Technology, Gaithersburg, Maryland 20899, 1993

-
- 24 Williams, F.A., *Mechanisms of Fire Spread*, 16th Symposium (International) on Combustion, pp. 1281 - 1294, The Combustion Institute, Pittsburgh, 1977
- 25 Quintiere, J., Hopkins, D., *Thermoplastic Pool Fires*, Symposium on Thermal Science and Engineering, November 1995
- 26 Quintiere, J. & Iqbal, N., *An Approximate Integral Model for the Burning Rate of a Thermoplastic-like Material*. Fire and Materials, Vol. 18, 89-98, 1994
- 27 Iqbal, N., *Burning Rate Model for Thermoplastic Materials*, MS Thesis, University of Maryland, College Park, 1993
- 28 Steckler, K.D., Kashiwagi, T., Baum, H.R., Kanemaru, K., *Analytical Model for Transient Gasification of Non-Charring Thermoplastic Materials*, Fire Safety Science Proceedings of Third International Symposium, pp. 895-904, G. Cox and B. Landford, eds., Elsevier Applied Science, London, 1991
- 29 Back, G., Beyler C., DiNenno, P., *Wall Incident Heat Flux Distributions Resulting From an Adjacent Fire*, proceeding of 4th International Association of Fire Safety Science, 1994
- 30 Quintiere, J.G., *Principles of Fire Behavior*, Delmar Publishers, Albany, New York. 1998
- 31 Ma, T., *Numerical Simulation of Unconfined Fire Plume: Accuracy And Limitations*, MS Thesis, University of Maryland, College Park, 2001
- 32 Tewarson, A, Ogden, S.D., *Fire Behavior of Polymethylmethacrylate*, Combustion and Flame 89: 237-259, 1992
- 33 Wu, P.K., Orloff, L., Tewarson, A, *Assessment of Material Flammability with the FSG Propagation Model and Laboratory Test Methods*, 13th Joint Panel Meeting of the UJNR Panel on Fire Research and Safety, Gaithersburg, MD, March 1996
- 34 Modak, A., Croce, P., *Plastic Pool Fires*, Combustion and Flames, V.30, pp. 251~265, 1977.
- 35 Steinhaus, D.T., *Evaluation of the Thermophysical Properties of Poly(methyl methacrylate)*, MS Thesis, University of Maryland, College Park, 1999

-
- 36 Orloff, L., De Ris, J., and Markstein, G.H., *Upward Turbulent Fire Spread and Burning of Fuel Surface*, 15th International Symposium on Combustion, the Combustion Institute, pp. 183-192, 1974
- 37 Quintiere, J., *Fundamentals of Fire Phenomena (Draft)*, Chapter 9, University of Maryland, College Park, 2002
- 38 Rubini, P., *private communications*, Cranfield University, UK, June 2002
- 39 Joglar-Billoch, F.J., *A Methodology for Fire Risk and Hazard Assessment, Ph.D. Dissertation*, University of Maryland, College Park, 2000